



**NAVAL
POSTGRADUATE
SCHOOL**

MONTEREY, CALIFORNIA

**DEVELOPMENT OF TECHNIQUES FOR INVESTIGATING
ENERGY CONTRIBUTIONS TO TARGET DEFORMATION
AND PENETRATION DURING REACTIVE PROJECTILE
HYPERVELOCITY IMPACT**

by

Max Peters

Thesis Advisor:

Ronald E. Brown, NPS

July 2011

Approved for public release; distribution is unlimited

THIS PAGE INTENTIONALLY LEFT BLANK

REPORT DOCUMENTATION PAGE

Form Approved
OMB No. 0704-0188

The public reporting burden for this collection of information is estimated to average 1 hour per response, including the time for reviewing instructions, searching existing data sources, gathering and maintaining the data needed, and completing and reviewing the collection of information. Send comments regarding this burden estimate or any other aspect of this collection of information, including suggestions for reducing this burden to Department of Defense, Washington Headquarters Services, Directorate for Information Operations and Reports (0704-0188), 1215 Jefferson Davis Highway, Suite 1204, Arlington, VA 22202-4302. Respondents should be aware that notwithstanding any other provision of law, no person shall be subject to any penalty for failing to comply with a collection of information if it does not display a currently valid OMB control number. PLEASE DO NOT RETURN YOUR FORM TO THE ABOVE ADDRESS.

1. REPORT DATE (DD-MM-YYYY) 01-07-2011	2. REPORT TYPE Technical Report	3. DATES COVERED (From — To) 01/2011 – 07/2011		
4. TITLE AND SUBTITLE Development of Techniques for Investigating Energy Contributions to Target Deformation and Penetration during Reactive Projectile Hypervelocity Impact		5a. CONTRACT NUMBER		
		5b. GRANT NUMBER		
		5c. PROGRAM ELEMENT NUMBER		
6. AUTHOR(S) Max Peters		5d. PROJECT NUMBER		
		5e. TASK NUMBER		
		5f. WORK UNIT NUMBER		
7. PERFORMING ORGANIZATION NAME(S) AND ADDRESS(ES) Naval Postgraduate School Monterey, CA 93943-5000				
8. PERFORMING ORGANIZATION REPORT NUMBER NPS-PH-11-006				
9. SPONSORING / MONITORING AGENCY NAME(S) AND ADDRESS(ES) Helmut Schmidt University University of the Federal Armed Forces Hamburg Holstenhofweg 85, 22043 Hamburg Germany				
10. SPONSOR/MONITOR'S ACRONYM(S)				
11. SPONSOR/MONITOR'S REPORT NUMBER(S)				
12. DISTRIBUTION / AVAILABILITY STATEMENT Approval for public release; distribution is unlimited.				
13. SUPPLEMENTARY NOTES The views expressed in this thesis are those of the author and do not reflect the official policy or position of the Department of Defense or the U.S. Government.				
14. ABSTRACT There are longstanding interests in the effects during hypervelocity penetration of projectiles and shaped charge jets through water and through water submerged targets. The effects of apparent reaction during the penetration of reactive aluminum jets through an inert fluid and water are examined in this research, where there is an attempt to differentiate the causes of observed target deformation and volume displacement. Specific developed routines in ANSYS AUTODYN finite element code are used to characterize the jet and to estimate penetration for comparison with experimental results. This report covers shaped charge, penetration and metal combustion theory which is crucial for the determined process. The jet criteria is examined using ANSYS AUTODYN, determining the jet characteristics occurring which are likely to have strong influences on the penetration process. The penetration process is simulated by a special developed technique using this software. The portions of the jet responsible for the deformation and the liquid displacement are identified, and the fraction of the energy causing the plastic deformation is estimated using 3D Explicit Dynamics WORKBENCH code. Experimental and simulation results are compared and possible reasons for observed differences are demonstrated and evaluated. The predictions are found to be in good agreement with the tests.				
15. SUBJECT TERMS shaped charge, reactive linear material, metal combustion, finite difference computation ANSYS AUTODYN				
16. SECURITY CLASSIFICATION OF: a. REPORT U b. ABSTRACT U c. THIS PAGE U		17. LIMITATION OF ABSTRACT UU	18. NUMBER OF PAGES 159	19a. NAME OF RESPONSIBLE PERSON Ronald Brown 19b. TELEPHONE NUMBER (include area code) 831-656-2635

**NAVAL POSTGRADUATE SCHOOL
Monterey, California 93943-5000**

Daniel T. Oliver
President

Leonard A. Ferrari
Executive Vice President and
Provost

This report was submitted in partial fulfillment of the requirements for the degree of Master of Science from the Helmut-Schmidt-Universität, Universität der Bundeswehr Hamburg.

Further distribution of all or part of this report is authorized.

This report was prepared by:

Max Peters

Approved by:

Ronald E. Brown
Professor and Lead Advisor
Physics Department

Reviewed by:

Andres Larraza, Chairman
Physics Department

Released by:

Karl A. van Bibber
Vice President and
Dean of Research

THIS PAGE INTENTIONALLY LEFT BLANK

ABSTRACT

There are longstanding interests in the effects during hypervelocity penetration of projectiles and shaped charge jets through water and through submerged targets. The effects of apparent reaction during the penetration of reactive aluminum jets through an inert fluid and water are examined in this research, where there is an attempt to differentiate the causes of observed target deformation and volume displacement, using specially developed routines in the ANSYS AUTODYN and WORKBENCH EXPLICIT DYNAMICS finite difference code.

This report covers shaped charge, penetration and metal combustion theory which is crucial for the determined process. The jet criteria is examined using ANSYS AUTO-DYN, determining the jet characteristics occurring which are likely to have strong influences on the penetration process. Furthermore, the penetration process is simulated by a special developed technique using this software. Experimental and simulation results are compared and possible reasons for observed differences are demonstrated and evaluated. Finally, an explanation for the effects observed in the experiments, which is supported by all available information, is provided.

KURZZUSAMMENFASSUNG

Entwicklung von Techniken zur Untersuchung von Energiebeiträgen zur Zieldeformation and Penetration bei Hochgeschwindigkeitseinschlägen von Reaktiven Projektilen

Seit langem besteht Interesse an Verbrennungseffekten von Hochgeschwindigkeitssprojektilen und Hohlladungsstacheln bei Penetration von Wasser und von Wasser umgebener Ziele. Die Besonderheiten bei der Penetration von inerten Fluiden und von Wasser durch reaktive Hohlladungsstachel aus Aluminium sind Gegenstand dieser Masterarbeit. Es werden die Gründe beobachteter Zielverformung mit Hilfe von speziellen Verfahren im FEM-Code ANSYS AUTODYN und WORKBENCH EXPLICIT DYNAMICS untersucht.

Diese Masterarbeit befasst sich mit den Grundlagen von Hohlladungen, Penetrationstheorie und Verbrennung von Metall, soweit für die untersuchten Prozesse relevant. Die Characteristica von Hohlladungsstacheln werden auf ihren Einfluss auf den Penetrationsprozess hin untersucht. Darüberhinaus wird der Prozess mit ANSYS AUTODYN unter Zuhilfenahme spezieller Techniken untersucht. Experimentelle und simulatorische Ergebnisse werden verglichen und die Gründe für die Unterschiede und aufgezeigt. Schließlich wird eine durch die Beobachtungen und Ergebnisse gestützte Theorie für die beobachteten Zielverformungen in den Experimenten erläutert.

TABLE OF CONTENTS

Nomenclature	19
I. INTRODUCTION	1
A. Motivation	1
B. Evidence of Hydro Reaction	1
C. Synopsis of Research Results	2
II. TECHNICAL BACKGROUND	3
A. Technical Background of the Shaped Charge	3
1. Introduction into Shaped Charges	3
a. Short History of the Shaped Charge	3
b. Terms and Definitions of Shaped Charges	4
2. Jet Forming Process	5
a. Estimating the Jet and Slug Velocities using the PER Theory	6
b. Estimating the Particle Velocities with Gurney Equations	8
c. Estimating the Particle Velocity with a Chanteret Equation	10
d. An Example Calculation for the Chanteret/PER Solution	11
e. Influences on the jet and the jetting process	13
3. Characteristics of the Jet	14
a. Gradient of Velocities	14
b. Temperature	15
c. Particulation	16
d. Mass Distribution along the Jet	16
4. Applicational Characteristics	16
a. Stand-Off Distance	17
b. Maximum Jet Velocity	18
B. Characteristics of the Penetration Process	19
1. Penetration Process	19
2. Erosion of the Jet in Inert Materials	21
a. Projectile Heating and Thermal Softening	21
b. Hardening Effects	22

C.	Combustion of Metal and Potential Energy Release	23
1.	Reaction of Aluminum and Water	23
2.	Potential Energy Release Approximation	24
3.	Erosion in Reactive Materials	24
D.	Description of Preliminary Experiments at the UIUC	25
E.	Overview of Experimental Evidence for the Reaction	26
1.	Qualitative Evidence	27
2.	Spectroscopy	28
3.	Calorimetry	28
4.	Controlled Penetration Experiments	29
F.	Using ANSYS AUTODYN for Shaped Charge Research	29
1.	Basics of ANSYS AUTODYN Shaped Charge Calculations .	30
2.	Simulations of the Charge Used for the Reserach	31
3.	Gathering Jet Information	32
III.	RESEARCH GOAL AND OBJECTIVES	33
IV.	NATURE OF THE PROBLEM	35
A.	Properties and Problems of Target Simulations	35
B.	Difficulties in Fluid Modeling for Target Penetration Calculations .	36
C.	Characteristics of Metal Combustion	36
1.	Description of the Combustion Process	37
2.	Ignition	37
3.	A Simple Burning Law for Spherical Particles	38
D.	Characteristics of the Jet Combustion	39
1.	Jet Properties	39
2.	Mass Gradient along the Jet	39
3.	Example Penetration Simulations	40
a.	Penetration Behavior of the Jet Parts	40
b.	Temperature	40
c.	Particulation and Surface	42
E.	Mass Distribution Between the Target Plates	42
F.	Quantifying the Energy Release during the Combustion	43
1.	Compressed Air	43
a.	Internal Energy of a Compressed Air Sphere	44
2.	High Explosive	44
3.	Evaluation of the approaches	46
4.	Estimating the Energy Release with ANSYS WORKBENCH 3D Explicit Dynamics Calculations	46

V. TECHNICAL APPROACHES	49
A. Comparing Inert and Reactive Materials in Experiments	49
1. Used Active and Inert Materials	49
2. Estimating the Difference using Square Root Rho Law	49
3. Estimating the Difference using AUTODYN Impact Simulations	49
4. Discussion of other Potential Influencing Parameters	51
5. Additional Simulations using Polyethylene as Substitute	52
B. The "Divide and Conquer" Technique to Simulate the Target Penetration	53
C. Estimating the Mass Distribution	55
1. Mass Distribution in the Target Simulation	55
2. Technique to Estimate the Mass Distribution out of TOA Data	56
D. Plate Penetration Simulations in ANSYS WORKBENCH 3D Explicit Dynamics	59
1. Jet Data	59
2. Influence of the Slug	60
3. Geometric Setup of the WORKBENCH Penetration Simulations	62
E. Plate Deformation Simulations in ANSYS WORKBENCH 3D Explicit Dynamics	62
1. Energy Source in the WORKBENCH Simulation	63
2. Geometric Setup of the WORKBENCH Deformation Simulations	65
3. Estimation of the Pressure Magnitude	65
F. Dividing Penetration and Combustion Effects	67
G. Data Acquisition in the WORKBENCH Simulations	68
H. Additional Experiments	68
1. Repeating Tests	69
2. Filter Tests	69
VI. EXPERIMENTAL RESULTS	73
A. Evaluation of the TOA data from the Preliminary Experiments in Terms of chemical Erosion	73
B. Repeating Tests	75
1. Test 1	75
2. Test 2	75
3. Test 4	76
C. Filter Tests	76

1.	Test 3	76
2.	Test 5	76
3.	Comparison of the Penetration Performance in the Filter Test with the Plate Array Tests	77
VII.	SIMULATIONS AND EXAMINATION OF EXPERIMENTAL RESULTS	
	79	
A.	Comparison of the Simulations and the Experimental Results	79
1.	Jet tip velocity	79
2.	TOA	80
3.	Penetration Depth	81
4.	Hole Diameter	82
B.	Mass Distribution and Potential Chemical Energy in the Target	83
1.	Mass Distribution Estimation from AUTODYN Penetration Simulations	84
2.	Mass Distribution Estimation from TOA and Cumulative Mass Data	85
C.	Target Plate Deformation due to Penetration	87
D.	Target Plate Deformation due to Pressure Load	89
E.	Analysis of the Available Mass and Deformation Ratio	91
VIII.	CONCLUSIONS	93
IX.	RECOMMENDATIONS	97
A.	DIMENSIONS OF THE TARGET	99
B.	DRAWINGS AND DIMENSIONS OF THE CHARGE	101
C.	OVERVIEW OF THE EXPERIMENTS	105
D.	COMPARISON OF THE DEFORMATION IN THE WATER AND OIL TESTS	107
E.	RESULTS OF THE ADDITIONAL EXPERIMENTS	111
F.	COMPLETE TOA AND HOLE DIAMETER DATA	113

G. MATERIAL PROPERTIES FOR THE AUTODYN SIMULATIONS	115
H. RESULTS OF THE MASS DISTRIBUTION ESTIMATIONS	117
I. RESULTS OF THE ANSYS WORKBENCH PENETRATION SIMULATIONS	121
J. DESCRIPTION OF CREATING GEOMETRY FOR AUTODYN WITH MATLAB	125
LIST OF REFERENCES	130

THIS PAGE INTENTIONALLY LEFT BLANK

LIST OF FIGURES

Figure 1.	Main dimensions and build up of a shaped charge	4
Figure 2.	Progress of the collapse and the jet formation of a shaped charge [Zuk98]	5
Figure 3.	Geometric parameters of a collapsing liner used for the velocity estimations in the PER theory	6
Figure 4.	Detail of figure 3 showing the relevant velocities	7
Figure 5.	Example of a Gurney configuration: a cylindric metal tube filled with explosive [Zuk98].	9
Figure 6.	Used dimensions of the liner for the Chanteret velocity estimation.	10
Figure 7.	Velocities of the Chanteret-jet and the AUTODYN simulation for the 50mm charge with NM over the x dimension of the jet	12
Figure 8.	The aluminum jet from the 50mm UIUC charge after the forming process from AUTODYN predictions. The slug, tail and tip are marked. The tail will stretch continuously after this time.	14
Figure 9.	Graph of velocity vs. x of the 50mm aluminum jet with a liner angle of 21 as used in the experiments at the UIUC, gathered from a AUTODYN simulation	15
Figure 10.	Velocity over the cumulative mass of the 50mm jet as used in the experiments at the UIUC, gathered from a AUTODYN simulation	17
Figure 11.	Principle of penetration depth over charge diameter versus stand-off over charge diameter with optimal stand-off.[Zuk98]	18
Figure 12.	Principle of the penetration process [Zuk98]	20
Figure 13.	Example of a Stress-Strain diagram for steel	22
Figure 14.	Picture of the plate array that was used in the experiments. The charge is set on the thick plate on the top. In the best tests the jet penetrated till the marked plate 9.	25
Figure 15.	Comparison of the plate deformation in the water test (left) and the oil test (right). The red line indicates the same plate in both tests. Note the strong deformation in the water test.	27
Figure 16.	Light emission over time and penetration depth of a aluminum jet into stacked steel plates submerged by water from [Fan08].	29
Figure 17.	Setup of the UIUC charge used for the simulation.	31
Figure 18.	Possible chemical energy release of the simulated jet parts over the x-dimension. The parts are marked with the blue stars.	40
Figure 19.	Comparison of the slow and the fast parts during the penetration	41

Figure 20.	Absolute temperatures of the slow ($1527\frac{m}{s}$) and the fast ($5724\frac{m}{s}$) parts of the jet during the penetration	41
Figure 21.	Internal Energy of a compressed air sphere over radius and pressure.	45
Figure 22.	Average 50mm copper rod velocity during penetration of a semi-infinite target containing water and oil vs. time	51
Figure 23.	Average 50mm copper rod velocity during penetration of a semi-infinite target containing water and polyethylene vs. time	53
Figure 24.	Principle of the "Divide and Conquer" technique to simulate the penetration process	54
Figure 25.	Average TOA of the experiments with water as submerging fluid (red points) and the matching quadratic fit (blue line).	57
Figure 26.	Picture of the penetration process of the steel plate target in a simulation. The tunnel formed by the water flowing away from the penetration axis is clearly visible.	61
Figure 27.	Plate for the WORKBENCH simulation. The green regions are the symmetry planes	62
Figure 28.	Stress-Strain Diagram. The shaded area A is a measure of the plastic work.	64
Figure 29.	Plate for the WORKBENCH simulation. The red area shows the pressure load.	65
Figure 30.	Sketch showing the values for the pressure magnitude estimation	66
Figure 31.	Plate 7 Difference in deformation of Test 12 (water,red) and Test 13 (oil,blue)	67
Figure 32.	Plate 10 Difference in deformation of Test 12 (water,red) and Test 13 (oil,blue)	68
Figure 33.	Principle of the filter tests, where one monolytic steel plate substitutes the first water/plate combinations.	70
Figure 34.	Average TOA from the all water tests and TOA from the oil test for the different plates	73
Figure 35.	TOA for the oil and the water AUTODYN simulation over the plates	74
Figure 36.	Comparison of the theoretical jet length calculated from the penetration performance for the filter test (blue) and the other experiments (red).	78
Figure 37.	Comparison of the TOA from the experiments with water as submerging fluid and the matching simulation	80
Figure 38.	Comparison of the hole diameters in the plates from the water experiments and the matching simulation	82

Figure 39.	Comparison of the average hole diameters in the plates from the water experiments and the matching simulation	83
Figure 40.	Minimum mass distribution in the water simulation. The mass distributed before the first plate is not included.	84
Figure 41.	Mass distribution between the target plates of Test 13	86
Figure 42.	Mass distribution between the target plates of Test 4	87
Figure 43.	Plate 1 Penetration Simulation	88
Figure 44.	Plate 9 Penetration Simulation	88
Figure 45.	Comparison of Plate one deformation due to jet and slug penetration in the simulation.	88
Figure 46.	Comparison of the diagonal plate deformation due to pressure load in the simulation (blue) and the water experiments (red). The red arrow points at the differing bend.	89
Figure 47.	Example plate deformation in the ANSYS WORKBENCH pressure load simulation	90
Figure 48.	Plate8 to Plate 10 diagonal deformation from the WORKBENCH simulation in blue and Test 12 in red	91
Figure 49.	Sketch of the complete target setup showing the charge, the plate stack and the containing tank as well as the dimensions.	100
Figure 50.	Engineering Drawing of the used UIUC charge liner [Mas10]	102
Figure 51.	Engineering Drawing of the used UIUC charge confinement [Mas10] .	103
Figure 52.	Plate 1 Deformation in Test 12 and Test 13	107
Figure 53.	Plate 2 Deformation in Test 12 and Test 13	107
Figure 54.	Plate 3 Deformation in Test 12 and Test 13	107
Figure 55.	Plate 4 Deformation in Test 12 and Test 13	108
Figure 56.	Plate 5 Deformation in Test 12 and Test 13	108
Figure 57.	Plate 6 Deformation in Test 12 and Test 13	108
Figure 58.	Plate 7 Deformation in Test 12 and Test 13	108
Figure 59.	Plate 8 Deformation in Test 12 and Test 13	109
Figure 60.	Plate 9 Deformation in Test 12 and Test 13	109
Figure 61.	Plate 10 Deformation in Test 12 and Test 13	109
Figure 62.	Plate 11 Deformation in Test 12 and Test 13	109
Figure 63.	Plate 1 Penetration Simulation	121
Figure 64.	Plate 2 Penetration Simulation	122
Figure 65.	Plate 3 Penetration Simulation	122
Figure 66.	Plate 4 Penetration Simulation	122

Figure 67.	Plate 5 Penetration Simulation	122
Figure 68.	Plate 6 Penetration Simulation	123
Figure 69.	Plate 7 Penetration Simulation	123
Figure 70.	Plate 8 Penetration Simulation	123
Figure 71.	Plate 9 Penetration Simulation	123
Figure 72.	Build-up of a .zon file (left) and the matching simple example consisting of one cell (right)	125
Figure 73.	Grid of the sphere and the explosive after importing into AUTODYN	126
Figure 74.	Set-Up and values of the MATLAB function to create the hollow sphere	127

LIST OF TABLES

Table 1.	Comparison the Chanteret-Jet with experimental and simulation data	12
Table 2.	Values for the Chanteret calculation	13
Table 3.	Residual Analysis for the reactive jet fired into submerged steel targets [Fan08].	28
Table 4.	Comparison of penetration simulations of a 50mm copper rod with 10mm diameter fired into semi-infinite fluid target containing water and oil, respectively.	50
Table 5.	Overview of the Tests	106
Table 6.	Test results for Test 1	111
Table 7.	Test results for Test 2	111
Table 8.	Test results for Test 4	112
Table 9.	Test results for Test 5	112
Table 10.	Complete TOA Data	113
Table 11.	Complete Hole Diameter Data	113
Table 12.	Material Properties for Nitromethane	115
Table 13.	Material Properties for the AUTODYN penetration simulations	116
Table 14.	Mass distribution data from the water simulation	117
Table 15.	Mass distribution data from the oil simulation	118
Table 16.	Mass distribution in Test 11	118
Table 17.	Mass distribution in Test 12	118
Table 18.	Mass distribution in Test 13	119
Table 19.	Mass distribution in Test 1	119
Table 20.	Mass distribution in Test 2	119
Table 21.	Mass distribution in Test 4	120
Table 22.	Values for the penetration simulations	121

THIS PAGE INTENTIONALLY LEFT BLANK

NOMENCLATURE

α	Liner Angle
β	Bend angle
δ	Taylor angle
ϵ	Strain
κ	Isentropic Exponent
σ	Stress
$\sqrt{2E}$	Gurney velocity
C	Mass per unit ratio of an explosive
D	Diameter of a burning particle
E_i	Internal Energy
EOS	Equation of state
l	Jet length
LD	Charge diameter
M	Mass per unit ratio of metal
M_b	Bending Moment
n	Amount of Substance
P	Penetration depth
q	Line Load
R	Gas constant: $8.314 \frac{J}{molK}$
R_e	Outer radius of the explosive
R_i	Inner radius of the explosive
R_{eC}	Outer radius of the confinement
R_{iL}	Inner radius of the liner

TOA Time of Arrival

U Detonation velocity of an explosive

u Penetration Velocity

v_0 Initial velocity

V_n Volume n

v_{jet} Velocity of the jet

WD Warhead diameter

DECLARATION

I hereby declare that I, Max Peters, have created this thesis by myself, without assistance of others, using only named sources and supplementary materials.

EHRENWÖRTLICHE ERKLÄRUNG

Hiermit versichere ich, Max Peters, dass ich die vorliegende Studienarbeit selbstständig verfasst habe und keine anderen als die im Quellen- und Literaturverzeichnis genannten Quellen und Hilfsmittel genutzt habe, insbesondere keine dort nicht genau bezeichneten Internetquellen. Alle aus den Quellen und der Literatur wörtlich oder sinngemäß bernommene Stellen wurden als solche kenntlich gemacht. Die ebenfalls eingereichte elektronische Version der Arbeit entspricht der schriftlichen.

THIS PAGE INTENTIONALLY LEFT BLANK

ACKNOWLEDGEMENTS

First of all I want to thank Prof. Ronald E. Brown, who not only guided me over the research and provided his knowledge and experience, but also his generous hospitality.

Additionally I would like to thank Prof. Hendrik Rothe, who talked me into going to the NPS in the first place and provided support along the way through all the bureaucracy to reach this goal.

Thanks to Dr. Cornelius Hahlweg, who gave me motivation, support and the possibility of practical experience with shaped charges and explosive effects.

I would like to thank Dione "Dee" Martinsen for helping me with the daily struggle and the American way of administration.

Special thanks to the team at the UIUC, Prof. Nick Glumac and Lance Kingston for providing the experiments and evaluating the data.

Special thanks need to be given to the hard working German People, who payed for my complete education and training beginning from elementary school over officers training and the university up to this very moment and beyond. I will give my best to justify this investment.

Also to the American people, who welcomed me kindly in its beautiful country.

Finally I would like to thank my family for their endless support all my life, and my wife Suzi who is the best thing ever happened to me.

This Thesis was written using **LATEX**.

THIS PAGE INTENTIONALLY LEFT BLANK

I. INTRODUCTION

A. MOTIVATION

High velocity impacts of combustible metals such as aluminum and hafnium in oxide rich materials like halogenated polymers are known to cause blast effects, caused by the reaction of the metal.

Although the effect is very likely in aqueous media and especially water submerged targets with water being rich in oxygen, it is often ignored¹, and the differences between experimental results and hydro codes are mostly declared with uncertainties in the experimental setups or the simulations.

The goal of this research is to determine the properties and circumstances leading to the combustion and to analyze the penetration process using ANSYS AUTODYN hydrocode simulations. Additionally the magnitude of the involved energy is estimated.

B. EVIDENCE OF HYDRO REACTION

Experiments conducted at the University of Illinois² by Glumac, Fant and Mason³ and at the Naval Postgraduate School and the Ernst-Mach-Institute by Brown and Dolak⁴ showed strong evidence for combustion effects in water submerged targets, with deformations not explicable with the hydrodynamic theories which are usually used in impact theory. These results are supported by residual analysis showing large ratios of reaction products after penetrating aqueous media.

There are observed in these experiments substantial increases in light emission along the penetration path and significant target deformations.

¹See for example [Eld99]

²University of Illinois at Urbana-Champaign, referred to as UIUC.

³See [Mas10]

⁴See [Dol08]

The observed deformations is the motivation of this research due to the possibility of increasing the efficiency of shaped charge warheads in terms of increasing the demolition ability if used against under water targets.

C. SYNOPSIS OF RESEARCH RESULTS

The results of this research can be divided in two main groups.

Firstly, it was proven that the observed target deformations can not be caused by effects other than the reaction of the jet material with the target fluid.

Secondly, the amount of energy which is needed to cause those deformations was estimated.

All results rest upon detailed examination of the process using simulations and analytic methods as well as experiments.

II. TECHNICAL BACKGROUND

The following chapter provides basic background needed for this research.

Initially the shaped charge is introduced and determined. This includes the jet forming process and especially its characteristics which have a strong influence on the further process.

The penetration process is evaluated and the influencing parameters are shown. A simple but important analytic law for the description of the penetration process is introduced, and parameters of the erosion of the jet in inert materials are shown.

To provide basic information potential of reactive shaped charge jets the reaction is explained and the possible energy release of the metal combustion is estimated. Additionally the potential increase of erosion due to the chemical reaction is discussed.

Furthermore the using of ANSYS AUTODYN hydrocode for shaped charge research is introduced and explained.

Finally previous studies are displayed and evaluated.

A. TECHNICAL BACKGROUND OF THE SHAPED CHARGE

1. Introduction into Shaped Charges

In a shaped charge a -in most cases- conical cavity in the explosive is covered with a liner. If the explosive detonates, a small portion of the liner material is formed into a hypervelocity jet which is able to penetrate deep even in very strong targets.

In the following section a briefly overview of the aspects of a shaped charge is provided⁵.

a. *Short History of the Shaped Charge*

The first scientific demonstration of the shaped charge effect was realized by von Foerster, a German, in 1883. It was rediscovered by Charles E. Munroe, a US-Navy

⁵The section is mostly based on [Zuk98]. This source gives a very detailed overview for all aspects of shaped charges, and is highly recommended for everyone who is interested in this topic.

Officer in 1888⁶. He discovered that a cavity between an explosive and a surface causes more damage to the surface than the sheer explosive would.

It was discovered later that applying a liner on the surface of the cavity improves the penetration capability. In late 1930 military uses of the effect were determined, and finally the first deployment was done by German paratroopers in the fights by Fort Eben-Emael in Belgium, where lined shaped charges were used to destroy armored turrets. Later the principle was used in anti-tank weapons as Bazooka and Panzerfaust, and is used today in similar weapons.

b. Terms and Definitions of Shaped Charges

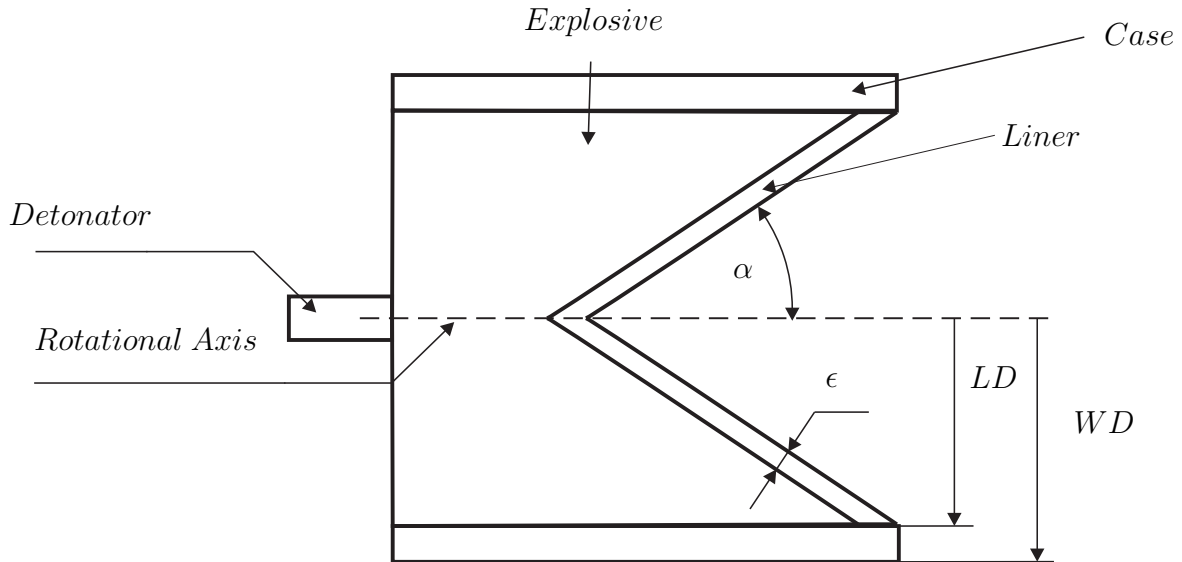


Figure 1: Main dimensions and build up of a shaped charge

Figure 1 gives an overview of the main parameters and build-up describing a shaped charge used in this work. The charge is rotationally symmetric. It can be described as a *Case*, filled with *Explosive*, which will be initiated from the left by a *Detonator*. The explosive forms a cavity, mostly conical in shape, which is layered by a *Liner*. The liner is mostly metal, but can be any stable material. Due to the principles of the process,

⁶After Munroe the effect is called 'Munroe-effect'. It describes the function without a liner.

mostly the density is important. Even glass or water could, theoretically, form a shaped charge jet.

The main dimensions are the charge diameter LD^7 , the liner angle α and the liner thickness ϵ . WD describes the warhead diameter.

2. Jet Forming Process

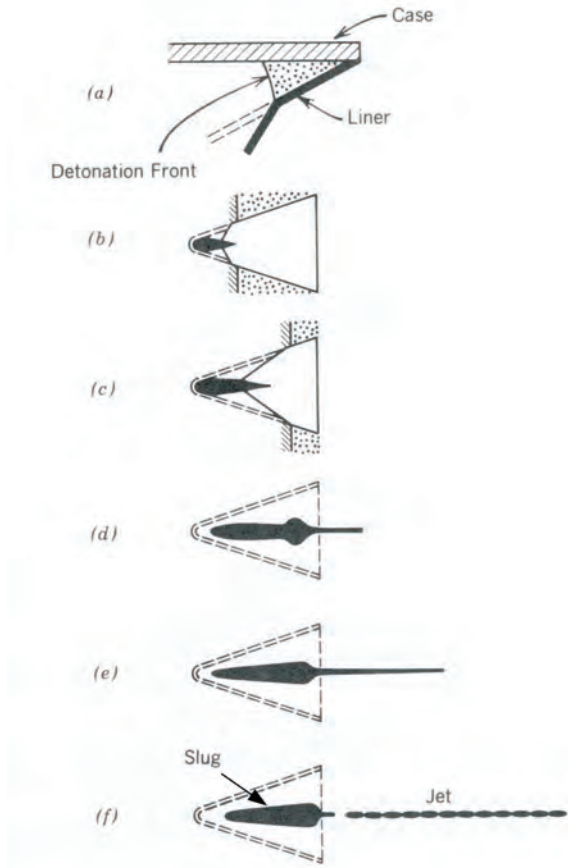


Figure 2: Progress of the collapse and the jet formation of a shaped charge [Zuk98]

When the explosive is initiated, the detonation front travels along the charge. As it hits the liner, the material is facing very high pressures (some GPa) and therefore begins to flow⁸ very fast towards the center of the cavity. Because of the extreme high pressures and

⁷Or caliber of the charge

⁸The liner “collapses”

velocities, any material behaves like a fluid. Shearstrength can be ignored. As mentioned before, the main determining factor of the behavior of the liner material is the thickness and the density.

The charge being symmetric, the material is forced to flow in the direction of the rotationally axis. This process forms a very fast traveling jet and a relatively slow traveling slug, depending on where the material flows. The jet is responsible for the penetration.

It is impossible to describe the process analytically. But it can be described with relative easy theories, which estimations lead to reasonable results.

a. Estimating the Jet and Slug Velocities using the PER Theory

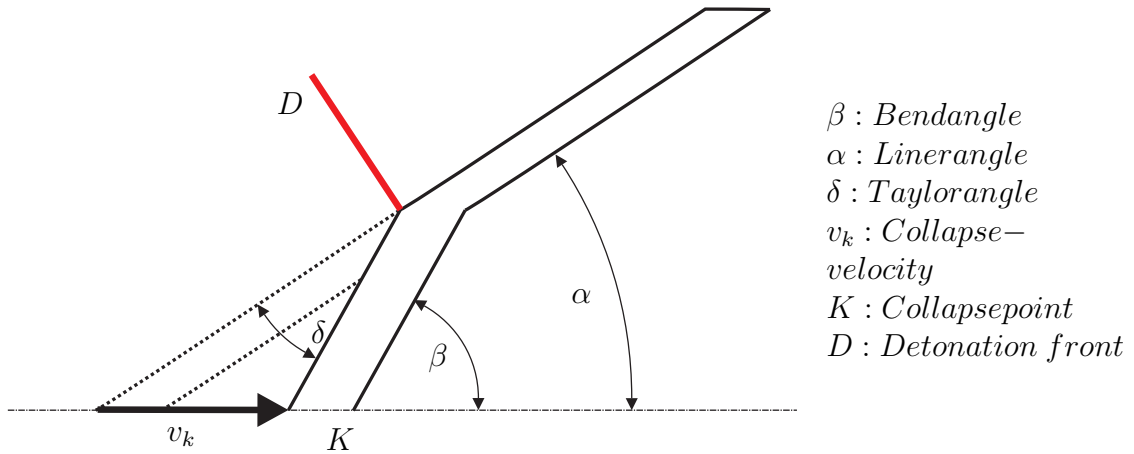


Figure 3: Geometric parameters of a collapsing liner used for the velocity estimations in the PER theory

The PER-Theory provides a principle to estimate particle velocities respecting the angle between shock wave and liner and also the different velocities which will occur along the jet. The main presumptions are that the metal is accelerated instantaneously and that material strength and compressibility can be neglected. This allows to find the final jet velocity with relatively easy geometrical and fluid dynamic considerations.

In figure 3 the main geometric parameters are given, supplemented with figure 4. The key to the model is the Taylor angle, which can be found by equation 1. Herein U is the detonation velocity of the explosive.

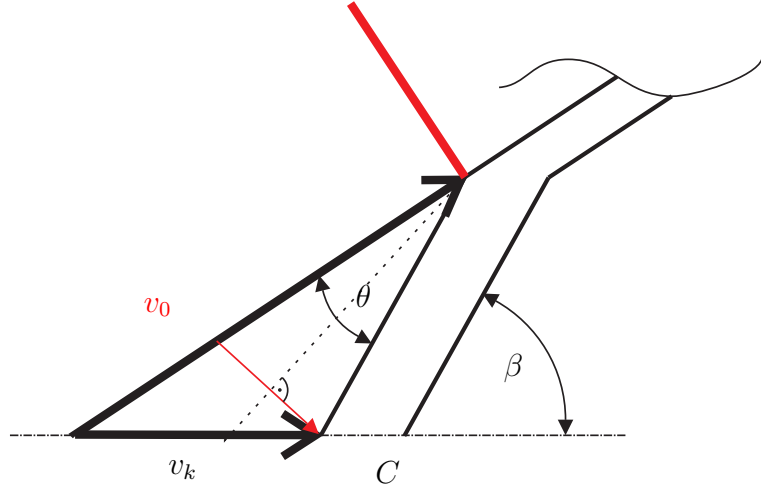


Figure 4: Detail of figure 3 showing the relevant velocities

$$\sin \frac{\delta}{2} = \frac{v_0}{2U} \quad (1)$$

The Taylor angle respects the fact that the particles are not accelerated normal to the metal surface. Using the equations which root in the geometry given above, even a cylinder, wrapped with explosive will collapse with an angle towards the rotationally axis if initiated from one side. The simple model used here can be found in [Wil03] [Sch10], and [Zuk98]. It is a summary of the Taylor- and the PER model and results in simple equations to estimate the jet velocity and the masses of the slug and the jet of a shaped charge.

These equations will need the bending angle β . This angle varies by the material combination, the detonation velocity and, of course, the geometry. It can either be gathered by experiments or can be estimated knowing the particle velocity from Gurney (See section b) and refers directly to the Taylor angle being the sum of δ and α .

$$\beta = \alpha + 2 \cdot \arcsin \frac{v_0}{2U} \quad (2)$$

With that information many important parameters can be estimated. For example it could be useful to know which parts of the liners mass go into the jet and which

into the slug. The collapse point being defined as the point of origin of the coordinate system and therefore being the inertial system, one can use the Bernoulli equation to describe the process [Wil03]. Estimating an stationary adiabatic process with an incompressible fluid one can easily find that the masses will follow equation 3 and 4, correlating only with the mass of the whole liner and β^9 .

$$m_{Jet} = \frac{1}{2}m_{Liner}(1 - \cos \beta) \quad (3)$$

$$m_{Slug} = \frac{1}{2}m_{Liner}(1 + \cos \beta) \quad (4)$$

The velocity of the jet will be provided by the equation 5.

$$v_{jet} = \frac{v_0}{\sin\left(\frac{\beta}{2}\right)} \cdot \cos\left(\alpha + \delta - \frac{\beta}{2}\right) \quad (5)$$

One important initial information needed for the PER theory is the initial velocity of the liner particles. This velocity can be estimated by the following approaches.

b. Estimating the Particle Velocities with Gurney Equations

The Gurney Equations are easy way to estimate initial velocities of material which is accelerated by an explosion and can therefore provide the missing value for the PER theory.

The equations are based on a simple assumption: the chemical energy of the explosive is converted directly in the kinetic energy of the accelerated material, explosion products and the metal. The initial velocity is reached instantaneously. The explosive-specific Gurney-Energy is added to take account of the thermodynamic losses. So basically the model is based on the conservation of momentum and energy, supplemented by a correctional term.

⁹It can be seen, that a smaller liner angle, which leads to a smaller β will decrease the mass flowing into the jet.

Figure 5 provides a simple cylindric configuration of explosive and metal and the equation 6 shows how to estimate the initial velocity of the metal particles.

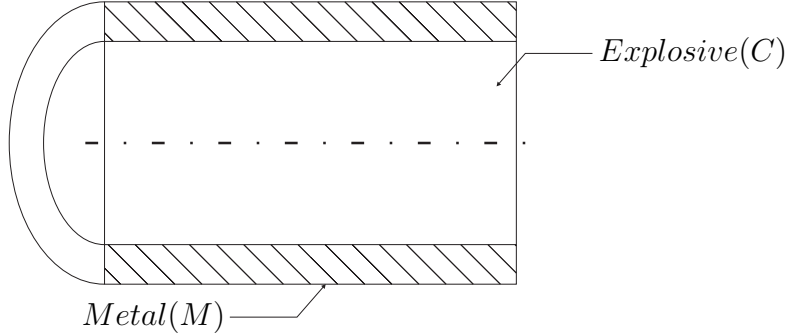


Figure 5: Example of a Gurney configuration: a cylindric metal tube filled with explosive [Zuk98].

$$v_0 = \sqrt{2E} \left[\frac{M}{C} + \frac{1}{2} \right]^{\frac{1}{2}} \quad (6)$$

In the equation M and C in $\frac{M}{C}$ are the masses of the metal and the explosive¹⁰, and v_0 is the absolute initial velocity. The expression $\sqrt{2E}$ describes the Gurney-velocity, being calculated out of the Gurney energy E , which is a mass specific experimental gained value. It includes all the losses explained above and is explosion specific. To give an example, for PETN with a density of $1.76 \frac{g}{cm^3}$ it is $2.93 \frac{km}{s}$ ¹¹.

There are some restrictions to the use of the model. The M over C ratio, for example, should be within 0.2 to 10. And of course it can not provide information about the time till the metal reaches its full velocity due to its presumptions. But the main restriction regarding shaped charges is the fact that Gurney estimates a shock wave traveling normal to the surface of the metal. In a shaped charge build-up it will travel with an angle though. Also the $\frac{M}{C}$ ratio changes within the charge. Therefore there is no Gurney equation which is able to provide an initial particle velocity for the whole liner, so the initial velocity will differ.

¹⁰Which descriptions are used for M and C is depending on the configuration. If it is e.g. a metal plate with a layer of explosives, M and C should be given in mass units per area units.

¹¹See, for example, [Hom02]

c. Estimating the Particle Velocity with a Chanteret Equation

There are some assumptions in the Gurney equations which restrict the use of the Gurney formula. The main constraint is the angle that occurs between the detonation front and the metal liner. In the Gurney model the front always hits the liner normal to its surface.

Chanteret [Fli86] developed a model to calculate the initial velocities using a control volume approach. It is basically a modified Gurney equation.

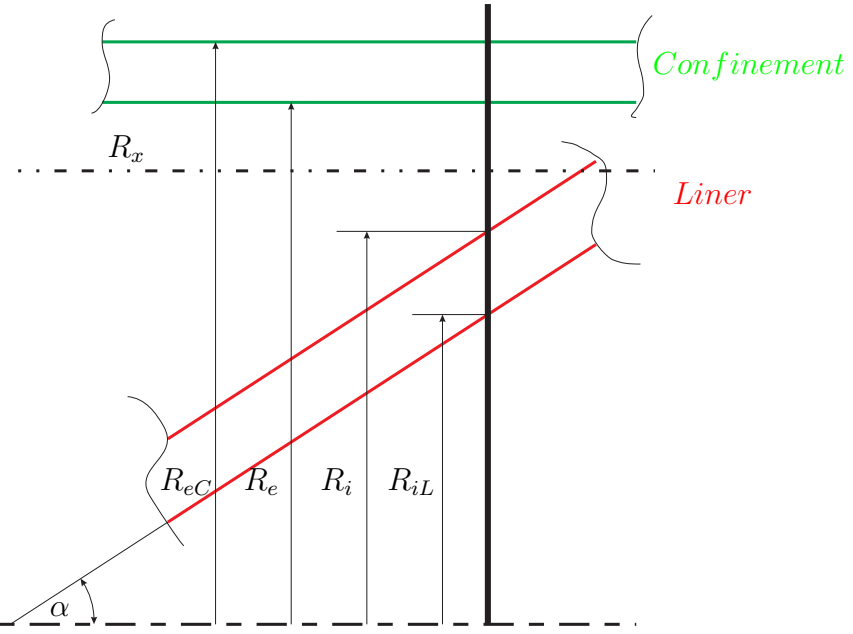


Figure 6: Used dimensions of the liner for the Chanteret velocity estimation.

The basic assumption is that the liner part is modeled as a cylinder¹². The radius of the cylinder is calculated first. This has to be done all over the liner, so the solution is discrete. Figure 6 gives the needed dimensional parameters. The black vertical line indicates the actual location of the detonation wave.

The theoretical radius R_x is the solution of equation 7:

¹²Also it is assumed that the metal reaches its final velocity instantaneously like in the Gurney model.

$$\begin{aligned}
& R_x^3 + 3R_x \left[(R_e + R_i) \cdot \frac{\rho_0}{\rho_{CJ}} \cdot \frac{M_e}{C} \cdot R_e + R_i R_e \right] \\
& - 3R_i R_e (R_e + R_i) \left[\frac{2}{3} + \frac{\rho_0}{\rho_{CJ}} \cdot \frac{M_i + M_e}{C} \right] = 0
\end{aligned} \tag{7}$$

Here are M_i , M_e and C the mass ratios per length unit of the liner, the confinement and the explosive. The densities ρ_0 and ρ_{CJ} are the original and the Chapman-Jouguet densities of the explosive

If the radius is known, v_0 can be calculated with equation 8

$$v_0 = \frac{1}{2} \cdot \frac{\sqrt{2E}}{\sqrt{\left(\frac{R_e^2 - R_i^2}{R_e^2 - R_i^2}\right) \frac{M_i}{C} + \frac{1}{6}}} \tag{8}$$

Using this velocity as an input parameter for the PER theory it provides results like explained below.

d. An Example Calculation for the Chanteret/PER Solution

With Chanteret and PER combined it is possible to approximate the jet velocities. The initial velocities must be calculated for each radius of the liner and then used to estimate the resulting jet velocity of this part.

In figure 7 the velocities of the Chanteret-Jet are compared with those of a jet simulation. Both are done for a 50mm shaped charge with a angle of 21, like used in the experiments at the UIUC which are the basis for this research¹³. The explosive is *NM*, the liner material is aluminum and the confinement is made of steel.

The difference in the tip is easy explained. The model lacks, like all Gurney estimations, of the fact that it takes time to accelerate the material, while it is assumed that it reaches the velocity instantaneously in the model. Therefore the tip is slower in reality than in the model.

¹³More detailed information on this charge can be found in IIF2 as well as in the appendices B and A.

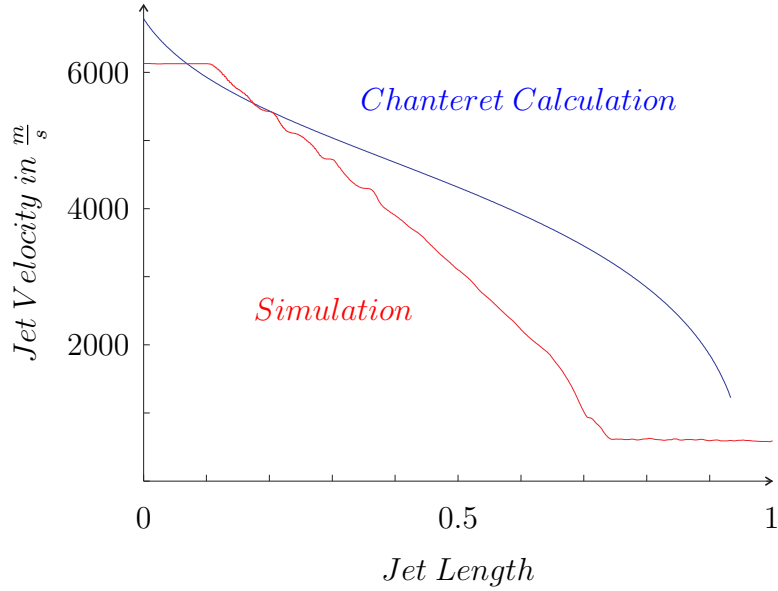


Figure 7: Velocities of the Chanteret-jet and the AUTODYN simulation for the 50mm charge with NM over the x dimension of the jet

Also the jet is slower in the later parts, because of the losses in the plastic and elastic work that is done¹⁴.

Tabular 1 compares the tip velocities from Chanteret with the experimental data from [Mas10]¹⁵ and a simulation made in AUTODYN, for the actual 50mm charge which is of interest in this research.

	Chanteret	Experiment	Simulation
$\hat{V}_{Jet} \text{ in } \frac{m}{s}$	6790	6180	6130
Difference to Chanteret		9.8%	10.7%

Table 1: Comparison the Chanteret-Jet with experimental and simulation data

The values¹⁶ used for the explosives are given in tabular 2.

All these equations can, of course, only give a rough estimation of the parameters of a shaped charge. But they are very useful to get a first overview before starting

¹⁴See also IIA4b

¹⁵See also IID

¹⁶Compare [Coo96] and [Zuk97]

	ρ_0 in $\frac{g}{cm^3}$	ρ_{CJ} in $\frac{g}{cm^3}$	U in $\frac{m}{s}$	$\sqrt{2E}$ in $\frac{m}{s}$
NM	1.128	1.607	6290	2410

Table 2: Values for the Chanteret calculation

simulations and experiments.

To estimate the processes and characteristics much more exactly finite element methods must be used. They include all the processes and properties which are neglected or cannot be included in simple analytic estimations and therefore provide much more exact results.

e. Influences on the jet and the jetting process

The forming of the jet is a very sensitive process. Small changes in the circumstances can disturb it seriously. Some influences are listed below.

- The liner angle is the one key factor for the behavior of the shape. The smaller the angle, the faster the jet. But also the jet mass decreases (See equation 3), and the jet becomes more instable.
- Because of equation 2 and 5 the detonation velocity of the explosive is also responsible for jet velocity, as is the density of liner material and explosive.
- The machining and assembling of the charge must meet special requirements. If cavities between explosive and liner exist, the Munroe effect will destroy the liner and disturb the formation. Also any antisymmetry in the liner will disturb the flow. The particles will not meet in the rotationally axis and therefore the jet will, for example, lack of velocity.

These are some examples for important parameters for shaped charges. Some others will be explained in the next sections.

3. Characteristics of the Jet

Figure 8 shows the jet which was produced by the charge discussed in this research at the stand of distance of 127mm, or $35.1\mu s$ after the initiation. The different parts are marked. The detailed characteristics are described in the following sections.

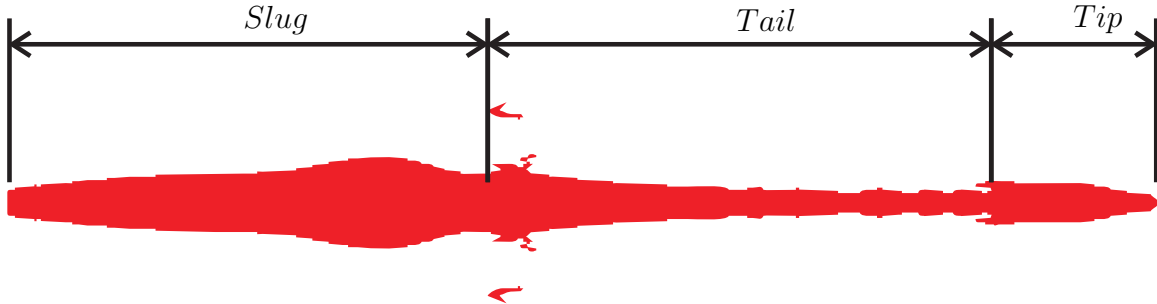


Figure 8: The aluminum jet from the 50mm UIUC charge after the forming process from AUTODYN predictions. The slug, tail and tip are marked. The tail will stretch continuously after this time.

a. *Gradient of Velocities*

The velocity of the jet is not the same in all parts. The tip contains the fastest particles; then the velocity is decreasing over the length of the jet till it reaches the minimum in the slug. In figure 9 an example for the velocity versus the x-axis of the jet is given. Here x is measured from the tip to the tail of the jet¹⁷.

While the tip velocity reaches more than $6 \frac{km}{s}$ in the example, the after end tail will only reach $1 \frac{km}{s}$, and the slug will be even slower (about $0.6 \frac{km}{s}$).

The first parts of the tip are slightly slower than the fastest parts. The reason for this effect is the fact that the first parts of the liner, which are very close to the rotational axis, cannot be accelerated to the maximal possible velocity till they are reaching the axis. Therefore the fastest parts are situated a little bit further.

¹⁷Note that this is the initial jet length directly after the formation. Due to the velocity gradient explained below this length increases during the process.

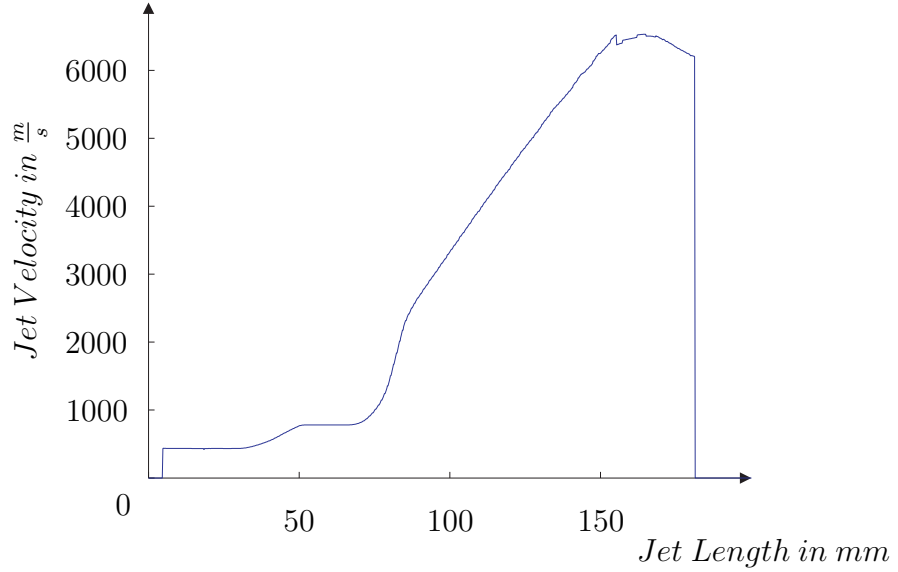


Figure 9: Graph of velocity vs. x of the 50mm aluminum jet with a liner angle of 21 as used in the experiments at the UIUC, gathered from a AUTODYN simulation

b. Temperature

The jet material is heavily reshaped in the forming process. This leads to a increased temperature of the jet. Because of the short time the heat of explosion will not influence the jet much, neither there is much conduction, and therefore the temperature is surprisingly low in the area of ca. 850 to 900K[Haz06]¹⁸.

Walters and Zukas [Zuk98] are predicting the temperature to be more than the melting temperature of the material in peak and between 0.2 to 0.5¹⁹ times in average, which gives temperatures between 400 and 600K for aluminum jets.

Von Holle and Trimble [Tri76] measured explosively driven copper plates and copper jets, formed by shaped charges using Composite B and Octol as explosives. The average jet temperature for Composite B was 700K and 840K for Octol.

On the other hand the temperature will rise much when the jet is penetrating. The heat will, due to the high velocity again, have no time to flow deep into the jet. For this

¹⁸This value was measured in experiments, using thermo graph cameras and copper jets.

¹⁹Based on the temperature in $^{\circ}C$

reason the eroded particles will carry most of the heat, which leads to high temperature of the eroded particles, both of the jet and the target material.

c. Particulation

Due to the gradient of velocity the jet sees tensile stress. This stress will increase along the movement. Therefore the jet tends to particulate. This effect depends on the velocity gradient, the distance till the jet is eroded and the jet material.

Another reason why jets can particulate is the exceeding of certain flow velocities. The effect is described in I4b.

The particulation can have an influence on the penetration performance, especially when the parts will not be in the same axis when impacting. Particulation can also lead to an unstable jet, which will decrease the performance strikingly.

d. Mass Distribution along the Jet

The ratio of mass over length is increasing from the tip to the tail of the jet. This is caused by the elongation and the increasing radius.

The elongation leads to a difference in density. The density will be lower as the natural density of the material. During the formation process there are also flow effects which decrease the density. The effect is explained more detailed in II4b.

Another and even stronger reason is the difference in radius over the length. The tip is usually very thin; then the radius increases till it reaches its maximum at the end of the jet. Therefore the slower parts of the jet are containing more mass than the faster parts next to the tip.

The tip again contains more mass due to the effect explained above.

In figure 10 the velocity over the cumulative mass for the 50mm jet is shown.

4. Applicational Characteristics

There are some parameters which must be considered when a shaped charge is deployed due to the very unique and sensitive process.

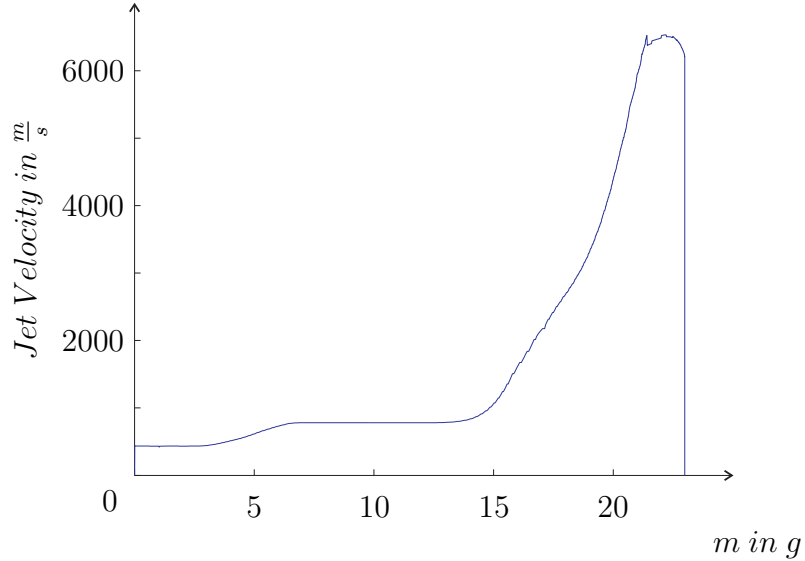


Figure 10: Velocity over the cumulative mass of the 50mm jet as used in the experiments at the UIUC, gathered from a AUTODYN simulation

a. Stand-Off Distance

To achieve the maximum penetration performance the charge must be initiated at a certain distance from the target. This distance is called the stand-off.

Like shown below in section IIAB the penetration depth is linearly dependent from the total length l of the jet. The jet is stretching because of the velocity gradient. If the stand-off distance is to small the jet will be rather short and therefore lack in performance.

On the other hand, when the stand-off distance is too big, the jet will begin to particulate, and the total length of the jet stops to increase. Also the particles are more sensitive for disturbances and can tumble out of the axis, which decreases the effective jet length and therefore the performance. This leads to the situation like shown in figure 11: until a certain point the influence of the elongation overbalances the influence of the particulation and vice versa.

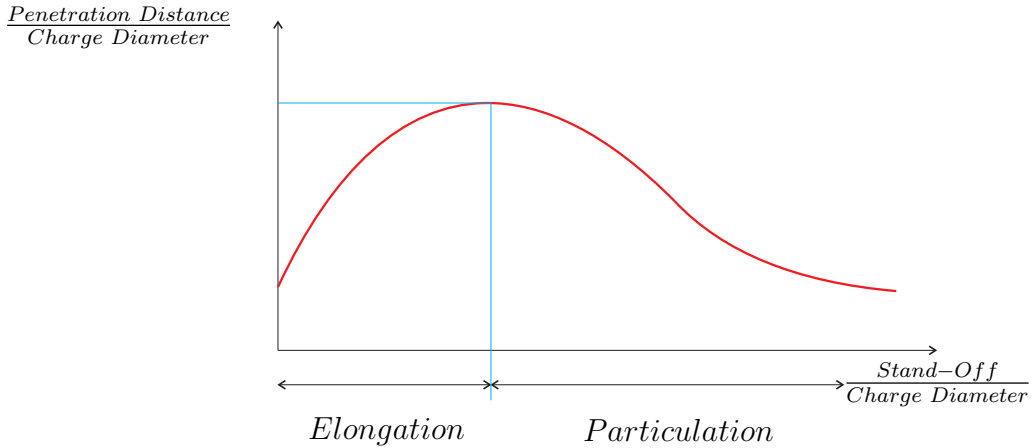


Figure 11: Principle of penetration depth over charge diameter versus stand-off over charge diameter with optimal stand-off.[Zuk98]

It has been found that the optimal stand-off distance for high performance charges lies between 6 to 10 times the charge diameter, depending also on the liner angle and the material.

b. Maximum Jet Velocity

The theoretical limit for the jet velocity is provided by the Birkhoff et al. theory²⁰. The smallest possible liner angle is 0, which means that the liner has the form of a cylinder. Under this condition of instantaneous collapse the theoretical velocity is than twice the detonation velocity of the explosive with a jet mass equal to zero.

Indeed, experiments showed very high jet velocities; but the performance is relatively poor due to the vast particulation, and the small amount of mass flowing into the jet.

However, the real limiting velocity is far below the theory. There is a maximum flow velocity which is linear to the bulk sound velocity of the liner material. Beyond this flow velocity the jet becomes incoherent. The effect is referred to as bifurcation.

²⁰This was the first theory which described the formation process mathematically. It assumes the liner to be a wedge instead of a cone, and also ignores all strengths. It does not provide the fact that the jet has a velocity gradient, but is useful to calculate the theoretical limitations for the process.

It was shown in the 1970's that this maximum velocity is 1.23 times the sound velocity C_0 for copper. If this velocity is exceeded during the forming process the material will produce a spray of particles instead of producing a coherent jet.

Hirsch and Mayseless [May07] found the reason for this effect in the compressibility of the material, which is normally ignored in the shaped charge theories. The high velocity compresses the liner material during the collapse, when the direction of the flow changes from towards the rotational axis along the axis. Then the material releases this inner pressure during its flow elastically. The resulting strain overvalues the strength of the material and forces the jet to particulate tangential to the axis, literally producing a spray of particles.

The factor for the maximum velocity differs for each material; Hirsch and Mayseless provided them as 1.231 for copper and 1.222 for aluminum.

B. CHARACTERISTICS OF THE PENETRATION PROCESS

General comments regarding jet formation and resulting material characteristics are presented in the following paragraphs along with specific features of the aluminum jet generated by the shaped charge fabricated and tested at the UIUC.

1. Penetration Process

As mentioned before, a shaped charge jet will achieve very high velocities of some kilometers per second²¹. The velocity when impacting the target will be higher than the sound velocities of the participating materials. The pressures will be much higher than any strength. Roughly said, the only parameter standing against the impact is the inertia of the target particles, like in the jet forming process. This assumed, the penetration of a solid target can be described very easily with the square root-rho-law. The basic requirement for this a high velocity of the penetrating material. The approach should not be used below $3 \frac{km}{s}$.

²¹High performance charge jets exceed $10 \frac{km}{s}$. The charge which is used in this research is relatively slow with a tip velocity around $6 \frac{km}{s}$, which is due to the relatively slow detonation velocity of the NM.

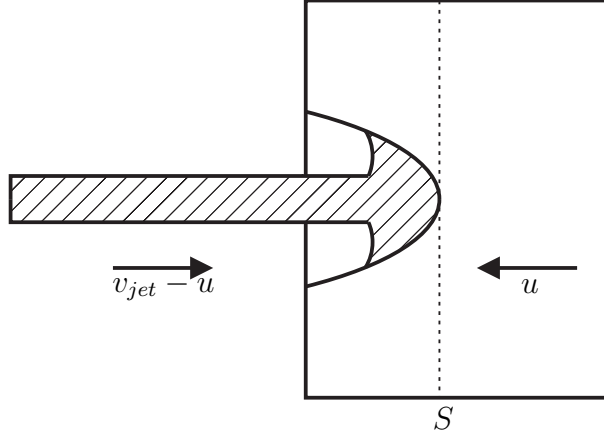


Figure 12: Principle of the penetration process [Zuk98]

The penetration can be seen as an adiabatic, stationary process in which shear strength of jet and target material can be ignored. Therefore the process can be imagined as a liquid jet penetrating a liquid target. In figure 12 the process is shown. If the origin of the coordinate system is in the point S , where the jet hits the target, the observer sees the target coming from the right with the penetration velocity u and the jet coming from the left with the jet velocity in the inertial system v_{jet} minus the penetration velocity²²:

$$v_{jet, \text{theoretical}} = v_{jet} - u \quad (9)$$

The whole process can now be described by a simplified Bernoulli formula, assuming that the ram pressure in the meeting point is equal on both sides:

$$\frac{1}{2} \rho_{jet} (v_{jet} - u)^2 = \frac{1}{2} \rho_{target} u^2 \quad (10)$$

Defining a penetration time t and knowing that the process is stationary and begins instantaneously, with the equation 11

$$\frac{l}{v_{jet} - u} = t = \frac{P}{u} \quad (11)$$

²²Compare [Sch10][Zuk98]

in which l is the length of the jet and P the total penetration depth, the ratio $\frac{P}{l}$ turns out to be

$$\frac{P}{l} = \sqrt{\frac{\rho_{jet}}{\rho_{target}}} \quad (12)$$

The penetration depth depends only on the length of the jet and the ratio of the densities.

2. Erosion of the Jet in Inert Materials

When the jet penetrates the target (and also when it moves through air) it erodes. Dolak [Dol08] gives a very detailed overview on the erosion and the involved influences on the jet material in his work. Following, the main properties are summarized.

Erosion in the jet and in the target is mostly caused by the inertia of the materials. Both bodies can be assumed as mass points with no connection to each other. The difference in velocities of the jet and the target particles forces them to transfer momentum, which leads to the known results²³. Both materials will flow away from the penetration point. This process will stop either when the jet ends or the jet particles are to slow, and the process begins to be influenced by shear strengths again, where it becomes very difficult to describe.

However, there are some effects that should be considered during the process, especially when slower parts are involved.

a. *Projectile Heating and Thermal Softening*

Of course the friction and the forming processes during the penetration will result in heating of the involved parts. The heating will be concentrated on the actual penetration front, because of the short time period the process takes. When a particle is heated up, it already will be eroded, leaving no realistic possibility to let the heat flow in the following parts of the jet. Therefore the zone of influence is very small on the tip of the jet.

²³Also discussed in IIA1

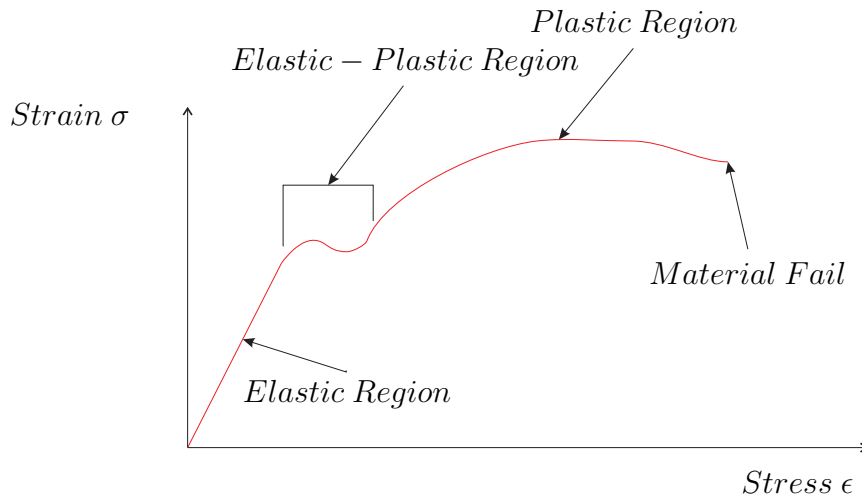


Figure 13: Example of a Stress-Strain diagram for steel

However, due to the short time the plastic strain on the material will lead to a adiabatic heating of the particles and the erosion front, which could have an influence on the erosion rate because of thermal softening. Still, the main reason for the erosion is the inertia discussed above.

b. Hardening Effects

If a material is suspended under stress, it reacts with elongation or strain. There are different stages of the deformation, starting with elastic strain over plastic strain, which will stay after the stress is released till the stress exceeds the material strength and it fails. Figure 13 shows an example for this material behavior.

In the penetration process, the stress usually exceeds the material strength by magnitudes, forcing the material to fail instantaneously. However, there is the effect of strain-rate hardening that should be considered.

The response of the material on stress depends on the strain rate²⁴. In a dynamic process the material is more resistant to stress if the strain rate is increasing.

²⁴There is also a hardening effect if the material is suspended to stress repeatedly.

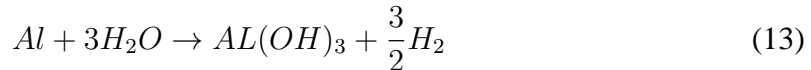
The effects of thermal softening and strain rate hardening are working in opposite direction. At high velocities their influence is considered to be relatively small. However, especially the heating of the particles can be very important because of their influence on the combustion process²⁵.

C. COMBUSTION OF METAL AND POTENTIAL ENERGY RELEASE

The difference in the mode of operation between a reactive and a non reactive shaped charge liner is in the energy release of the combustion of the active material, which in this work will be aluminum. To estimate this reaction a short review of the procedures is needed.

1. Reaction of Aluminum and Water

Aluminum is a very reactive material. Even in air, pure aluminum reacts instantaneously with oxygen to aluminum oxide or alumina. In water, which is rich in bound oxygen, the process also occurs. Dolak [Dol08] gives a detailed review of the reaction process and the released energy in water and also in hydrogen peroxide, which contains even more oxygen. The chemical reaction is described by formula 13 for the first reaction hierarchy.



This reaction will lead to a energy release of 99.3 *kcal* per *mol* or 15.4 *kJ* per *gram* of reacting aluminum.

Also the hydrogen reacts back to water, which releases an additional 68.3 *kcal* per *mol*.

²⁵See IVC

2. Potential Energy Release Approximation

The maximum possible energy release from the aluminum jet generated in the UIUC experiment can be approximated based on the PER theory and the known chemistry by a back-of-the-envelope evaluation.

The liner which Mason used in his work contains approximately²⁶ 22g of Aluminum as reactive material. As explained in equation 3 the mass of the jet is depending on the collapse angle β . The edge case where the mass reaches its maximum will occur when $\cos(\beta)$ reaches its minimum, therefore when β is 90. In this case the mass of the jet will be half the mass of the liner. In reality the jet mass will achieve values between 15 to 20% of the total liner mass.

The slug is not evaluated, because only the surface of the slug will oxidize. The jet will particulate while penetrating the target and could burn totally because of the big total surface of the particles.

Aluminum has a atomic weight of $26.98 \frac{g}{mol}$ [Pal02]. This leads to a amount of energy of $16kcal$ or $67.8kJ$ for the combustion of $4.4g$ of aluminum. The kinetic energy of the jet, which travels at a mean velocity of approximately $4 \frac{km}{s}$ will be ca. $36kJ$. Therefore the potential energy release is in the same magnitude as the kinetic energy of the jet, even if only 50% or less of the jet would react.

Nevertheless it must be considered that the combustion is a very slow process compared with the penetration; but after all the possible effect of the blast resulting from the chemical reaction could be very impressive, like seen in Masons Experiments.

3. Erosion in Reactive Materials

During the penetration of reactive material the additional chemistry has an influence on the process. Like recent experiments showed the jet is eroded more when penetrating reactive materials.

This stronger erosion is expected to be caused by two effects: (i) the reaction itself which influences the material structure and (ii) the heat resulting from oxidation.

²⁶See [Mas10], Table 4.2 ,p. 44

The reaction itself, if happening directly at the erosion front, weakens the structure of the material. When the aluminum reacts to alumina, the size of the molecules is increasing, disturbing the order of the material.

Additionally the resulting heat could increase the thermal softening up to potential melting of the material, which also would lead to more erosion.

Both effects are expected to have more influence in the slower parts of the jet, where the hydrodynamic penetration theory becomes more inaccurate and material strength must be considered.

D. DESCRIPTION OF PRELIMINARY EXPERIMENTS AT THE UIUC

Mason and Glumac [Mas10] did experimental work at the UIUC where a 50mm shaped charge with a reactive aluminum liner and nitromethane as explosive was fired into a stack of steel plates submerged by water and oil. Figure 14 shows the stack.

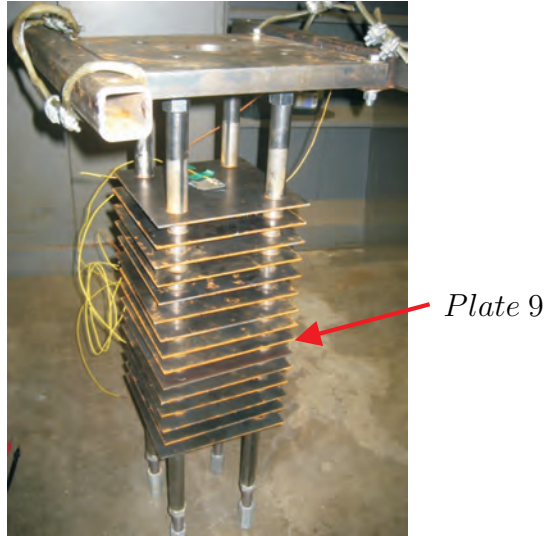


Figure 14: Picture of the plate array that was used in the experiments. The charge is set on the thick plate on the top. In the best tests the jet penetrated till the marked plate 9.

These experiments are the most important ones for this research, and are therefore described more detailed in this section. The basic submerged plate array and the tank are

described in appendix A. Also the liner and charge dimensions can be found in appendix B.

The experimental setup consists of the charge, the steel plate stack and a steel tank containing the stack and the fluid. The fluid level and the distance of the first plate to the basis of the charge is kept constant to maintain an equal stand off distance in all tests.

In the experiments several data was gathered of the jet.

The jet tip velocity was measured using a laser beam and photo diodes.

Also the time when the jet reached the plates was measured. A metallic foil was attached on top of each plate, isolated from that by adhesive and connected with a measuring wire. When the jet tip hit a plate, it closed the circuit between the foil and the plate. The resulting voltage drop could be measured, thus providing the time of arrival of the jet at this plate.

Three tests were conducted with this setup, two in water and one in oil. They are referred to as Test11, 12 and 13. An overview of these tests and the additional tests which were done during this research can be found in appendix C.

The observations are described below.

E. OVERVIEW OF EXPERIMENTAL EVIDENCE FOR THE REACTION

To study the effects of reactive jets a lot of work was done in the past. Early work on the NPS dates back to the 1980s ([Sha86] and [Koh85]).

Experimental work containing aluminum rods and reactive effects during penetration was done at the NPS and the Ernst-Mach-Institute by Dolak ([Dol08]).

Fant and Mason ([Fan08], [Mas10]) did experimental work at the University of Illinois in Urbana-Champaign.

1. Qualitative Evidence

Mason [Mas10] fired shaped charges into spaced steel targets, using different liners and sizes. Liner velocities and plate deformations were measured, supplemented by the measurement of time of arrival²⁷ data at the plates and velocity information.

He observed a very huge difference in the plate deformation when the aluminum jet was fired into reactive material, while in a test with oil as submerging liquid the plates were not deformed remarkably²⁸.

Figure 15 shows the deformation in the target for the water (left) and the oil (right) test. The red line marks the same plate in both arrays. This plate, plate number 10, was the first one which was not penetrated in both experiments. While the penetration performance was the same much more deformation was observed in the water test, being more than 10mm at the center while none was measured in the oil test at all.

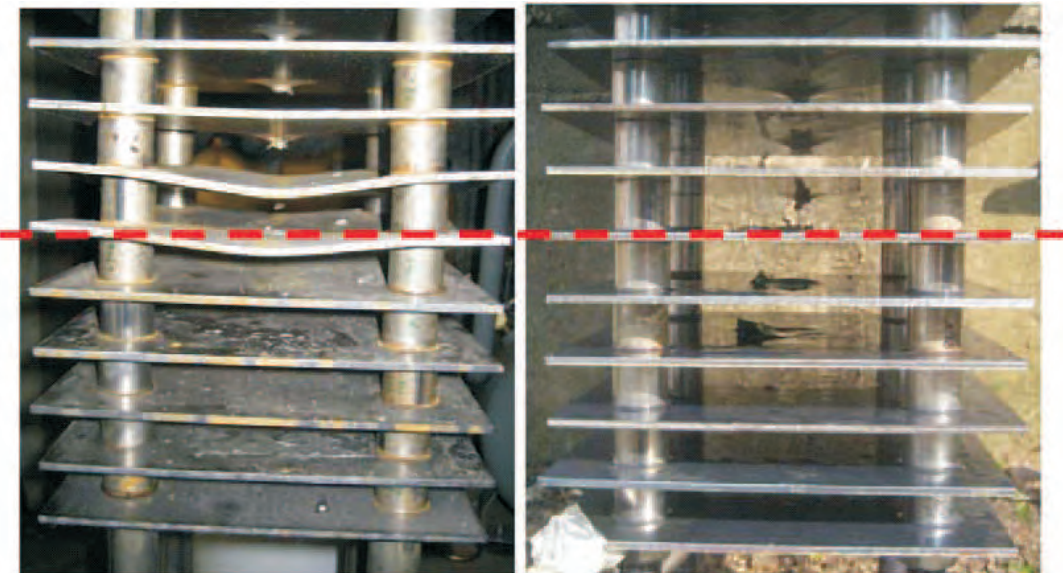


Figure 15: Comparison of the plate deformation in the water test (left) and the oil test (right). The red line indicates the same plate in both tests. Note the strong deformation in the water test.

²⁷TOA

²⁸The tests which are discussed in this thesis are mainly Tests 11, 12 and 13. While 11 and 12 used water, Test 13 used oil. A comparison of the deformation in Test 12 and 13 is provided in appendix D.

Also it was observed, that the deformation took place in the last plates mostly, before the penetration stopped. The effect seems to be much stronger from the tail of the jet.

2. Spectroscopy

During the work of Brian Fant [Fan08], who also fired aluminum shaped charge jets into plate arrays²⁹, the residual from the aluminum jet were analyzed, both in oil and in water and additionally in hydrogen peroxide which has even more reactive potential than water.

It was shown that much more alumina was formed when fired into the water or peroxide instead of the inert oil. This was done in two ways, by (i) finding a strong increase in the spectroscopic lines of alumina during the process itself and (ii) by analyzing the residual after the test.

The spectroscopic analysis of the collected residua is shown in table 3. Note that almost a third of the initial available aluminum has reacted in the H_2O_2 Tests, while only 5% of aluminum oxide was detected in the oil test.

Test Liquid	# of Tests	Collected Residue Mass in g	Percentage of Al reacted to Al_2O_3
Oil	1	1.33	4.8%
Water	2	1.78	$28.3\% \pm 1.5$
H_2O_2	2	1.47	$32.5\% \pm 6.8$

Table 3: Residual Analysis for the reactive jet fired into submerged steel targets [Fan08].

3. Calorimetry

Fant also measured the light emission during the penetration over penetration depth and time. The results can be seen in figure 16. The emission increases over the penetration depth, reaching its maximum right before the first not penetrated plate, where also the strongest deformation occurred. Additionally the emission lasted for more than 1ms, which makes it very likely to be caused by the combustion of the aluminum.

²⁹Fant also saw very impressive deformations, but used other plate dimensions.

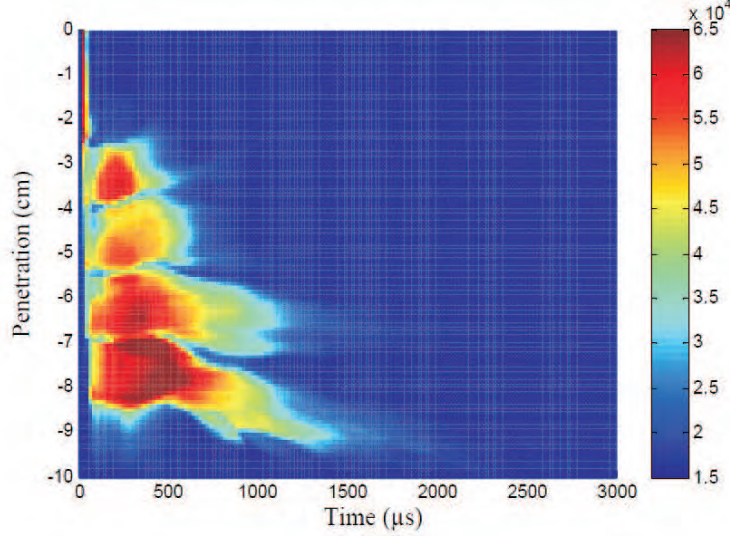


Figure 16: Light emission over time and penetration depth of a aluminum jet into stacked steel plates submerged by water from [Fan08].

4. Controlled Penetration Experiments

Dolak [Dol08] conducted experiments at the NPS and the EMI where aluminum rods were fired into target tanks filled with oil, water and hydrogen peroxide at a velocity in the area of 2700 to $3700 \frac{m}{s}$. Steel plates were mounted in the tanks to examine the penetration process.

He found strong evidence of increasing oxidation with the reactivity of the fluid, and a small trend to the increase of deformation of the target plates.

Recently realized tests are showing evidences for increasing erosion within reactive materials.

F. USING ANSYS AUTODYN FOR SHAPED CHARGE RESEARCH

Basis for all further research and simulations is the simulation of the jet and the investigation of its characteristics at the stand off distance.

Simulating shaped charges in AUTODYN is a very common technique. The credibility of the results was validated in many works³⁰ and the matching of simulations and experiments was found to be very good.

The following sections are providing a brief overview on the characteristics of the software and the setup which was chosen for the jetting simulations.

1. Basics of ANSYS AUTODYN Shaped Charge Calculations

ANSYS AUTODYN is a software for multiphysics computations. It contains different solvers and an extensive material library, including explosives.

There are two kinds of solver techniques which were used in this research, Lagrangian and Eulerian solvers³¹ and combinations of them.

A Lagrangian solver forms meshed bodies which are filled with material. During the computation process the mesh deforms. To maintain reasonable time steps³² degenerated cells have to be removed. Due to its characteristics the Lagrangian solver is suitable for structural mechanics, and certain penetration problems.

An Eulerian solver, on the other hand, consists of a stable mesh which forms an area and is filled with material in those parts which represent the calculated bodies. During the computation the material flows through the mesh. Therefore the Eulerian solver is suitable for fluid dynamics and, of course, explosions.

The calculation of jet forming processes is only feasible using Eulerian solvers. The reason is that the flow of the liner material would degenerate the liner cells in a way which would force the solver to erode most of them, which would keep their inertia and mass but not complete behavior. Additionally the time step would decrease strongly during the process.

³⁰To name an example, [Has10], [Duo05], [Dol08] or examples from the manufacturer in [SAS10]

³¹AUTODYN also provides the SPH or Smoothed Particle Hydrodynamics solver, which is mesh free.

³²The time step is one major parameter in FEM computations. It is the interval which is calculated in each circle during the computation. The time step is adjusted to the mesh size to ensure that no information, material or force (e.g. a shock wave) can travel further than one cell during the cycle to maintain accuracy, and therefore is calculated by the ratio of the dimension of a cell over the sound velocity of the material, or the fastest velocity occurring. Therefore a smaller mesh does not only lead to more cells to compute but also to smaller time steps, which both increases computation time.

2. Simulations of the Charge Used for the Research

Figure 17 shows the setup which was used in the jetting simulations. It matches the assembly of the charge used in the experiments described below, not including the detonator. Simulating the detonator would only increase the complexity of the simulation without providing more accuracy, so the charge is initiated by a line of detonation points instead of the detonator used. Differences between the simulation and the experiments are much more influenced by things like charge imperfections.

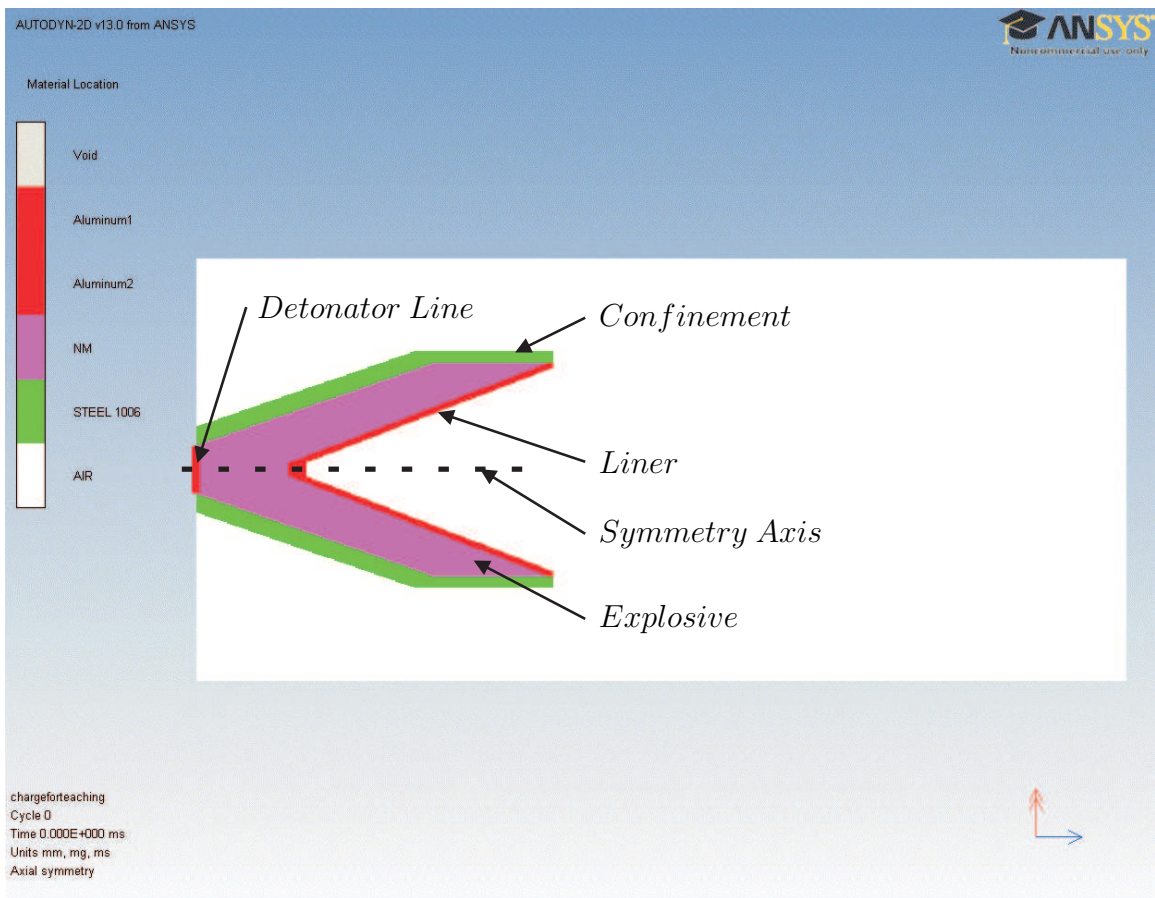


Figure 17: Setup of the UIUC charge used for the simulation.

The charge is simulated in a 2D- setup, which allows to keep the number of cells reasonable small.

The complete liner and confinement dimensions can be found in the appendices B and A.

3. Gathering Jet Information

The jet which is resulting out of this simulation is used in several parts of the this research. Figure 8 in section II3 shows the jet as it reached the stand off distance in the simulation.

All the jet data that was used throughout this research was gathered at this point. AUTODYN provides the possibility to remap data into other simulations, which allows to simulate the forming process itself once and using the jet in different calculations.

For the use of the jet data in MATLAB the PROFILE PLOT tool was used. This allows to export information along a linear path in the mesh. Every cell can be determined and the wanted data like velocity, density, internal energy or temperature can be extracted. This technique provides very detailed data of the complete jet.

Despite all its advantages AUTODYN cannot simulate all effects involved in the process. While the physical processes are all reproduced the chemical reaction involved is not included due to its very high complexity.

The simulation of the explosives, for example, is not calculated by the simulating the actual reaction but by using models describing the parameters mostly empirical.

Simulating combustion processes alone is a very complex and difficult issue, but simulating it in combination with the fluid and the penetration processes would be extremely difficult and beyond the scope of this research. Therefore other approaches must be developed to determine the observed behavior.

III. RESEARCH GOAL AND OBJECTIVES

Several properties and characteristics of the processes described above are unknown so far.

Although the combustion of the reactive liner material as the cause for the observed deformation in specific target plates is very likely, any other possibilities such as flow effects due to the submerging liquid or kinetic effects of the penetrating jet itself must be excluded.

Additionally, the amount of mass distributed in the various parts of the target and, linear to that, potential chemical energy is unknown. This information is crucial for further understanding of the process.

Furthermore the energy which is dissipated into plastic work in the target plates is unidentified.

The main goals of this research are to (i) analyze the penetration process to determine the jet portions and the mass distribution in the target which is responsible for the observed deformation and (ii) to estimate the energy needed to perform this deformation.

First of all a technique must be developed which allows to compute the penetration process. The high complexity of a multi material target in combination with the wide magnitude of involved velocities requires special methods of computing. This includes specific investigation on jet characteristics because this information is needed to estimate mass distribution in the different parts of the target.

Additionally, the simulations must be validated by comparing with available experimental data, and the reasons for eventually occurring differences must be determined.

Also a technique is needed which allows to estimate the mass distribution out of experimental data. The experimental results vary naturally due to differences in charge characteristics such as production quality and the mixture and state of the explosive.

Finally, different approaches need to be developed and tested to compute the deformation process. The chosen approach must not only deliver matching results but also provide energy information concerning the plastic deformation of the plate and, if possible, of the involved flow processes in the submerging liquid.

IV. NATURE OF THE PROBLEM

A. PROPERTIES AND PROBLEMS OF TARGET SIMULATIONS

Simulating the complete penetration process at once is very complicated due to the dimensions of the experimental setup, and the range of the involved velocities of the jet which vary over almost a magnitude. Two approaches were initially conducted.

A coarse full simulation was done to gather basic information about the behavior of the jet and to validate the simulation results with the experimental data. However, the technique is not feasible for finer meshes in reasonable computation times. It was observed that a common technique where parts are added over the time when the jet tip reaches the end of one part³³ produced very small time steps in the area of $1 \cdot 10^{-10} ms$ caused by the interaction between the parts, which would lead to simulation times of some decades. Simulating the process in this manner was found to be feasible only if done coarse, but still very slow due to the amount of cells needed to cover the dimensions³⁴. Therefore it was only done to get a basic comprehension of the process, and to compare the experiments with the simulations as far as possible.

The second approach involved a segmented series of computation. In this case the jet was modeled in small parts. Each part was used in a penetration simulation until it was completely eroded. This allowed the concentration on certain properties and events and, as a result, provided a reasonable explanation for the observed properties. It is described in section IVD³⁵.

Both techniques have disadvantages. The full penetration can only be very coarse and therefore does not provide data which is detailed enough. The partial approach lacks

³³This is explained, for example, in [Duo05]

³⁴The nine plates and the matching space which where penetrated in the experiments are almost 300mm in the axial dimension.

³⁵The approach was developed and used in [Pet11]

of specific properties of the jet, especially the elongation³⁶, which means that it cannot not be used to estimate the properties of the complete process.

The technique which was finally used is described in VB.

B. DIFFICULTIES IN FLUID MODELING FOR TARGET PENETRATION CALCULATIONS

The basic penetration law which is used in most shaped charge research and was explained in IIB bases on the assumption that the target strength and the jet strength are much smaller than the ram pressure which is applied to the material by the inertia of its mass.

During the penetration this assumption tends to lose accuracy with decreasing velocity. The reason is that the influence of the strength of the penetrator is increasing, while there still is no strength in the fluid at all. This leads to a smaller erosion rates than expected, and the erosion of the jet is decreasing vastly below velocities of $3 \frac{km}{s}$ [Eld99].

Orphal and Anderson [And99] are providing a possibility of adjusting the penetration law by including a projectile strength Y_p and a target resistance R_t into the equation.

The problem of adapting this possibility to the target which is handled in this research is the mixture of materials. While the strength of the steel plates is at least in the magnitude of the aluminum, the fluid does not have a strength at all.

This fact has a big influence on all simulations and deliberations, and it shows the difficulties of estimating and describing complex penetration processes.

C. CHARACTERISTICS OF METAL COMBUSTION

The virtue of a reactive liner is the energy release of the combustion of the liner material. This reaction is a very complex process, influenced by many parameters. The following sections will give an overview over the main effects.

³⁶See also I3a

1. Description of the Combustion Process

There are three stages of the combustion [Sha86]. First, the particle needs to be ignited. Second, it produces heat, keeping the combustion process stable. In the end the particle either (i) has completely reacted, (ii) is covered by a thick layer of oxide and therefore is separated from the oxidizer or (iii) the radiated heat into the environment is too high, which leads to cooling of the particle till the activation energy for the process can not be achieved any longer.

After consuming the activation energy, the process delivers energy during the reaction, producing alumina and, in a water environment, hydrogen.

2. Ignition

Aluminum particles are always covered with an oxide layer. To let the material react, this layer must be destroyed.

Beckstead [Bec07] summarizes several ignition predictions and experimental results. One way of igniting the material is to increase its temperature till the melting of the oxide layer. For Al_2O_3 the melting point is at $2300K$ ³⁷. Beyond this point the layer loses its integrity, allowing the aluminum to react.

By contrast it was observed in experiments, that ignition occurs at lower temperatures between 2000 and $2100K$, leading to the conclusion that the integrity is lost before the alumina is melting. There is also speculation that shell cracking at lower temperatures which exposes pure aluminum to oxygen can lead to reaction.

Finally, mechanical stress like in a shock wave can likewise deflect the layer and giving it the chance to ignite at relatively low temperatures.

The temperature needed for the process is depending on the actual setup. If the aluminum is not influenced by shocks and therefore the oxide shell is intact, no ignition will appear below the very high melting temperature of the alumina. But if the layer is mechanically destroyed or damaged, the reaction will start at very low temperatures if oxygen is available.

³⁷The melting point of aluminum is much below at $933K$.

3. A Simple Burning Law for Spherical Particles

The process can be described with a simple burning law³⁸. The needed assumptions are that the particle is (i) a sphere, (ii) consists only of pure metal and (iii) will burn uniformly.

Then, the rate of burning mass fraction per time will be:

$$\dot{m} = -\frac{dV}{dt}\rho = -\frac{\pi\rho}{4} \cdot \frac{dD^3}{dt} = -\frac{\pi\rho D}{4} \cdot \frac{dD^2}{dt} \quad (14)$$

The rate of reactive area decrease is then

$$-\frac{4\dot{m}}{\pi\rho D} = \frac{dD^2}{dt} = \text{constant} = \beta \quad (15)$$

The equation can now be solved for the change of diameter over time:

$$D^2 = D_0^2 - \beta t \quad (16)$$

This law is the D^n law.

It was observed in experiments that the exponent is smaller than two and closer to the area of 1.5 to 1.8³⁹. In the real process the surface will not burn uniformly; some areas will be more or less covered with oxide.

The value of β , however, depends on many parameters of the environment, like the oxidizer, the pressure, the temperature and so on. Experimental data for burning particles by Shavit [Sha86], which was validated by Glumac at the UIUC, can be used to estimate β . Shavit found that a particle with the size of $6\mu\text{m}$ in a steam environment will react completely within a time of $200\mu\text{s}$. with $D = 0$ at this time β will be $\beta = \frac{D_0^{1.5}}{t}$. This gives a value of $7.4 \cdot 10^{-5} \frac{m^{1.5}}{s}$.

³⁸For the burning law and the additions compare with [Bec07]

³⁹Beckstead refers this values to [Gok96]

D. CHARACTERISTICS OF THE JET COMBUSTION

To understand the combustion process and the effects which were observed in the experiments, preliminary work was done [Pet11]. The findings are describing the jet properties which have an influence on the process and are described below.

1. Jet Properties

The dimensions used for the shaped charge were the same as in the experiments at the UIUC by Mason. The liner dimensions are presented in appendix B. The explosive is nitromethane.

To gather the jet information a simulation of the shaped charge Mason used in the experiments was done. The calculation was stopped when the jet tip reached the stand-off distance of $190mm$. The needed data was collected and processed using a MATLAB function, cutting of parts with velocities under $1500\frac{m}{s}$ and dividing the remaining $164mm$ jet into 20 parts with an equal length of $8.2164mm$, each described with their respective internal energy, temperature, radius and velocity to be the jet parts used for the target simulations.

2. Mass Gradient along the Jet

The mass per length unit ratio differs along the jet, like explained in I3d. The difference is almost in the order of magnitude. This mass gradient leads to a gradient in the chemical energy which is crucial for the power of the combustion. Figure 18 shows the chemical energy of the created jet parts⁴⁰ over the x-dimension of the jet, not including the tip.

⁴⁰Represented by the blue stars.

Chemical Energy in kJ

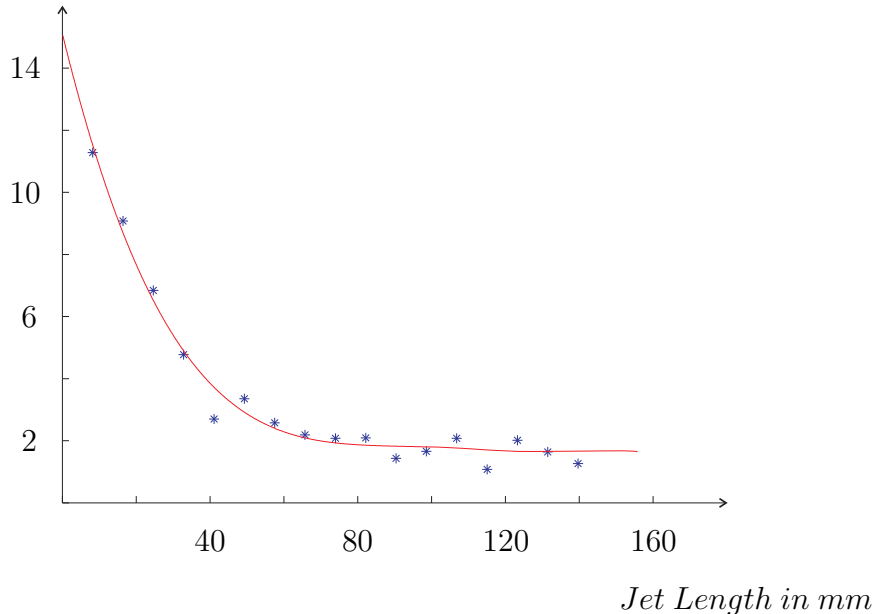


Figure 18: Possible chemical energy release of the simulated jet parts over the x-dimension. The parts are marked with the blue stars.

3. Example Penetration Simulations

a. Penetration Behavior of the Jet Parts

Figure 19 displays the situation of the parts after the penetration process. While the fast parts are completely eroded, like predicted with the hydrodynamic theory, the slower parts are partially unimpaired.

This difference in the penetration behavior shows the complexity of the process, where the influence of the strength of the involved materials is increasing with the decrease of the jet velocity. Especially in the water parts, where the jet has a material strength while the fluid has none, the behavior changes strongly. This has also an influence on the heating of the jet, like explained below.

b. Temperature

In both cases the eroded parts are showing increased temperature after the penetration.

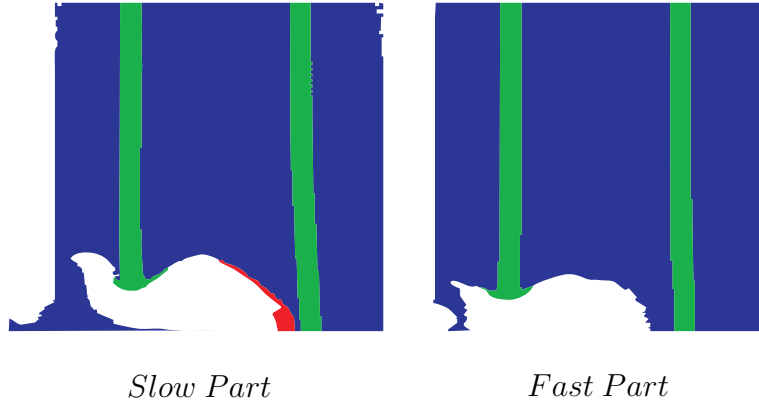


Figure 19: Comparison of the slow and the fast parts during the penetration

The temperature varied during the simulation. When the jet first hit the first plate peak temperatures occurred up to $2000K$ for short periods of time. The average temperature of the eroded material was much lower at areas between 800 and $900K$. Figure 20 gives an overview of the temperature in the jet during the penetration of the first target plate.

In both cases the increase of temperature seems to be enough to ignite the material. Due to the additional destruction of the oxide layer because of the erosion a reaction is very likely in both cases.

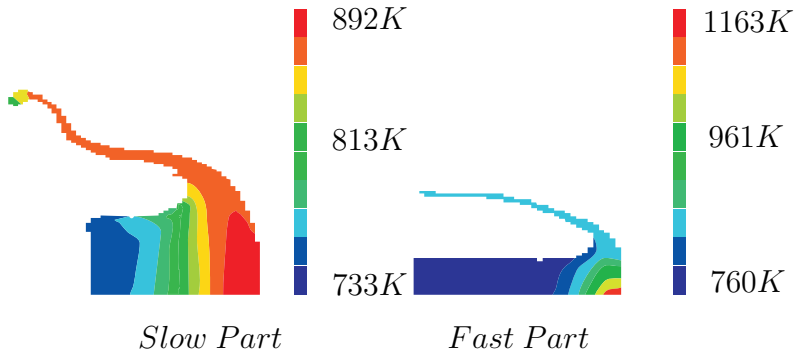


Figure 20: Absolute temperatures of the slow ($1527\frac{m}{s}$) and the fast ($5724\frac{m}{s}$) parts of the jet during the penetration

Dolak [Dol08] observed much higher temperatures in the erosion front during simulations. This is believed to be caused by the definition of the mesh, which could lead to the loss of peak values.

c. Particulation and Surface

The fast parts show a expected behavior of particulation; the small amount of available mass and the strong erosion are leading to a wide spreaded cloud of material along the penetration path.

The slow parts are staying unimpaired, due to the influence of the material strength in the slow penetration. Still, the erosion produces a big surface.

In both cases the material is forced to flow, which will destroy the oxide layer, producing free material for the combustion.

The observed behavior leads to a possible explanation why the strong deformation in the experiments was observed in the last penetrated plates.

All parts of the jet fulfill the requirements for the combustion, (i) being vastly deformed which destroys the oxide layer and (ii) being heated up to critical temperatures during the penetration process.

The slower parts are carrying up to a magnitude more mass and therefore chemical energy. This fact is believed to be the reason for the much stronger combustion effect.

E. MASS DISTRIBUTION BETWEEN THE TARGET PLATES

As explained above, gradient of mass which is distributed between the plates seems to be the main reason for the difference in the observed deformations along the penetration path.

The information about the mass gradient is gathered out of the simulation results of the jet forming. The characteristics of the jet are therefore known, and the general information which parts of the jet will be eroded in which parts of the target can be approximated

in a reasonable way. However this is only a quantitative description about the ratio of available mass along the penetration path. The exact amount, especially the differences between the experiments is unknown further on.

Therefore an approach must be found that is able to estimate the exact mass of aluminum available in the different parts of the targets. This must be possible out of available experimental data.

F. QUANTIFYING THE ENERGY RELEASE DURING THE COMBUSTION

The process of the combustion during the penetration is very complex. It includes mechanics, fluid mechanics and chemistry; no hydrocode supports this combination. It is therefore impossible at this moment to simulate the complete process with all its effects.

While the fluid dynamics can be calculated very good with AUTODYN and similar codes, the chemistry can not be determined.

To quantify the energy release during the combustion special techniques must be used. The following sections are introducing some possibilities.

All techniques have one thing in common: they provide a specified amount of *energy*, which is released and contributes work on the target by deforming it. The source of the energy differs.

In every approach it has to kept in mind that the process is basically like a part of a joule process, where chemical energy is dissipated into the actual plastic work on the target plate and the thermodynamic losses occurring from the creation of entropy during the expansion and the flow processes.

1. Compressed Air

Using a sphere of compressed air as a source of energy is one possibility. If the pressure of the sphere is larger than in the space surrounding it it expands, dissipating its internal energy to the environment.

The easiest EOS for a gas is the *Ideal Gas Law*, which describes the behavior of a hypothetical gas⁴¹:

$$pV = nRT \quad (17)$$

The ideal gas law is the result of some simple assumptions. Basically (i) the volume of the molecules and (ii) the cohesion between them is ignored, which means that there is now interaction between the molecules whatsoever.

a. Internal Energy of a Compressed Air Sphere

Considering the air being a ideal gas, the energy stored in a sphere of compressed air can be described by equation 18:

$$E_i = \frac{nR}{\kappa - 1} T = \frac{pV}{\kappa - 1} = \frac{4}{3}\pi r^3 \frac{p}{\kappa - 1} \quad (18)$$

This equation shows the two degrees of freedom of the EOS: the pressure and the radius⁴² of the sphere.

Figure 21 shows the resulting internal energy for $p-r$ -pairs. The area marks the possible combinations. The gas can only be in a state described by this area.

Every process will take place anywhere in this surface. The fact that the process has two degrees of freedom makes it relatively easy to adjust it to the current deformation, because the final radius is already known, which leaves only the pressure and the initial radius to adjust.

2. High Explosive

Another possibility is to use high explosive as a source of the deformation energy. The main difference to the compressed air bubble approach is the impossibility to choose the initial pressure. Due to the properties of the explosive it reacts extremely fast⁴³.

⁴¹Compare e.g. [Car95]

⁴²Respectively the volume

⁴³The reaction time is in the order of some microseconds, while a combustion process takes place in a millisecond magnitude.

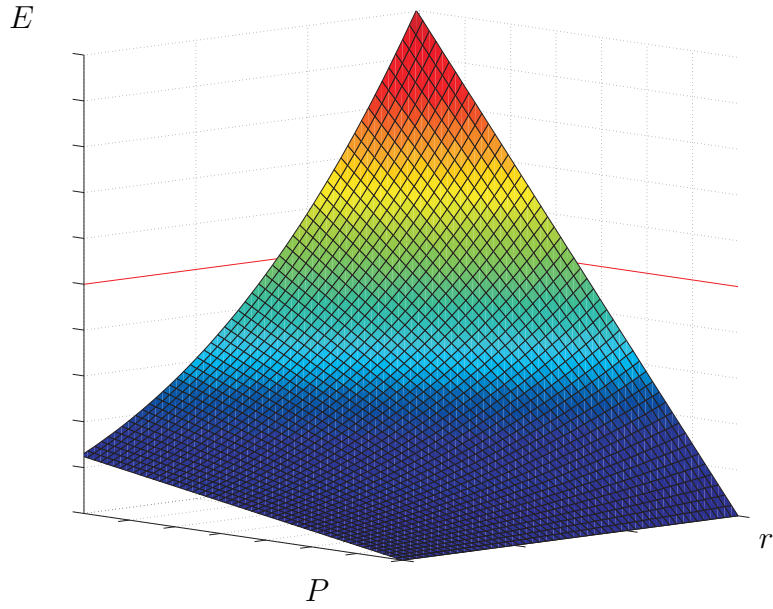


Figure 21: Internal Energy of a compressed air sphere over radius and pressure.

The explosion process is calculated using a JWL EOS⁴⁴. After the initial expansion the EOS is changed to an Ideal Gas to be more accurate. This basically justifies even more the approach using compressed air bubbles, because the technique is basically the same without the strong influence of shock which is included when using explosives.

An advantage of using high explosives as an energy source is the fact that the process contains a reaction, which makes it much more like a combustion process. Additionally the amount of chemical energy which is available is known and can be fitted to the expected amount of chemical energy of certain parts of the real jet.

A disadvantage, which should be considered when comparing the simulation with experimental results is the difference in the time magnitude. The involved materials will show different reactions on the influences during the process depending on their velocities.

⁴⁴The Jones-Wilkins-Lee EOS is an empirical EOS, describing the pressure in the expanding gas with

$$P = A \left(1 - \frac{\omega\eta}{R_1}\right) e^{-\frac{R_1}{\eta}} + B \left(1 - \frac{\omega\eta}{R_2}\right) e^{-\frac{R_2}{\eta}} + \omega\rho e \quad (19)$$

where $A, B, R_{1,2}$ and ω are empirical constants, $\eta = \frac{\rho}{\rho_0}$ and e is the specific internal energy [SAS10].

3. Evaluation of the approaches

After both approaches were tested, it was found that neither the bubble expansion nor the explosive expansion can be used to gather the wanted information. The main problem is that the process is much too complicated to be simulated entirely. The combination of the plastic strain in the plate with the highly turbulent fluid calculations leads to heavy oscillations and cavitation due to the shock wave. Most of the influencing parameters for the flow process can not be estimated in reasonable quality, which means that the results are not trustworthy in a reasonable magnitude.

Additionally the needed combination of Eulerian meshes for the fluid calculations with the Lagrangian meshes for the plates, which becomes necessary due to boundary condition requirements leads to uncertainties and long computation times.

Finally an approach using WORKBENCH was chosen, mostly due to its simplicity and the credibility of the results. It is introduced below.

4. Estimating the Energy Release with ANSYS WORKBENCH 3D Explicit Dynamics Calculations

The approaches explained above are trying to describe the process as close to the actual events as possible, by including the fluid dynamics of the displaced water and the plastic deformation of the solid plates by implying a energy source into the actual setup.

Using Explicit Dynamics calculations is a total different approach. The technique concentrates on the mechanical plastic work which is dissipated in the plates.

In contrast to the other explained techniques the energy source itself and its behavior are not part of the simulated process; instead the deformation of the plate is caused by a pressure load. Therefore the simulations can be done in 3D, including the complete geometry of the actual target plates, because much less cells are involved when the same definition is used.

Also the penetration process of the jet itself can be simulated with the actual plate geometry, which allows measurement of the deformation caused by the kinetic energy loss during the plate penetration when compared and validated with the experimental results.

THIS PAGE INTENTIONALLY LEFT BLANK

V. TECHNICAL APPROACHES

A. COMPARING INERT AND REACTIVE MATERIALS IN EXPERIMENTS

1. Used Active and Inert Materials

To estimate the virtue of a reactive liner one needs to compare its effects in a reactive environment with the effects in a inert one. This is necessary to focus on the reaction of the liner and material. To fulfill these requirements a comparable liquid to water must be found, and the unavoidable differences must be considered.

In all of the preliminary experiments oil was used as a replacement for water. It is obvious and was observed, that no reaction with the oil occurs in the experiment. However, it has to be evaluated if the results are comparable or not.

2. Estimating the Difference using Square Root Rho Law

The easiest way to estimate the comparability is to use the penetration law mentioned in section IIA1. It can be simply found that the ratio of the penetration depths should be the square root of the inverse densities:

$$\frac{P_{Oil}}{P_{Water}} = \sqrt{\frac{\rho_{Water}}{\rho_{Oil}}} \quad (20)$$

The density of water being $0.998 \frac{g}{cm^3}$ and the density of the used *Hygold L750* from Ergon being $0.92 \frac{g}{cm^3}$ ⁴⁵, the penetration depth of the same rod should increase by 4% when impacting oil instead of water.

3. Estimating the Difference using AUTODYN Impact Simulations

Dolak [Dol08]⁴⁶, who examined aluminum rods impacting water filled targets together with the Ernst-Mach-Institute in Germany, performed AUTODYN simulations in order to gather information about the influence of the density when the rod was impacting

⁴⁵From the data sheet provided by the manufacturer.

⁴⁶See also section IIE

	Water	Oil	Difference
Sqrt Rho Penetration Depth	158.0mm	164.7mm	4.2%
AUTODYN Simulation Depth (apprx.)	155.0mm	160.0mm	3.2%

Table 4: Comparison of penetration simulations of a 50mm copper rod with 10mm diameter fired into semi-infinite fluid target containing water and oil, respectively.

monolytic steel targets with a velocity of $2700 \frac{m}{s}$. He used water with a shock equation of state and a Hydro (Pmin) failure model, which is implemented in the AUTODYN material library. He varied the densities between 0.5 and $1.5 \frac{g}{cm^3}$ and showed the differences plotting the average x-velocity over the time, which gives a good idea of the penetration process.

To quantify the differences target simulations where done. They contained a 50mm long and 10mm in diameter copper rod with a density of $8.94 \frac{g}{cm^3}$ impacting a semi-infinite target of water and oil, respectively, at a velocity of $5000 \frac{m}{s}$. A shock EOS⁴⁷ already implemented in AUTODYN was used for the calculation. The difference just occurs in the different density, leaving all other parameters the same.

During the simulation the average velocity of the penetrator material is measured. This velocity contains the parts of the penetrator that are not under any influence of the target material and still are moving with the initial velocity as well as parts which are directly in the erosion front or already eroded. Therefore this data provides very good information about the penetration process. The smaller the difference between this average velocity over time between two different target materials, the smaller the difference in the target resistance is, and vice versa.

The results are presented in table 4.

Only a small difference in the penetration depths could be observed. The result becomes more obvious if the average velocity of the copper in the x-axis is compared like in figure 22.

⁴⁷This EOS describes the Material in a Grneisen-Form. It establishes a linear relationship between the particle velocity u_p and the shock velocity U_s , combined with two parameters C_1 and S_1 [SAS10]: $U_s = C_1 + S_1 u_p$ This allows to describe any relation between the properties before and after the shock wave. For the material properties, see appendix G.

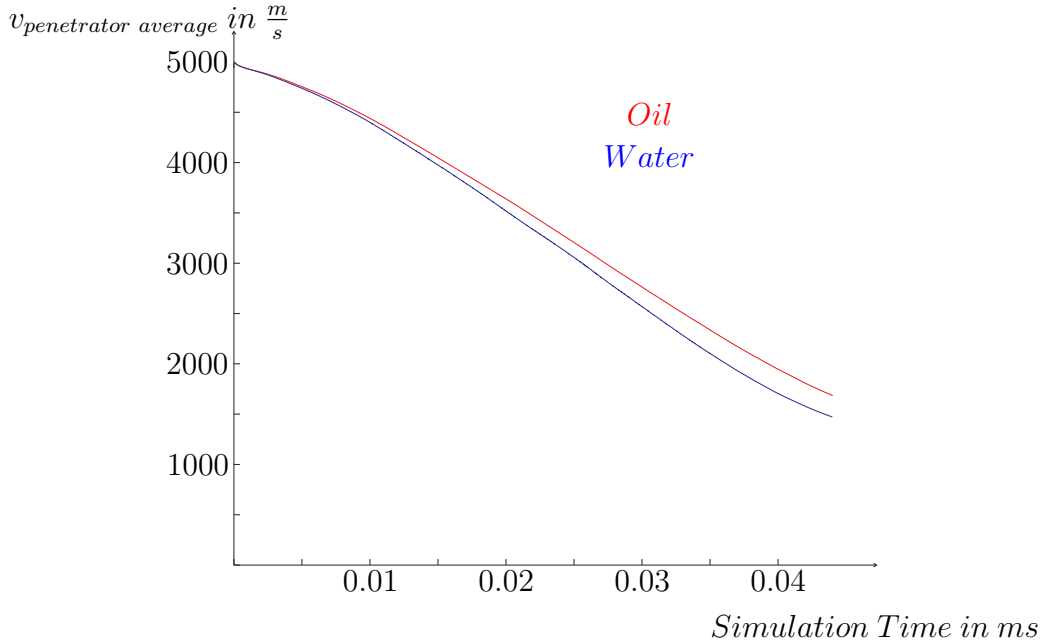


Figure 22: Average 50mm copper rod velocity during penetration of a semi-infinite target containing water and oil vs. time

4. Discussion of other Potential Influencing Parameters

So far the only influencing parameter was the difference in density between water and oil. The question is whether there are other material characteristics which maybe would leave a remarkable footprint on the results of the experiments. Those could be differences in the

- specific phase changes
- shear and bulk strength
- viscosity
- friction and abrasion.

All of those could possibly have an influence.

To simulate all these influences the material model has to be modified in its parameters. Most of the literature dealing with EOS and EOS parameters⁴⁸ treat solid materials

⁴⁸e.g. [Ste96]

because there are mostly involved with those calculations. Even if properties of liquids⁴⁹ are handled the EOS are very limited due to the inaccuracies next to critical points. Also finding values to fill an EOS for the special used oil would need experimental data which, of course, could not be provided for this certain issue due to the costs.

However, the process is still a hypervelocity one and therefore many of these can be ignored or at least estimated as very small. The pressures for example will exceed the shear strengths by some magnitudes. Friction and abrasion will hardly occur due to the cavitation effects while impacting. If there would be phase changes, they will happen in a distance from the rod.

To calculate the influence of other parameters than the density, simulations using polyethylene as target material are a very good method.

5. Additional Simulations using Polyethylene as Substitute

To make a worst case estimation of the potential additional influences on the penetration process polyethylene was used, which is a solid material.

Polyethylene has nearly the same density as the *Hygold L750* with a density of $0.916 \frac{g}{cm^3}$ ⁵⁰. Also it is implemented in the Material Library of AUTODYN. The material model includes, in difference to the fluids, an EOS with shear strength. If the difference between the target materials with all this influences included still stays reasonable small, those influences can be neglected and the oil substitution is justified.

The results of the additional polyethylene simulation can be seen in figure 23. The difference in average velocity is bigger than between oil and water; however the mean difference is 6.9% which is still small.

The small appearing differences in the results justify overall the use of materials with slightly different densities to examine the reactions. Varieties due to machining tolerances and other influences are considered to be in the same magnitude as the gap in density

⁴⁹e.g. [O'C01]

⁵⁰See [Lab80]. Also the Parameters for the EOS are given.

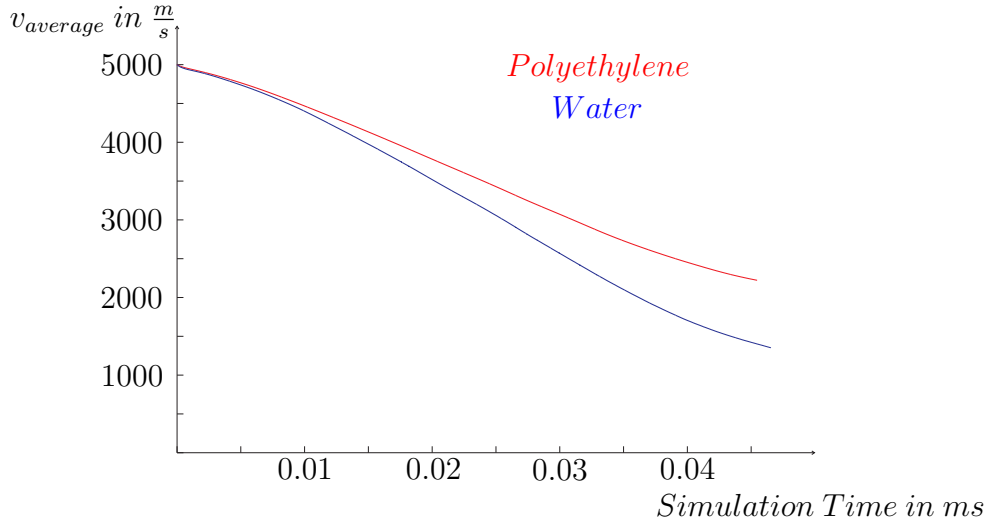


Figure 23: Average 50mm copper rod velocity during penetration of a semi-infinite target containing water and polyethylene vs. time

of ca. 10%.

Additional validation is gathered when the TOA data at the actual target of a oil and a water simulation is compared, which was done during the process of the work.

B. THE "DIVIDE AND CONQUER" TECHNIQUE TO SIMULATE THE TARGET PENETRATION

The "Divide and Conquer" technique combines the ideas of both approaches described in section IVA, allowing to simulate the process with a relatively fine mesh in a very short time.

The basic idea is to simulate small sections of the target. When the jet reaches the end of the section, the simulation is stopped. Then every material instead of the jet is deleted, which allows to write the jet into a datafile. This data is filled in the next simulation, where the process is redone. The jet is "carried" along simulations, containing its full data and being eroded over the time without the problems of very big parts.

The simulation of a small section can be done very fast, with a section having dimensions in the area of 50mm, even if a fine mesh is chosen.

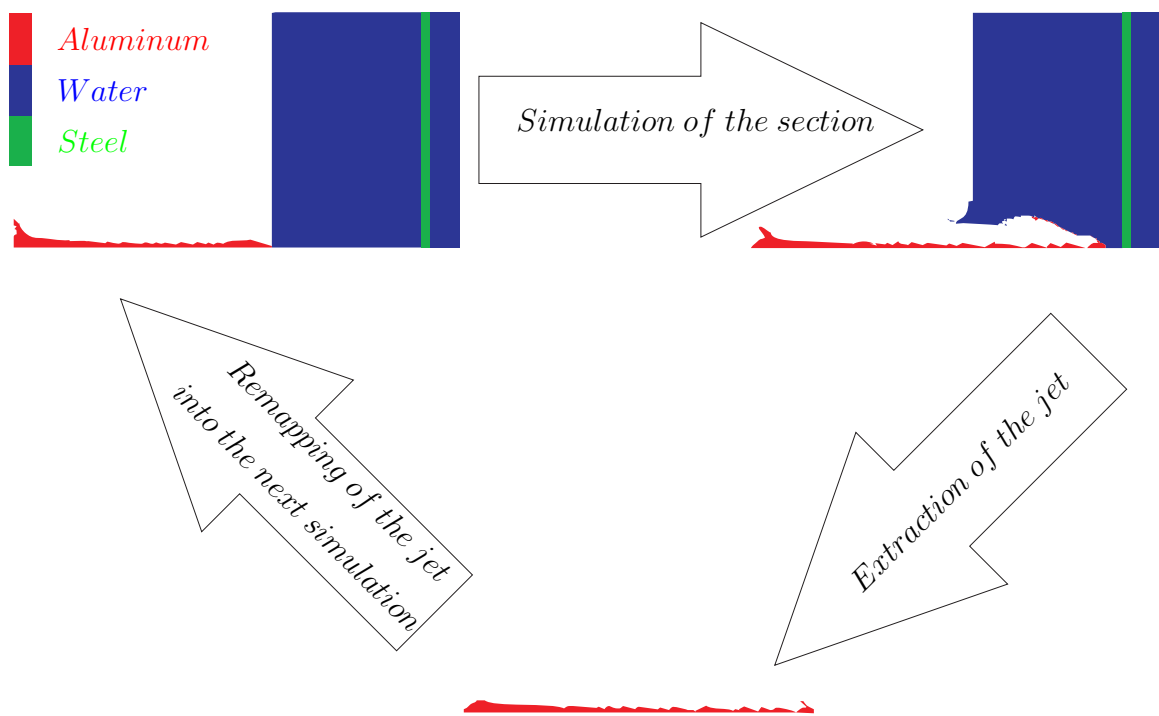


Figure 24: Principle of the "Divide and Conquer" technique to simulate the penetration process

Additionally, if the time step decreases due to particulation or if the debris from the target plates produces numerical failures like over-emptied target cells, the simulation can be stopped and the jet can be "cleaned" from this specific areas which are not necessary for the results.

Figure 24 provides the principle of the approach. First the jet is simulated while penetrating through a target section. Than the simulation is stopped and the jet is extracted by mapping it into a datafile. Now it can be remapped into the next simulation, and the process restarts.

This approach allows to simulate a penetration in very short times even if fine meshes are used. The results where validated with the coarse simulation mentioned above as well as the experimental data and found to be matching.

C. ESTIMATING THE MASS DISTRIBUTION

To estimate the mass distribution between the plates along the penetration path is a crucial information to (i) be able to explain the different deformation in the target and to (ii) validate the calculated energy amount for this deformation.

Two approaches where used; one using only the simulation results, the other connecting the experimental data with the known jet properties. Both are explained below.

Both approaches need the the jet characteristics explained in section I3d.

1. Mass Distribution in the Target Simulation

During the target simulation the TOA at the plates and the jet velocity at this points where measured. Knowing the cumulative mass⁵¹ matching to the jet velocity, the amount of mass which is eroded between two plates can be calculated as the matching difference in jet mass for the velocities at the plates.

Like explained in section IVA3 the penetration depth of the simulation and the one observed in the experiments differ. The simulation can therefore only provide a possible range of distributed mass. The minimum of this range is defined by the mass which is

⁵¹Compare figure 10.

distributed out of erosion between two plates. The maximum would be the total mass which is left in the jet after it penetrated the plate which was the last one in the test⁵². This maximum depends strongly on how the limit for the jet is set, meaning below which velocity the jet parts will not travel up to the place of interest.

2. Technique to Estimate the Mass Distribution out of TOA Data

The wide range of possible distributed mass out of the simulation is unsatisfying. To narrow this possible area, an additional approach was used.

This approach is only possible if some assumptions are made and is naturally not absolutely precise. However, it provides a good estimation of the distributed mass, and the assumptions are reasonable.

The basic idea is to use the TOA data out of the experiments to calculate penetration velocities along the penetration path. Out of the penetration velocity the initial jet velocity can be estimated, and this information can be used to get the distributed mass out of the cumulative mass information like above.

The penetration velocity, the velocity at which the penetration point travels into the target⁵³, can be defined as $u = \frac{dx}{dt}$.

Assuming that the jet velocity over its x dimension is a linear function, which is correct in a reasonable range⁵⁴, the penetration velocity over the penetration depth should also be linear, and u being the derivative of the penetration depth to the time, the TOA and the plate numbers⁵⁵ should follow a quadratic correlation.

In figure 25 the average TOA data for the water experiments (in red) and the resulting quadratic fit are plotted, with the function for the fit being $P(t) = a\frac{1}{s^2} \cdot t^2 + b\frac{1}{s} \cdot t + c$.

The derivative of this polynomial delivers directly the penetration velocity of $u = \frac{dP}{dt} = 2a \cdot \frac{1}{s} \cdot t + b$.

⁵²Which is plate number 9.

⁵³Compare I1

⁵⁴Compare I3a, figure 9

⁵⁵Or the penetration depth, respectively

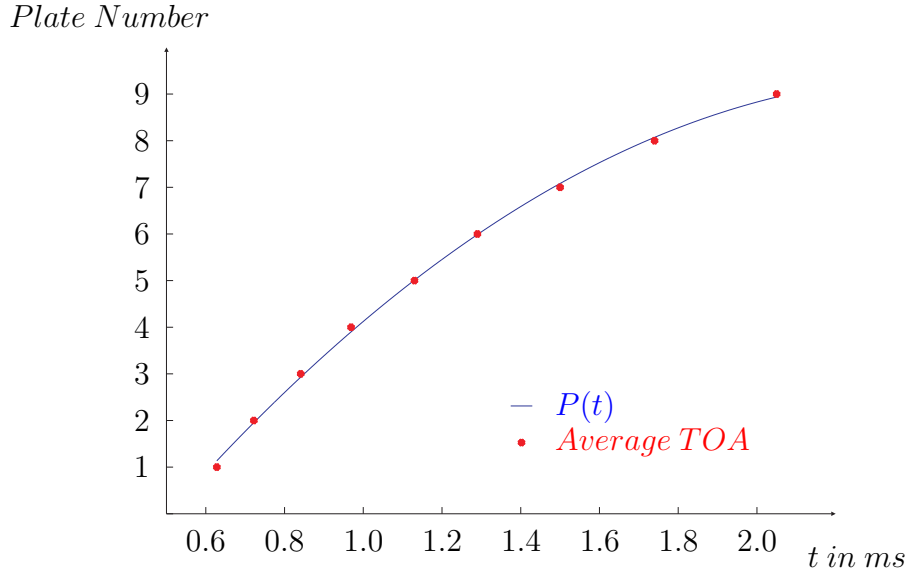


Figure 25: Average TOA of the experiments with water as submerging fluid (red points) and the matching quadratic fit (blue line).

The main assumption in the total approach is the connection of the penetration and the jet velocity. Knowing equation 10, the jet velocity should be like in equation 21:

$$v_{jet} = u \cdot \left(\sqrt{\frac{\rho_{target}}{\rho_{jet}}} + 1 \right) \quad (21)$$

or $v_{jet} = \psi \cdot u$, where ψ equals $\sqrt{\frac{\rho_{target}}{\rho_{jet}}} + 1$.

The problem is to find the target density. In the experiments multi-layer targets were used. The difference of the densities of steel and water is very big, with the water having a density of $1 \frac{g}{cm^3}$ and the steel having approximately $7.9 \frac{g}{cm^3}$. Therefore a theoretical combined target density must be estimated.

Theoretically, this density can easily be found by using the square root-rho-law, assuming that the same amount of jet must be eroded away over the same distance by the actual target and the theoretic material:

$$l_{Real\ Target} = l_{Theoretical\ Target} \quad (22)$$

When the real target is described by the distance of steel s and the distance of water w , the relation is

$$s \cdot \sqrt{\frac{\rho_{steel}}{\rho_{jet}}} + w \cdot \sqrt{\frac{\rho_{water}}{\rho_{jet}}} = (s + w) \cdot \sqrt{\frac{\rho_{target}}{\rho_{jet}}} \quad (23)$$

and finally delivers the theoretical density in equation 24

$$\rho_{target} = \left[\frac{s\sqrt{\rho_{steel}} + w\sqrt{\rho_{water}}}{s + w} \right]^2 \quad (24)$$

which will deliver a value of $\rho_{target} = 1.505 \frac{g}{cm^3}$. This will result in a value for ψ of 1.735.

By comparing the simulation results, which fit very good in terms of tip velocity and the TOA in the first plates, ψ was found to be in the area of 1.993, which would lead to a higher theoretical target density of $2.745 \frac{g}{cm^3}$.

The main reason for the difference is the difficulty to describe multi-material targets with the strong changes in the properties along the penetration path with such easy formulas. Especially while penetrating the water parts the penetration theory is slightly uncertain, where the jet has a remarkable strength if compared with the water, like explained above.

Additionally inequalities in the target, like differences in density are leading to resistance for the jet, which would lead to a higher theoretical density. The jet faces several sudden density alterations while it is traveling through the target, which would explain the higher value.

The correction using the simulation shows good results and was chosen.

The velocity of the jet at the actual point of the target can now be calculated, and the mass distribution information can be gathered like explained above.

This information is needed additionally for the approach described below.

D. PLATE PENETRATION SIMULATIONS IN ANSYS WORKBENCH 3D EXPLICIT DYNAMICS

To separate the deformation which is caused by the loss of kinetic energy of the jet during penetration from the penetration which is believed to be caused by the chemical energy of the combustion the penetration process was simulated. The AUTODYN calculations which were explained in section VB are already showing that the penetration itself will not result in strong target deformations⁵⁶; however the penetration was simulated in 3D additionally to validate these results.

1. Jet Data

To simulate the penetration the jet characteristics which occurred at the specific plates needed to be estimated. The main information here is the velocity and the actual radius. Additionally the length of the jet is important.

The information was gathered like explained in V2 by taking the average TOA for all water experiments as the basis for the further estimations.

The characteristics of the jet at the stand off distance are known from the simulation described in VB and validated as far as possible by the comparison with the experimental data.

Due to the elongation, which is caused by the mass gradient in the jet, the radius and length of the jet portions are changing during the travel into the target, while the velocity stays the same⁵⁷. Critical for the penetration behavior are the (i) velocity and (ii) the radius of the jet portion, while the length is only of interest as if it is enough to penetrate the entire plate. The jet length can be calculated using the known equation 12, assuming that the jet portion of interest must be able to penetrate plate and the liquid following, this being 3.277mm of steel and 22.9mm of water. Therefore the length is like in equation 25:

$$l_{jet} = 3.277mm \sqrt{\frac{\rho_{steel}}{\rho_{aluminum}}} + 22.9mm \sqrt{\frac{\rho_{water}}{\rho_{aluminum}}} \quad (25)$$

⁵⁶See also VIIC.

⁵⁷Until the portion reaches the erosion front.

which delivers $l_{jet} = 19.23\text{mm}$. This is a maximum limit which makes sure the jet penetrates.

During the travel into the target the velocity gradient in the jet leads to a elongation, which is responsible for the particulation. Additionally the radius decreases. Although the particulation effect is expected to be of more influence than the radius decrease, this decrease was estimated and included into the simulation. The minimum radius which is occurring due to elongation can be estimated by assuming that the volume of a jet portion stays the same, which dictates the relation between radius and length of the portion like in equation 26:

$$V_1 = V_2 \Rightarrow l_1 \pi r_1^2 = l_2 \pi r_2^2 \Rightarrow r_2 = r_1 \sqrt{\frac{l_1}{l_2}} \quad (26)$$

This adjustment was used in the simulations. Still it must be considered that this is a minimum estimation. However it shows good results.

2. Influence of the Slug

Like explained in IIA and II3 the liner material forms the fast traveling jet and the much slower slug.

Due to the relatively small thickness of the target plates the slug is able to penetrate some of them. During the test the slug was once found stuck in the 4th plate, and the deformation measurements show clear evidence that the slug penetrated and deformed some of the first plates in the targets in all tests.

To estimate the influence of the slug on the target deformation, it was included in the simulations of the first plates till it was to slow to be able to penetrate any more. Due to the velocity difference between the jet and the slug it is not reasonable to include both in the same calculation. Therefore the simulations needed to be divided.

This is a maximum estimation, because the possible influence of the water was not included. If there is water in the way of the slug or not is very difficult to say. During the

travel of the jet through the target the water is displaced and forms a tunnel⁵⁸. Figure 26 shows this channel during the mentioned coarse target simulation.

Due to the complexity of the target which makes it not feasible to simulate the entire process, and the impossibility to visualize the penetration without x-ray technology it is not known if the tunnel is stable long enough to let the slug travel without being influenced by water or not.

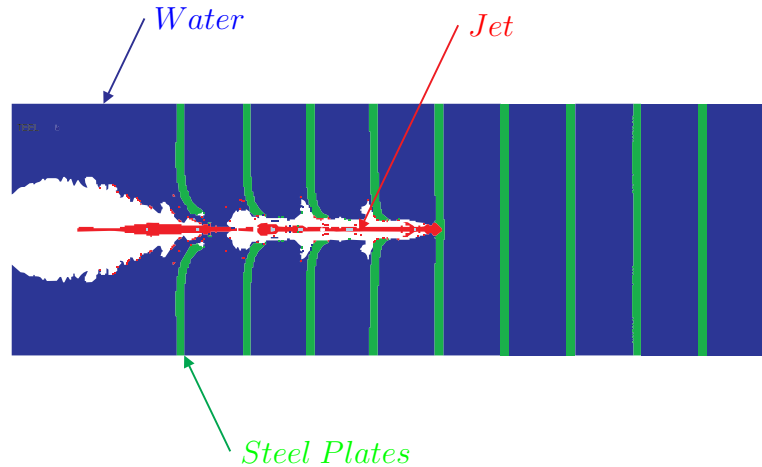


Figure 26: Picture of the penetration process of the steel plate target in a simulation. The tunnel formed by the water flowing away from the penetration axis is clearly visible.

Therefore the water was left away, and a simulation was done where the travel of the slug through the first three plates⁵⁹ was determined, the hole from the penetration of the jet included.

With the information of the maximum possible number of plates penetrated the slug was then included in the penetration simulations in WORKBENCH.

This information, combined with the fact that the slug was found to stuck in the fourth plate in one test, proves additionally that the strong deformation in the last plates can not be caused by kinetic influence of liner parts. Even if the slug would be able to penetrate twice as much distance it still would not influence the ninth and tenth plate, were the most deformation occurred.

⁵⁸A article that handles that topic is [C.C96].

⁵⁹Where it found to have stopped in the simulations

3. Geometric Setup of the WORKBENCH Penetration Simulations

The WORBENCH simulations contained the exact setup of the target plates, which are simple steel plates with holes in where the rods holding the stack together are put in.

The symmetries of the target plates were used to keep the problem small. The plate is symmetric in two planes, so only one quarter of the complete plate needs to be simulated, which means that much less cells need to be calculated.

Figure 27 shows the setup that was used. The green areas are the two symmetry planes which will complete the plate in the simulation.

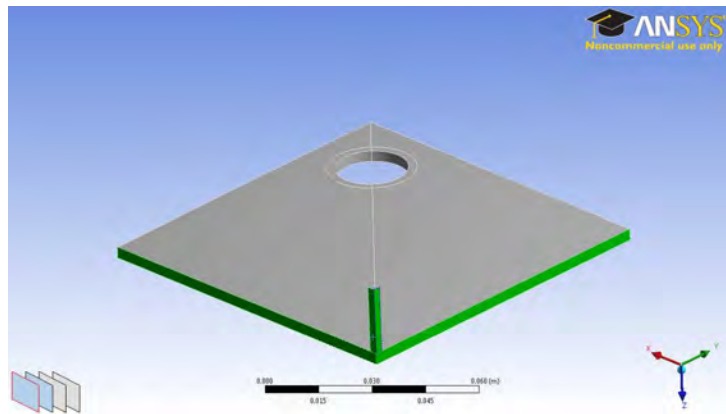


Figure 27: Plate for the WORKBENCH simulation. The green regions are the symmetry planes

The deformation is measured along the diagonal path like done in the experiments.

E. PLATE DEFORMATION SIMULATIONS IN ANSYS WORKBENCH 3D EXPLICIT DYNAMICS

The lack of chemistry in the ANSYS AUTODYN disallows the inclusion of hydro reactive effects.

To estimate the amount of energy which is released during the reaction WORKBENCH 3D EXPLICIT DYNAMICS simulations were used. The 3D feature also allows to recreate the influence of the non axial symmetric geometry of the plates.

To estimate the energy which is needed to deform the plate like observed, which is the plastic work done at the plate, the plate is loaded with a pressure that decreases over time. The pressure is varied until the final deformation matches the one observed in the experiments. This estimation will not include any of the energy needed for the fluid process that is occurring because water has to be displaced. However, it can provide basically a magnitude of the energy that is converted during the process, and is furthermore directly linked to the only measurable effect being the plastic deformation of the target plates.

Additionally, WORKBENCH provides the possibility to of parametric simulations, which means that the different initial parameters and the results can be calculated using one setup and one simulation.

1. Energy Source in the WORKBENCH Simulation

Due to the fact that only the plastic work is done at the plate prior to deformation, the energy source to reach this deformation can be chosen freely. This allows again to keep the simulation very simple, because no additional materials like air or water are needed, and the complete process contains only the plate.

The plate was therefore simply loaded with a pressure like shown in figure 29. As the area where the pressure is applied to a circle was created.

The plastic work dissipated in the plate depends only on the pressure and the resulting strain, not on the time magnitude of the process. This becomes obvious if the stress-strain diagram is reminded, like in figure 28. The shaded area A below the curve is

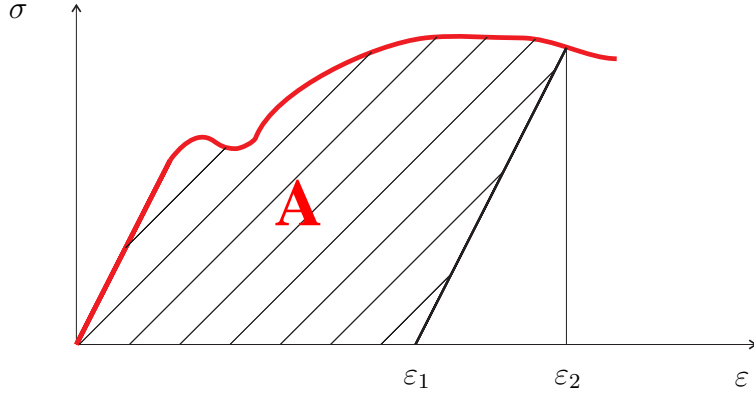


Figure 28: Stress-Strain Diagram. The shaded area A is a measure of the plastic work.

a direct measurement for the plastic work⁶⁰ done per volume unit of the metal⁶¹, assuming no initial stress:

$$w_{plastic} = \int_0^{\varepsilon_2} \delta(\varepsilon) d\varepsilon - \frac{1}{2} (\varepsilon_2 - \varepsilon_1) \delta(\varepsilon_2) \quad (28)$$

The integral calculates the complete area. Due to the elastic behavior of the material the final strain after the stress is relieved is below the maximum which was achieved under full pressure. Therefore the linear fraction must be considered by subtracting the corresponding part.

This shows that the amount of plastic work dissipated in a material behaving like that neither depends on how the deformation is produced nor the time passing during the process. As long as the final deformation is the same, the amount of energy is the same⁶².

⁶⁰There is additional elastic work, which is represented by the fact that the final strain is smaller than the observed highest strain if the stress is released in the end. In the simulation only the plastic work is measured. In the experiment there will be a small amount of elastic work be stored in the plate, which is due to the geometry and the resulting constraints. This amount is much smaller than the plastic work.

⁶¹The analysis of the units delivers:

$$[w] = [\delta \cdot \varepsilon] = \frac{N}{m^2} = \frac{J}{m^3} \quad (27)$$

⁶²Of course the elastic work can differ a lot. Also the process must not include re-plastification, meaning that the plate is plastic deformed beyond the wanted value and afterwards formed back again.

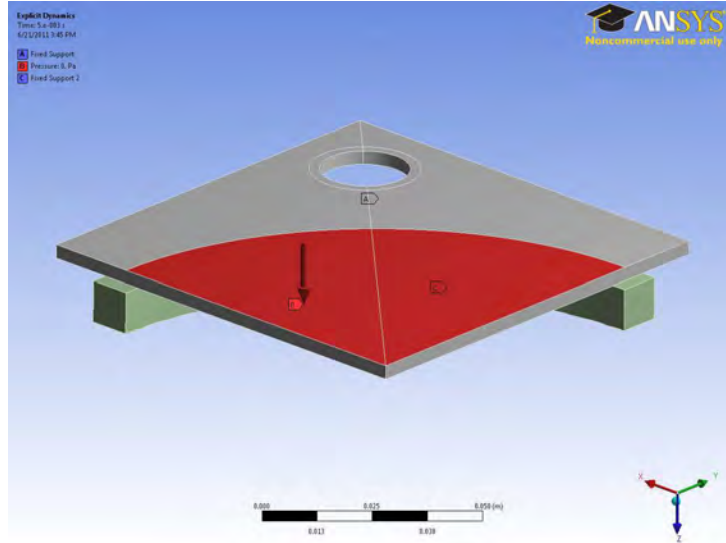


Figure 29: Plate for the WORKBENCH simulation. The red area shows the pressure load.

Therefore the pressure can vary over time in any particular way, as long as strong oscillations are avoided which could theoretically be caused by a sudden decrease or increase of pressure. These oscillations could lead to additional plastic work by bending the plate back and forth.

2. Geometric Setup of the WORKBENCH Deformation Simulations

The general setup of the plate is equal to the one from the penetration simulation, with an additional circle imprinted in the top face to define the area for the pressure load. Again the deformation is measured along the diagonal path. Figure 29 shows the plate.

The also visible ring below the plate was included to match the experimental results more closely, after the first simulations were evaluated.

3. Estimation of the Pressure Magnitude

The magnitude of pressure that causes plastic deformation in the target plates was estimated with a very simple back-of-the-envelope technique. The idea is to assume the plate being a beam like in figure 30, which will allow to calculate the stress occurring at the bottom of the plate using simple analytic equations. If the stress reaches the yield strength

of the plate material the lower pressure threshold is found. Pressures higher than that will cause plastic deformation.

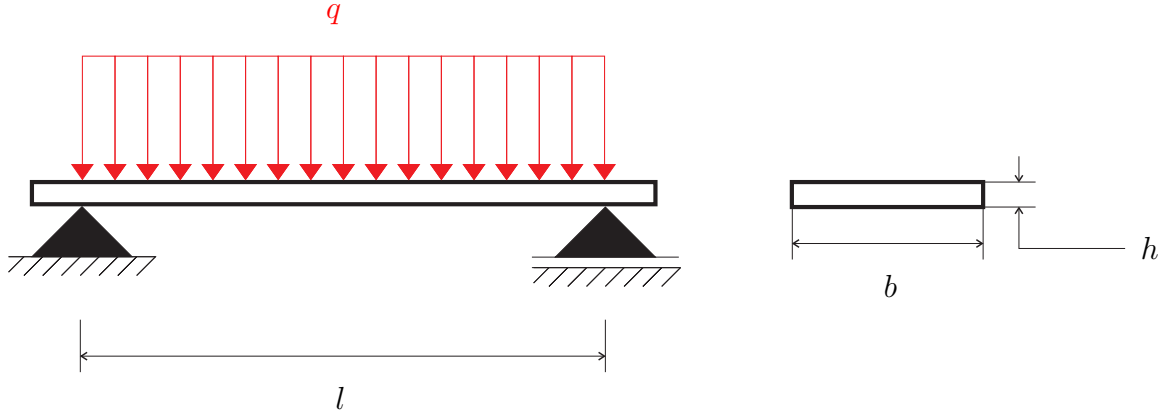


Figure 30: Sketch showing the values for the pressure magnitude estimation

In a setup like that the bending moment M_b in the beam is like in equation 29:

$$M_b = \frac{ql^2}{8} = \frac{pb l^2}{8} \quad (29)$$

The maximum stress is occurring at the bottom of the plate and can be calculated by

$$\sigma = \frac{M_b}{I_y} \cdot \frac{h}{2} \quad (30)$$

Combining the equations and knowing that $I_y = \frac{bh^3}{12}$ the pressure turns out to be

$$p = \frac{8M_b}{bl} = \frac{4}{3} \cdot \frac{h^2}{l^2} \cdot \sigma \quad (31)$$

Mason found the yield stress of the used target steel to be 327 MPa . The diagonal distance between the holes where the plates are held is approximately 200 mm , and the plate is 3.277 mm thick. The resulting threshold pressure is $p = 0.12 \text{ MPa}$.

This pressure is the lower limit where the bottom layer of the beam is exposed to the yield stress. To deform the beam plastically a higher pressure is needed.

The approach gives a very good idea of the threshold. The simulations were started using 1 MPa , which showed visible plastic deformation, and the range of 1 to 4 MPa which was simulated covers the full magnitude of the observed deformation.

F. DIVIDING PENETRATION AND COMBUSTION EFFECTS

From the initial experiments and considerations it is known that the deformation did not occur in the plates prior to 8 and 9 in the tests where the straightest jets were generated. To estimate the energy-release out of the combustion the deformation which is caused by the penetration itself must be known. Additionally the experimental results must be compared to determine the area of influence.

The deformation results of Test 12 (water) and 13 (oil), which were chosen because both showed very close jet performance and TOA data, was compared by plotting the z-displacement along the diagonal path. The figures for all plates can be found in appendix D.

The figures 58 and 61 are showing the comparison exemplarily for plates seven and ten. While there is a clear difference in the last one, there is almost no difference in the first. Following the complete penetration path the deformation was even bigger in the oil than in the water test, which is likely to be caused by a more stable slug.

The comparison shows that only the plates from number eight and up need to be simulated with the pressure load.

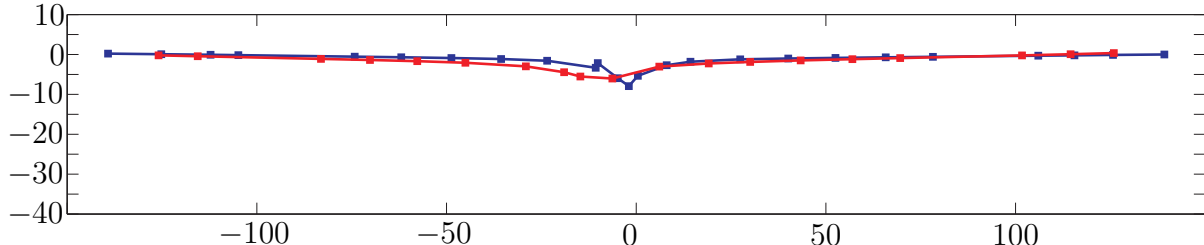


Figure 31: Plate 7 Difference in deformation of Test 12 (water,red) and Test 13 (oil,blue)

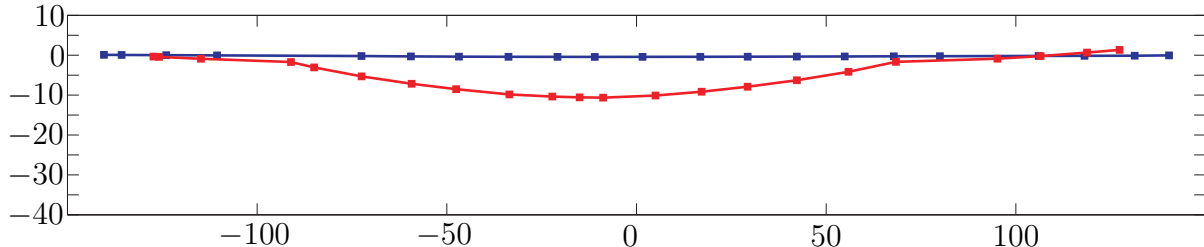


Figure 32: Plate 10 Difference in deformation of Test 12 (water,red) and Test 13 (oil,blue)

G. DATA ACQUISITION IN THE WORKBENCH SIMULATIONS

The deformation data of the target plates in the experiments were measured along the diagonal path. To be able to compare the experimental with the simulation data the z-deformation coordinates along this diagonal path were measured using the construction geometry feature in WORKBENCH, following the created edge in the diagonal described before.

This tool allows to evaluate the directional deformation along any path in the evaluated body.

The gathered data was then compared with the known deformations from the experiments using MATLAB plots.

H. ADDITIONAL EXPERIMENTS

During the work on this thesis the author had the possibility to participate in more experiments, which were also performed at the UIUC. These experiments were repetitions of the last experiments from Masons work, and additional tests to be able to concentrate on the properties of the process especially in the last plates, where the strong deformation occurred. An overview of all preliminary and recent experiments is provided in appendix C.

1. Repeating Tests

The data from the previous experiments did not contain TOA for all plates. In Test 11 and 12 only plates one to five were measured. Complete data was only available for Test 13.

Additionally it was uncertain when the deformation took place. This information could provide additional insight in the process.

To measure the deformation time an approach was tested where the plates were illuminated using blue LED's and filming the process with a high speed camera through a blue filter. The idea was to use the fact that the combustion produces light emissions with the maximum in the higher wavelength red areas of the visible light spectrum. So illuminating it with a light of shorter wavelength and filtering the light emitted by the target, which would be a mixture of emission from the combustion and the illumination, using a high pass filter could cut out the reaction and leaving only the wanted wavelengths.

Unfortunately the light emission from the combustion was way to intense, and the emission in the blue spectrum was pretty high.

Another approach using a flash which was triggered $0.5ms$ after the ignition, when the penetration process was almost over was also not satisfying because the shock wave caused cavitations and turbulent water that in addition with the debris made it impossible to film through the liquid.

2. Filter Tests

Out of the review of the previous work it was decided to develop a filter test, where the first steel plate and water combinations should be replaced by one solid steel plate, like shown in figure 33. This would allow to concentrate on the area where the strongest reaction was observed, guaranteeing that possible other influence than the jet itself would be filtered by the steel block.

The dimensions for the block based on simple penetration calculations using the known penetration law, backed up by simulations.

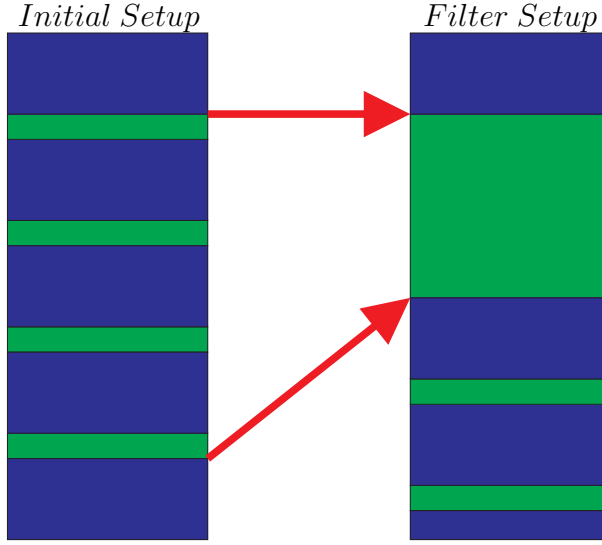


Figure 33: Principle of the filter tests, where one monolytic steel plate substitutes the first water/plate combinations.

In the preliminary experiments the jet penetrated plate nine. This distance, consisting of 29.5mm of steel and 246.7mm of water in total was used to estimate the jet length, like in formula 32:

$$l_{jet} = \sum l_{steel} + \sum l_{water} = \sum P_{steel} \sqrt{\frac{\rho_{steel}}{\rho_{aluminum}}} + \sum P_{water} \sqrt{\frac{\rho_{water}}{\rho_{aluminum}}} \quad (32)$$

which results in a total jet length of approximately 200mm⁶³. Using the penetration law again, the jet would be able to penetrate 120mm of steel.

It must be considered when using this estimation that the basic assumption for the approach above is the exceeding of any material strength by the high pressures occurring, or $\frac{1}{2}\rho_{jet}u^2 \gg \sigma_{jet}$ or σ_{target} , which leads to the observed behavior.

However, this assumptions is, like explained before, only correct in high velocity processes beyond $3\frac{km}{s}$. In the later parts the jet velocity falls below this velocity. The behavior of the jet will therefore be influenced by its material strength again, while water,

⁶³Compare with [Mas10] p. 107

of course, still behaves like a liquid. The jet is able to penetrate water at low velocities where it would stop to penetrate steel by far.

Additionally the jet performance varies between the test, due to the many possible influences. Therefore it was decided to substitute the first seven plate/water combinations, and to keep the rest of the stack as usual. Replacing seven plates and the matching distance of water with steel would result in a steel plate with a total thickness of 94mm. Due to the available dimensions of material the decision fell on using a 2in and a 1.5in plate, which equals 88.9mm. The missing distance was substituted by additional 15.5mm of water above the plate.

This setup was verified in a simulation. The breakthrough velocity was found to be approximately $3\frac{km}{s}$, with a possible breakthrough mass of approximately 2.5g.

THIS PAGE INTENTIONALLY LEFT BLANK

VI. EXPERIMENTAL RESULTS

Several experiments were conducted in previous works and during this research. This chapter displays the different results and summarizes them. An overview of all preliminary and recent experiments is provided in appendix C.

A. EVALUATION OF THE TOA DATA FROM THE PRELIMINARY EXPERIMENTS IN TERMS OF CHEMICAL EROSION

Different approaches were tested to find indications for an increased erosion due to the chemical reaction during the penetration process.

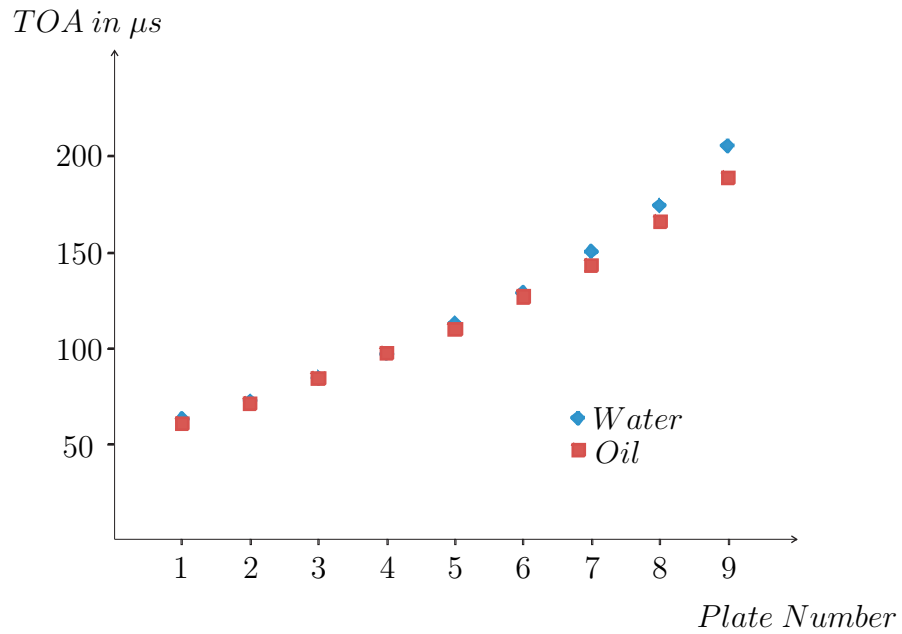


Figure 34: Average TOA from the all water tests and TOA from the oil test for the different plates

The average TOA data for all plates and the TOA of the oil experiment is plotted in figure 34.

The oil TOA, especially in the later plates, is earlier than in the water tests. The mean difference over all plates is 2.9%, while in plates 7,8 and 9 it is 4.77%, 4.72% and 7.94%.

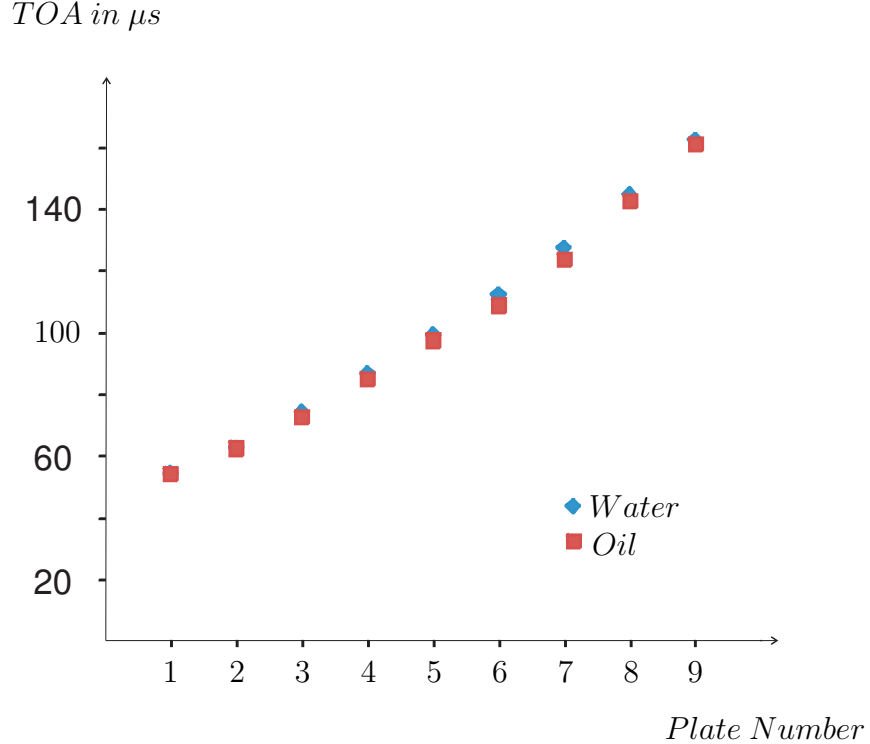


Figure 35: TOA for the oil and the water AUTODYN simulation over the plates

Between the water and oil simulation, which TOA can be seen in 35, the mean difference is only 1.86%, with the maximum being 3.64%. This indicates that the difference observed in the experiments is not explainable by the density difference alone.

However, any statement out of this data is vague. There is only one oil test, and TOA data for all plates is only available for two water tests. Therefore the result is that there might be indications of stronger erosion due to the chemical reaction, but to be able to make a adequate proven statement on this effect the amount of data is not sufficient.

Still, this concerns only the question if there is additional erosion due to the chemical reaction or not. The main parameter of the erosion process are still the ones known from usual shaped charge processes. It is likely that the influence of the reaction is rela-

tively small. The process can not start before the particle is in contact with water, which happens directly at the erosion front or after the particle is already eroded. Especially in the first plates the jet is way to fast to allow to be influenced by the reaction.

B. REPEATING TESTS

There where two main goals for the repeated tests, firstly to validate the known results and secondly to try to gather information about when the deformation of the plates occurred. Additionally the TOA was gathered for all plates, this providing more possibilities to compare the experiments with the simulations.

The repeating tests where number 1, 2 and 4. In all tests water was used as liquid, with all dimensions being the same as in the initial experiments⁶⁴.

The results from Masons work where confirmed. In all test similar deformations where observed, with the penetration stopping between the eighth and the tenth plate. Also the TOA data was similar to the initially measured⁶⁵.

The complete TOA data can be found in tables 6 to 9 in Appendix E.

1. Test 1

In test one the jet penetrated plate eight, stopping in plate nine. Very strong deformation occurred in the ninth plate.

Due to trigger problems the camera started to record after the actual event. The jet penetrated up to plate nine, deformed it but could not penetrate it.

Strong deformation was observed in plate eight and nine.

2. Test 2

In test two the camera was able to capture the penetration process.

No deformation was observed before the pressure wave hit the window. Observation was impossible after that.

⁶⁴All dimensions are provided in appendix B, and the assembly in A

⁶⁵Compare also VA2.

The jet penetrated plate seven and struck plate eight not penetrating it. Strong deformation of plate eight occurred again.

The slug was found in this test, it stuck in plate number four.

3. Test 4

Test four was the test with the best jet performance in this experiment series. The jet penetrated plate 9 and struck plate 10 almost penetrating it. Strong deformation occurred in plate nine and ten.

Due to problems with the measurement equipment no TOA data was gathered for plate one, two and three.

C. FILTER TESTS

The intention of the filter tests was to be able to concentrate on the processes which were caused by the jet only by excluding any other parts like the slug or influences like the explosion gases on the penetration of the last plates.

It was shown that the very impressive deformation effect occurred similar to the already known tests, and in the same parts of the target.

1. Test 3

Test three used the dimensions explained above. Unfortunately the jet did not penetrate the total distance, stopping right before the breakthrough.

If compared with the test number two, where the jet only penetrated plate eight, and keeping in mind the influence explained above, possible imperfections could be the reason.

2. Test 5

To avoid the possibility of not penetrating the total distance only a *2inch* or *50.8mm* steel plate was used in this tests, with the same stand off distance of water above it as in the usual stack tests (*63.5mm*). In this combination it substitutes the first five plates.

The jet penetrated the plate and stopped after the following fourth plate. This equals a total penetration of approximately nine plates, showing the correctness of the assumptions and the ability to repeat the experiment with the same results.

The last plate was heavily deformed.

Due to problems with the measurement equipment no TOA data was gathered for the beginning and end of the filter plate and the first plate following.

3. Comparison of the Penetration Performance in the Filter Test with the Plate Array Tests

In test 5 the jet penetrated the filter plate and plate 4, stopping between 4 and 5 and causing heavy deformation.

To be able to compare this penetration performance with the usual setup, the matching theoretical jet length must be calculated using the well known penetration law⁶⁶.

The jet penetrated the initial water stand off and three spaces, adding to a total distance of $63.5mm + 3 \cdot 22.9mm = 132mm$ of water. The total distance of steel was $50.8mm$ for the filter plate and $4 \cdot 3.3mm$ for the other plates, thus adding up to $63.908mm$ of steel. This leads to a theoretical jet length of approximately $187mm$.

The penetration of plate 8 equals a theoretical length of $178mm$, while the penetration of plate 9 equals $197mm$. This leads to the conclusion that, if compared with the usual setup, the jet from the filter test penetrated plate 8 and maybe hit plate 9. The penetration result is therefore close to Test 11 preliminary and Test 1 from the recent experiments.

Figure 36 shows the comparison of the calculated theoretical jet length from the filter experiments (in blue) and the theoretical jet lengths of the other experiments (in red).

Of course it is quite difficult to compare the tests due to the different dimensions. The filter plate does not exactly substitute parts of the filter; the exact plate number would be 5.15 plates. Additionally it is not known where the penetration exactly stopped, because the point can not be measured in water. Also the penetration behavior in the solid steel and the water/steel mixture differs. Still the comparison shows that the test works good, and

⁶⁶Compare with section VH2, equation 32.

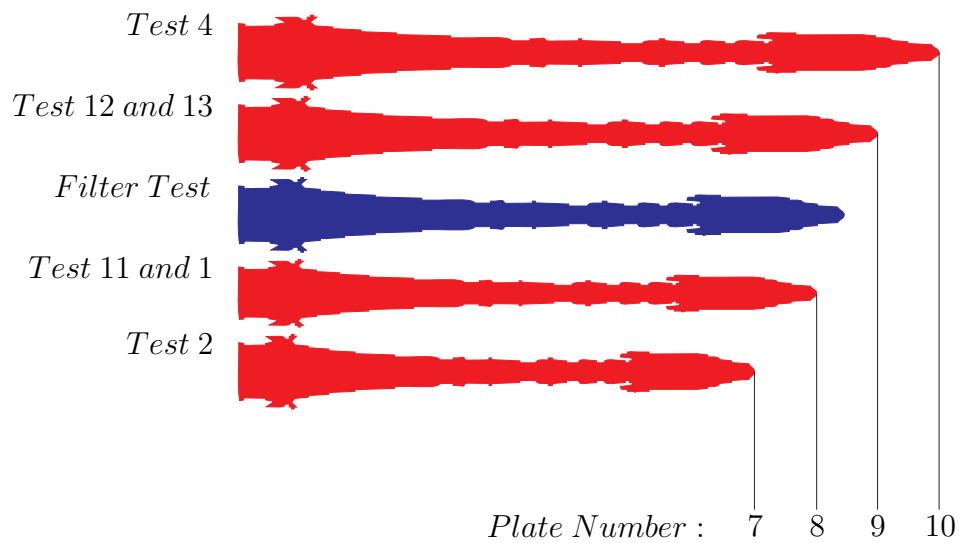


Figure 36: Comparison of the theoretical jet length calculated from the penetration performance for the filter test (blue) and the other experiments (red).

validated the deformation results from the initially experiments by filtering out any possible other influence than the combustion.

VII. SIMULATIONS AND EXAMINATION OF EXPERIMENTAL RESULTS

A. COMPARISON OF THE SIMULATIONS AND THE EXPERIMENTAL RESULTS

To validate the simulation results they had to be compared with those from the experiments.

The data which can be compared are the TOA of the jet at the different target plates, the total penetration depth and the hole sizes. Additionally the jet tip velocity was measured in tests 11,12 and 13 by Mason.

Basis for all simulations was a simulated charge following the experimental properties, with the calculation stopped as the jet tip reached the stand off distance.

1. Jet tip velocity

The jet tip velocity was measured by Mason, using a laser system. Basically a laser beam was split and sent on two photo diodes. When the jet traveled through the beam, the intensity drop was measured and the velocity was calculated.

Mason measured velocities of 6.18, 6.43 and $7.04 \frac{km}{s}$ in test 11,12 and 13. While the method worked very well in the two first test, the intensity drop was quite diffuse in the last test, which was the cause of the calculated very high tip velocity. The reason for that stayed unknown. The result is considered strongly distorted, because the value is unrealistic high.

The tip velocity in the AUTODYN simulations was $6.16 \frac{m}{s}$, which is a difference to the average value from the experiments not including the last value, $6.3 \frac{km}{s}$, of 2.3%.

This difference is very small if compared with the uncertainties in the assembling of the shaped charge and the possible errors in the measurement and the limits of the computation.

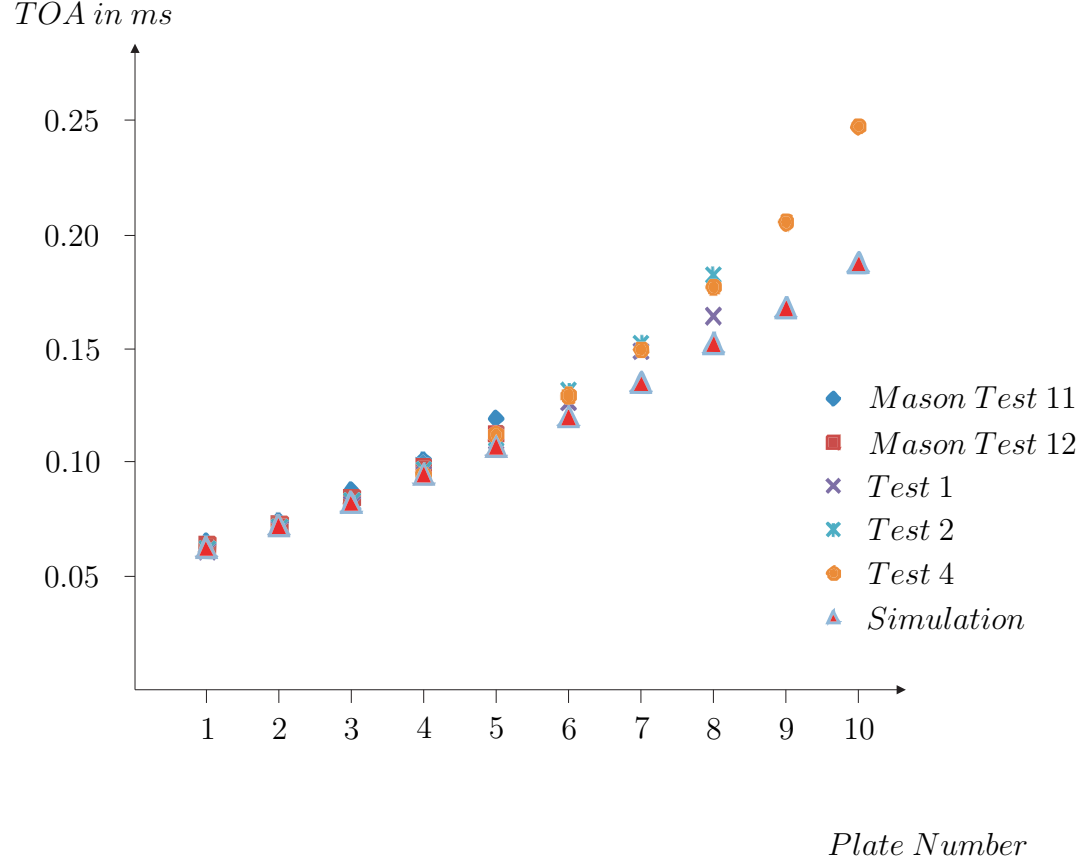


Figure 37: Comparison of the TOA from the experiments with water as submerging fluid and the matching simulation⁶⁷.

2. TOA

Figure 37 provides the TOA data from the different experiments and the simulation⁶⁷.

The TOA data was triggered with the ignition of the explosive. Therefore the data includes not only the time which was needed to form the jet and allowing it to travel up to the first plate, but additionally the delay of the detonator. This detonator was not simulated,

⁶⁷The complete TOA data for all tests involving the plate array can be found in appendix F in table 10 of the penetration through the water submerged targets. The data includes the previous experiments displayed in IID as well as those from additional experiments, which are discussed in VI.

and therefore the simulated jet reached the first plate slightly earlier than the ones in the experiments⁶⁸.

Additionally the time between the initiation and the impact at the first plate is influenced by the detonator, too. Therefore the only way to truly compare TOA data is to adjust it to the time of impact at the first plate. This adjustment is included in figure 37.

The difference between the simulation and the experiments is reasonable small, especially in the first plates. Along the penetration path this difference is increasing, which could be a hint for the increasing influence of the reaction on the erosion⁶⁹.

3. Penetration Depth

In the water experiments the jet penetrated plate 9 in test 12 and 13⁷⁰, and clearly hit plate 10 in test 4 but did not penetrate through. In tests 11, 1 and 2 it reached plate 7, 8 and 7. In the simulation the jet was able to penetrate much further, up to plate 15 which equals an increase of more than 50% if compared with the deepest experimental penetration. It is important to note that penetration cutoff criteria, usually invoked in these type of estimates was not employed because of the nature of the target. This is most likely the cause of this difference between simulation and experiment along with the fact that the simulation treats the charge as a perfect assembly without grain boundaries leading to a perfectly aligned jet.

This is believed to be caused by the fact that in the simulation the jet is perfect aligned along the axis of symmetry eliminating any chance of multiple impacts against the plates. In the reality this is not the case; the jet parts tumble and drift off-axis during the process. This becomes more obvious when the hole diameters are compared, as done in the following section.

Like discussed in I4 and 1 the jet forming process is very vulnerable for disturbance like asymmetries. It is very difficult to maintain exact specifications.

⁶⁸The average TOA at the first plate of the experiments was 62.4s, and the jet reached that plate after 53.2s in the simulation, which is a difference of 14.7%.

⁶⁹It is difficult to find one reason due to the many possible influences. Still, the simulation is of a absolute perfect charge, which will never be the case in reality. The mentioned reason, however, matches further results.

⁷⁰It was not sure if the jet reached plate 10 in test 13.

4. Hole Diameter

Hole Diameter in mm

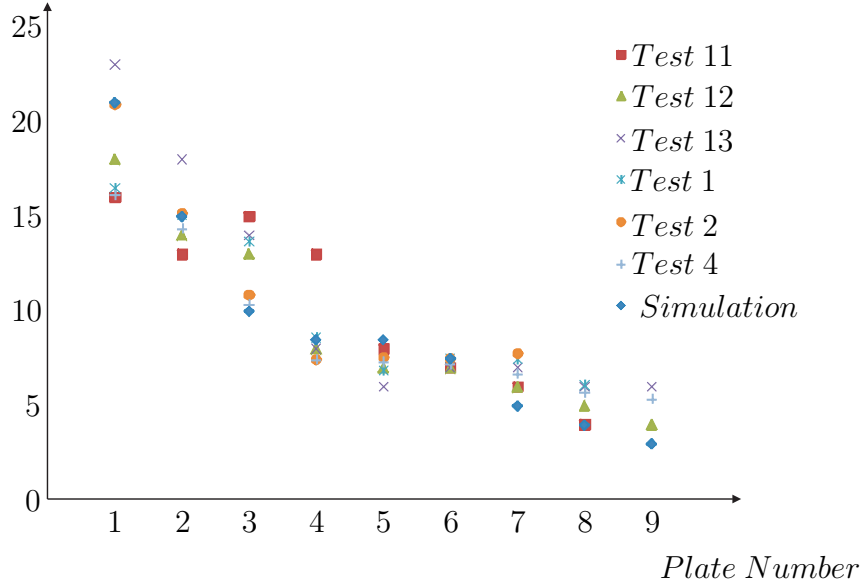


Figure 38: Comparison of the hole diameters in the plates from the water experiments and the matching simulation

Figure 38 displays the hole diameters of the simulation and the experiments. The simulation gave smaller diameters; the average difference is 31.5%. This is strong evidence for the fact that the real jet was not as perfect as the simulated one⁷¹.

Hole diameter differences between tests are a reflection of charge variations. The differences between average hole diameters (shown in Figure 39) and the simulation result from the noted charge perfection implicitly assumed in the simulation and actual conditions, which lead to larger holes because of jet turning and multiple impacts, a greater rate of jet expenditure and finally less penetration than predicted.

⁷¹The hole diameters for the first three plates are a combination of two simulations, one containing only the jet, the other only the slug. The influence of the slug and general related issues are discussed in VD2

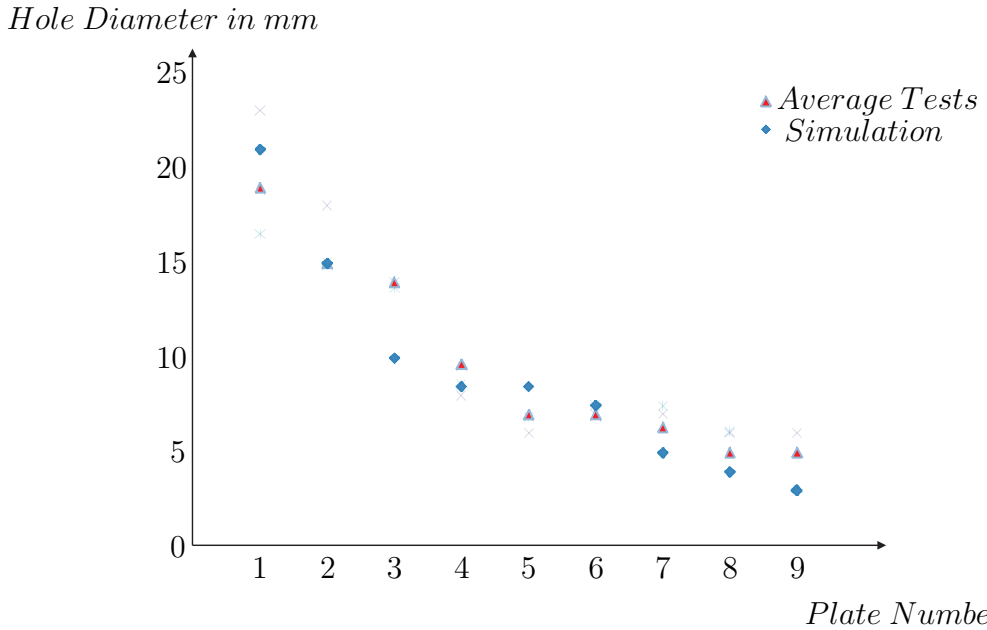


Figure 39: Comparison of the average hole diameters in the plates from the water experiments and the matching simulation

B. MASS DISTRIBUTION AND POTENTIAL CHEMICAL ENERGY IN THE TARGET

An objective of this research is to identify and -if possible - quantify the source(s) of energy responsible for the observed deformations of the water submerged plates. The almost identical penetration rates and depth reached by the jet in oil and water and the differences in resultant deformation suggests that reactions of the aluminum liner with the water and those leading to voluminous gas release must be responsible. The similarities in the penetration of the spaced targets in the two fluids suggest that deposits of jet mass between plates are close to the same. The large deformation at penetration termination might be caused by the reaction of the relatively large mass in the jet tail that travels to slow to penetrate further. It is important to note that jet mass increases along the jet length, thus there is also a large amount of mass along the slow portion of the jet stream.

The following analyses outline the methodology for tracking jet through the target and estimating the quantity between the final plates. The different approaches are narrow-

ing down the magnitude of the available reactive mass for the combustion, which gives a range of the possible release of chemical energy. All mass distribution data can be found in appendix H.

1. Mass Distribution Estimation from AUTODYN Penetration Simulations

In the target simulations the estimation delivers a upper and a lower limit of the mass which is distributed between the plates in a water simulation. The lower limit is the value for the case that the jet is penetrating much further than observed in the experiments, so that only the mass eroded by the usual effects is distributed. Figure 40 displays results, leaving out the mass which is distributed before the first plate ($3g$).

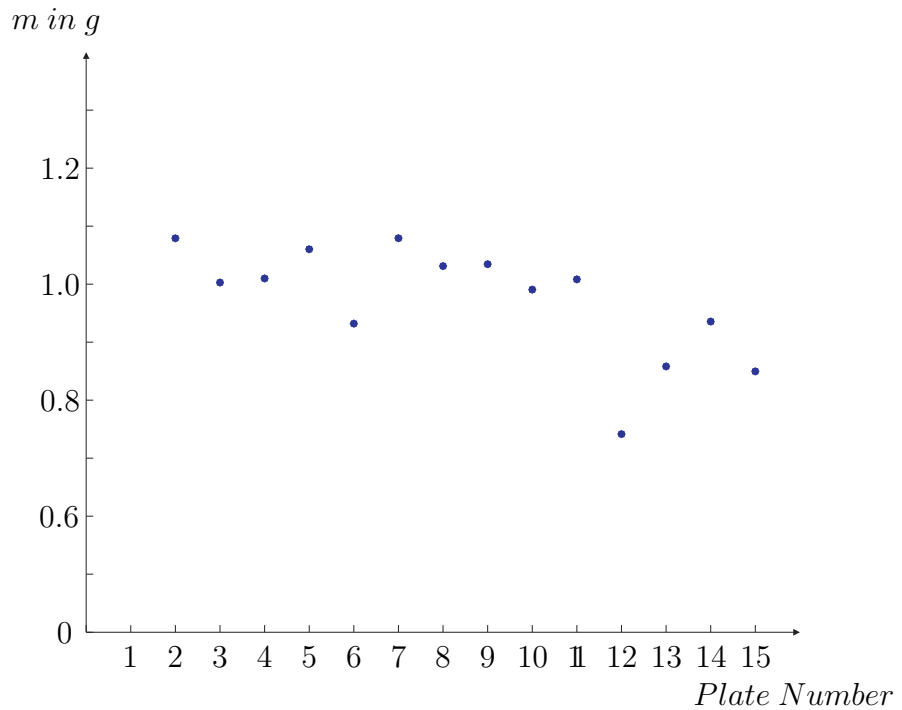


Figure 40: Minimum mass distribution in the water simulation. The mass distributed before the first plate is not included.

The distributed mass is relatively stable; the amount which is eroded between plate 9 and 10 is $0.29g$ which has a chemical energy of $4.123kJ$.

Assuming that the penetration stops at this plate and the complete jet portion which is traveling further in the simulation is available for the combustion at that very place, there would be $1.49g$ of aluminum or $22.976kJ$ potential chemical energy, respectively.

In summary, this result of this approach is that the mass distributed between the ninth and tenth plate is in the magnitude of 0.3 to 1.5 grams, with a possible chemical energy release between 4.2 and $23kJ$.

An additional simulation was done using oil. The mass distribution data differs very little from the water simulation, and can also be found in the appendix.

2. Mass Distribution Estimation from TOA and Cumulative Mass Data

Due to the fact that the jet performance was changing in the experiments, which is usual, the available information changes, too.

The experiments which are analyzed here were those with the best jet performance in terms of penetration depth, Test 12 and Test 13 from Masons Test and Test 4 from the recent experiments described in VH. The data for all tests can be found in appendix E.

TOA data were not available for all experiments, especially data for the last plates. This fact narrows the number of tests which are matching for the approach down to Test 13 and Test 4. Test 13 was the only test which was done in Oil; however it can be used because besides from the additional erosion, which is small, the data is absolute comparable with the water test, and the penetration performance in Test 4 was even better.

Figure 18 shows the distribution data for Test 13.

The most mass is distributed before the first plate. In this portion of the target, which is $63.5mm$ of water, the heavy tip of the jet is eroded. Although this implies strong possible deformation due to the high amount of chemical energy, there is no measurable effect because (i) the slug is hitting the first plates too⁷² and (ii) the first plate is not or not much shielded from the explosion gases.

⁷²See also section V D2

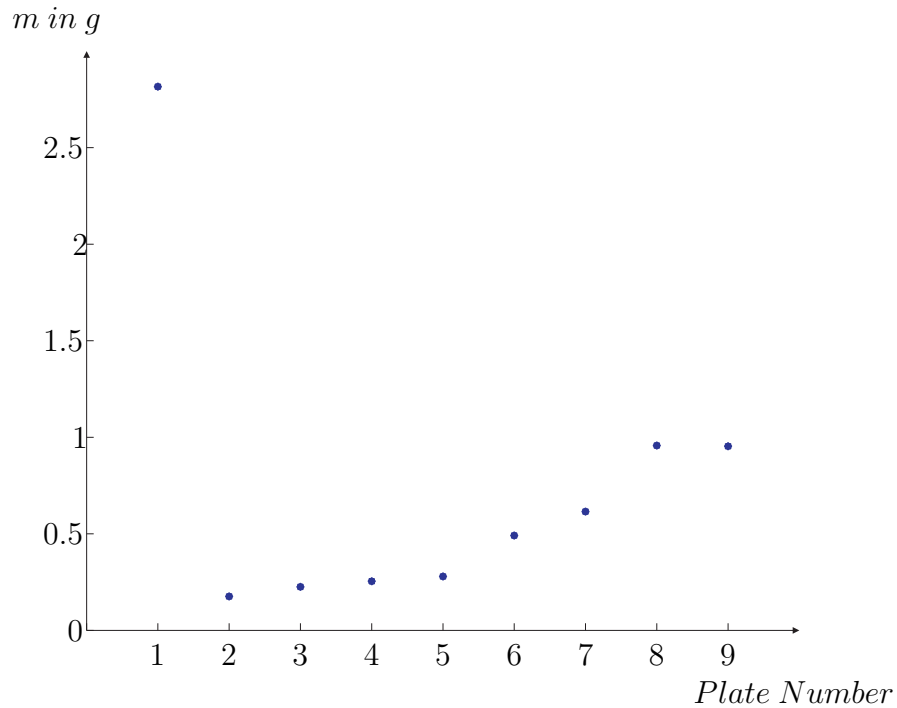


Figure 41: Mass distribution between the target plates of Test 13

Along the penetration path it is noticeable that the mass distribution increases up to the maximum of $0.9g$ of aluminum.

In figure 21 the same data is shown for Test 4, which was the one were the jet penetrated the longest distance. Unfortunately the measuring instrument for the first three plates failed in the test. Still the remaining data is very good.

The mass that is distributed between the ninth and tenth plate is $1.423g$, which is right below the maximum estimation from the simulation results.

All results from the TOA data estimations show the clear trend already found before: due to the increase of radius and the resulting increase of jet mass in the later parts of the jet the distributed mass is also increasing.

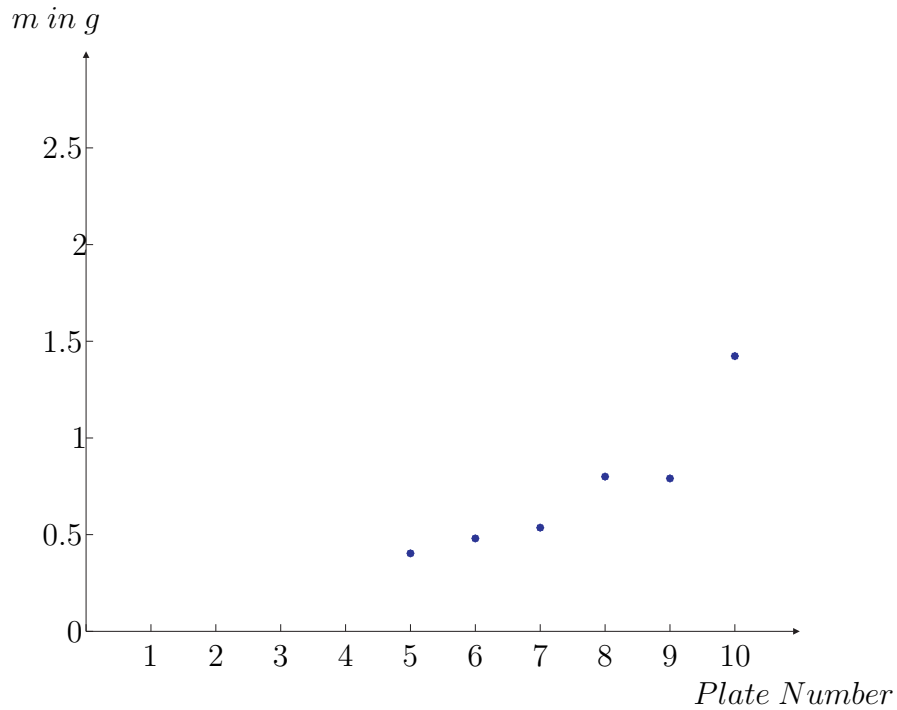


Figure 42: Mass distribution between the target plates of Test 4

C. TARGET PLATE DEFORMATION DUE TO PENETRATION

The plate deformation was estimated using ANSYS WORKBENCH EXPLICIT DYNAMICS 3D simulations, where a part of the jet and the slug were released against the plate. The complete results can be found in appendix I. In the following sections the first and the ninth plate, the last one completely penetrated in the tests, are shown in detail.

Figures 63 and 44 are showing the deformation in the z-direction along the diagonal path of the plate. The red graph shows the experimental data while the blue one shows the simulation results.

In the first plate the strong influence of the slug becomes noticeable, if the deformation is compared with the one that would be caused by the jet only, like in figure 45. In the simulation with the jet alone the plate stays mostly in its initial shape, with a relatively small hole where the jet penetrated it. This is typical for penetrations involving such very

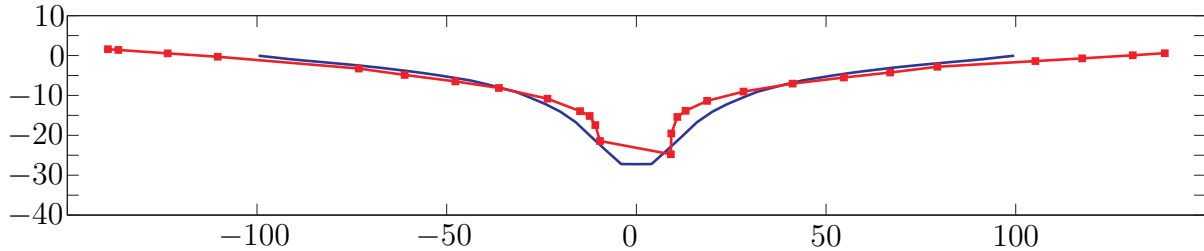


Figure 43: Plate 1 Penetration Simulation

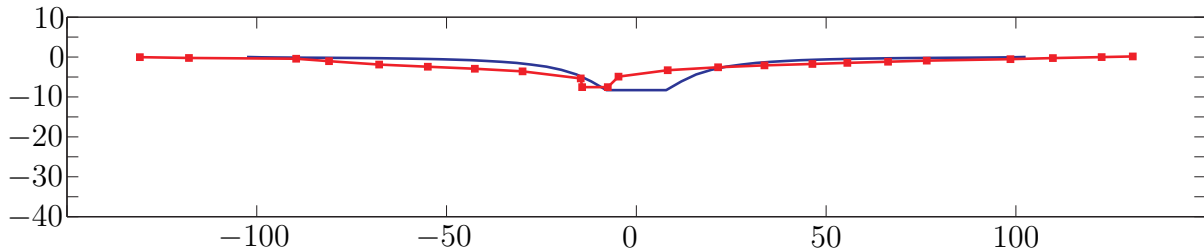


Figure 44: Plate 9 Penetration Simulation

high velocities (more than $4000 \frac{m}{s}$ of this jet parts). The much slower but heavier slug leads to a strong deformation of the plate and, additionally, a bigger hole.

The slug was able to penetrate plates one and two till it stopped in plate three⁷³, deforming it remarkably. In Test 13 it seems that at least parts of the slug reached beyond plate three, which would explain the differences of the results in plate four.

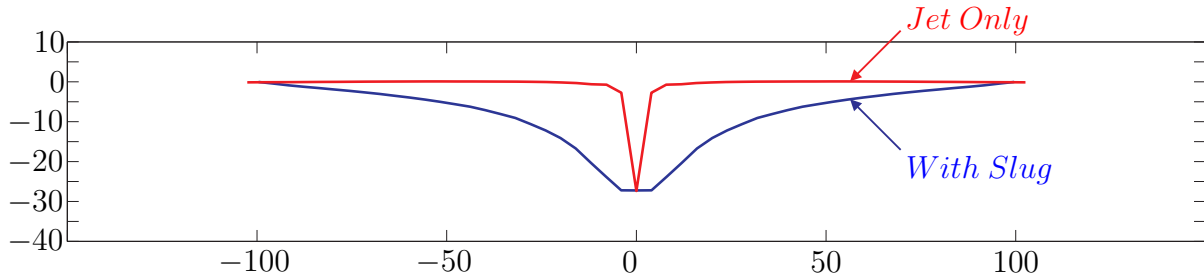


Figure 45: Comparison of Plate one deformation due to jet and slug penetration in the simulation.

In the ninth plate an offset between the holes can be observed. This is a hint for jet imperfection, because the jet does not travel on a centric path. This eccentricity will

⁷³In Test 2 it stuck in plate four.

decrease the ability to penetrate, which would explain the difference between the observed and the simulated penetration performance.

In all cases the matching between the experiments and the simulations was relatively good. Noticeable differences are mostly due to asymmetries, where the plates were deformed different on both sides of the hole. Due to the perfect symmetric character of the simulations something like that could not be observed.

Additionally, the discussed influence of the slug becomes very obvious. Even though it is relatively slow when compared with the jet, it still contains remarkable kinetic energy due to its mass.

Still, the deformation of the last plates cannot be explained by kinetic energy, because the slug would not be able to penetrate that far.

D. TARGET PLATE DEFORMATION DUE TO PRESSURE LOAD

Initially the plate was deformed just by applying a pressure. It was noticed that the deformation was differing in its type from the one observed in the experiments, like in figure 46.

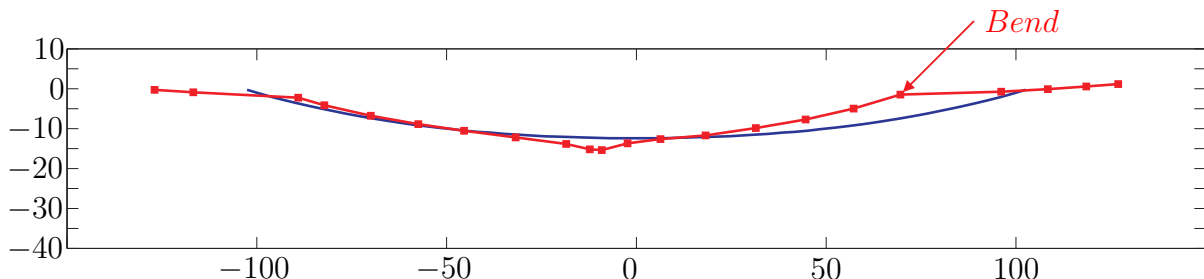


Figure 46: Comparison of the diagonal plate deformation due to pressure load in the simulation (blue) and the water experiments (red). The red arrow points at the differing bend.

Therefore the ring described in VE2 was included, which gave much better matching. It stops the deformation of parts of the plate at the value which was observed in the experiments.

The initial chosen pressure was 1 MPa and was increased up to 4 MPa . Then the deformation was compared with the data from the experiment, like in figure 48, where the blue line shows the simulation while the red one shows the experimental results. Figure 47 shows the total deformation of the target plate in the WORKBENCH simulation for a pressure load of 4 MPa .

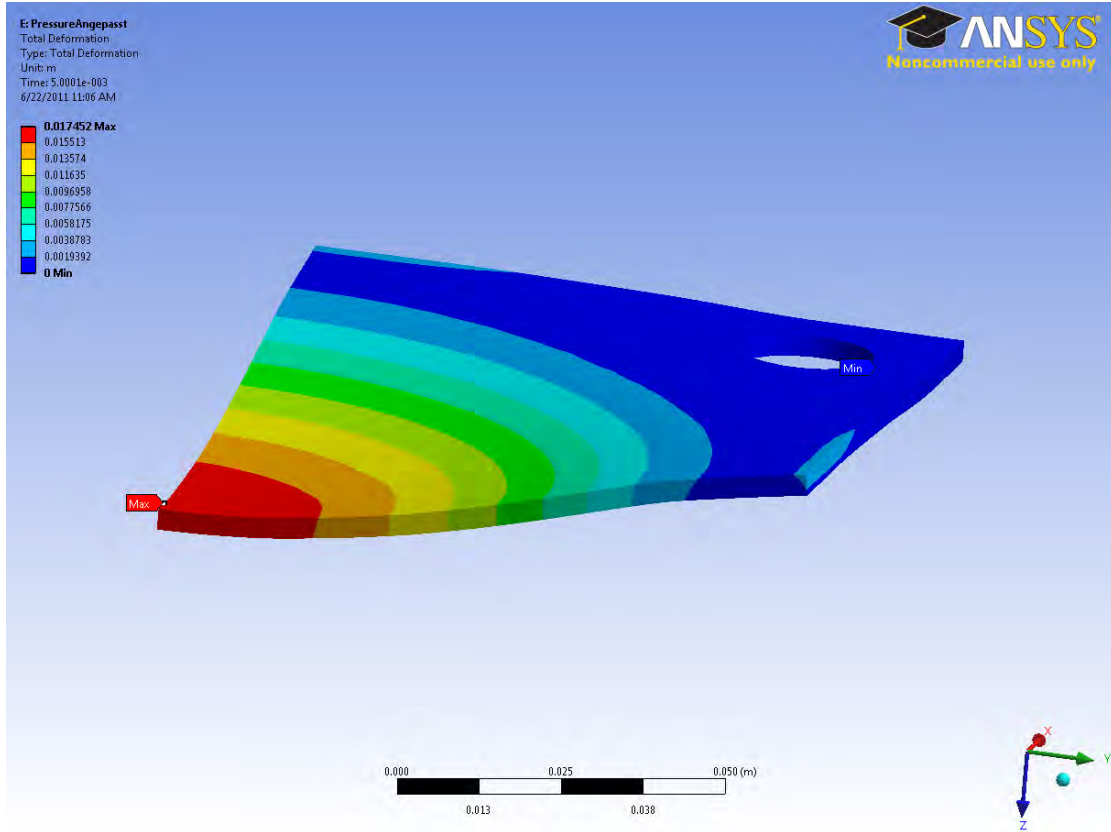


Figure 47: Example plate deformation in the ANSYS WORKBENCH pressure load simulation

The matching turns out to be very impressive. Additionally the decision of determining the deformation due to pressure only for the plates after number eight was justified.

The deformation in plates eight, nine and ten was reached by applying 1.25, 3 and 2.5 MPa of pressure. The work which was dissipated in these plates was 70.8, 343.2 and 247.588 J .

Plate 8

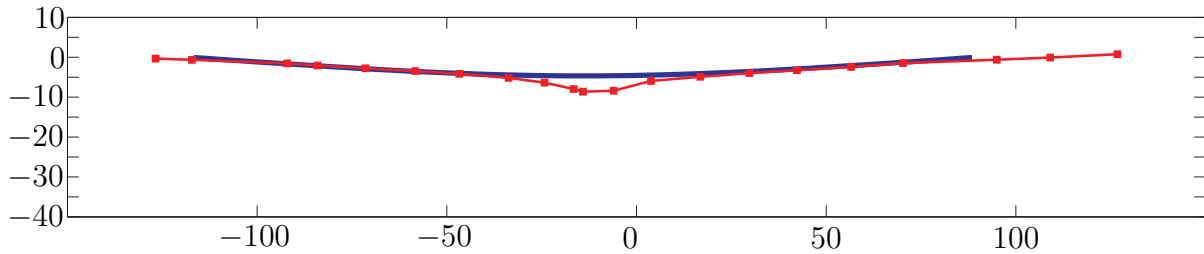


Plate 9

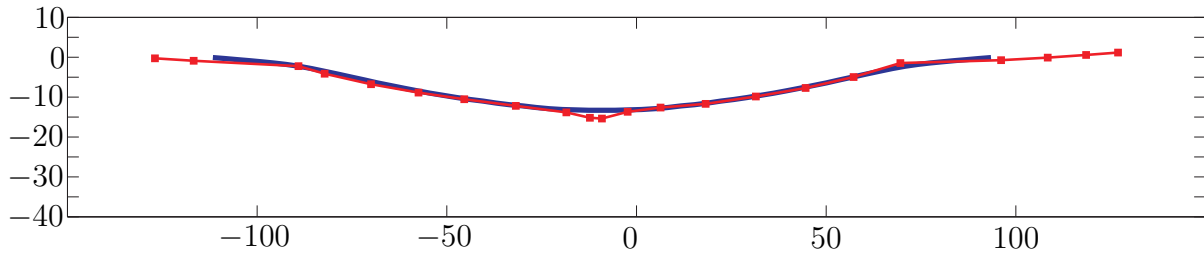


Plate 10

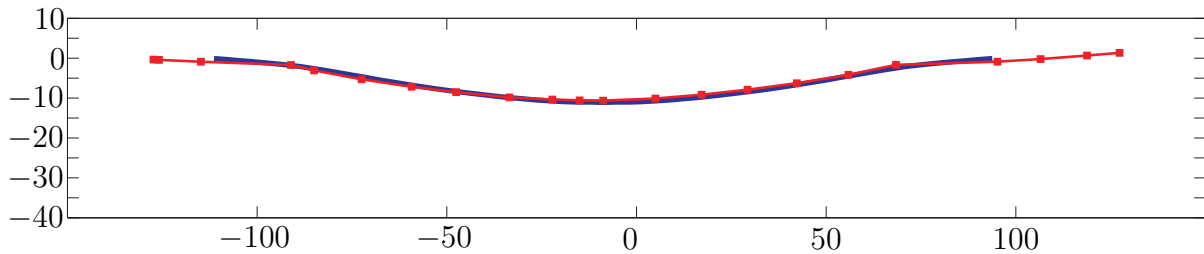


Figure 48: Plate8 to Plate 10 diagonal deformation from the WORKBENCH simulation in blue and Test 12 in red

E. ANALYSIS OF THE AVAILABLE MASS AND DEFORMATION RATIO

The amount of mass which is distributed between plate nine and ten is in the area of 1 to $1.5g$, which equals a potential chemical energy of 15.4 to $23kJ$ if calculated by the approach using the TOA data. The AUTODYN simulation also predicted the maximum of the available mass to be $1.5g$, and a minimum of $0.29g$.

The plastic work which is dissipated in the plates is in the magnitude of ca. 0.25 to $0.35kJ$, or 1 to 2.3%.

This ratio seems to be quite reasonable. The complete system is a thermodynamic process. To give a basic idea of the energy ratios in combustion and explosion processes one could think of the firing of a gun, like a howitzer. In such a weapon roughly 20 to 30%

of the chemical energy of the propellant are dissipated into kinetic energy of the projectile, while most of it is lost entropy. The same applies to engines, and of course explosives⁷⁴.

Furthermore, the values represent only the final plastic work. There is a lot more work done in the target during the displacement of the water.

Taking this into account, the ratio seems quite reasonable and should be expected dealing with effects like this.

⁷⁴Tests which try to measure the strength of an explosive are always fairly qualitative. Some are explained in [Hom02] and include the "Jumping Mortar Test" and "The Crater Method", which compare different explosives by the damage they cause or the distance how far they are able to throw things. A promising test is the "Aquarium Test", which includes the explosive ignited under water and measuring the impact wave with lead or copper membranes

VIII. CONCLUSIONS

This research is dedicated to understanding the possible role that hydro-reaction of combustible metals might contribute to the terminal ballistics of shaped charges against underwater vessels. Investigations during this year have focused on understanding results of a series of tests conducted by Glumac and co-workers in which there were found substantial deformation in localized sections of water-submerged spaced target arrays resulting from the impact and penetration of aluminum jets [Mas10].

During the investigations, reported herein additional experimentation was performed jointly with Glumac, confirming previous results and a comprehensive set of computations performed for the purposes of identifying and quantifying jet energetics responsible for the observed results. The potential kinetic and chemical energy deposition of the jet during penetration are traced using the previously validate finite difference code and specialty post-processors. The results from these computations are then used to estimate the energy and fraction of deposited jet mass required to affect the observed target deformations. The effect of hydro-reaction is clearly shown from these analyses.

In addition to extending the experimental database, an attempt was made towards determining the dynamics of chemical energy release. That is, we wished to determine whether energy release occurs within the time period of penetration or is delayed. These failed attempts included high-speed photography at UIUC.

Predicted characterization of the 50mm aluminum-lined shaped charge designed and tested by UIUC from the AUTODYN computations include jet velocity and cumulative velocity. The tip velocity compares well with UIUC data; albeit that flash radiography would have led to a more accurate method of determination.

There is shown that average penetration resistance of the oil simulates matches that of inert water within 3-4 percent and the resistance of each agree with hydrodynamic penetration theory. Predicted time of arrivals through the spaced target submerged in the inert fluid simulant is also very close showing that the qualitative accuracy of the charges man-

ufactured. The small differences that are estimated are ascribed to slight imperfections in materials and eccentricities which are not taken and can not be into account in the computations in lieu of microscopic grain structure detail and (of each liner) and inspection data of all parts and the charge assembly, respectively⁷⁵. Differences between predicted and experimentally determined time-of-arrivals through the water submerged target arrays are found to be slightly larger and perhaps associated with hydro-reactive induced erosion, which slows penetration procession, however the differences are too small in this case for firm conclusion.

Approximately 15 percent of the liner mass jets, (ca. 4.4 grams) based on the computations. The accurate predictability of times-of-arrival provides good bases for estimating jet mass erosion and deposition between target plates. As with constant angle lined charge, jet mass increases along the jet length (and with jet velocity decrease). Eroded mass and mass deposition between plates are estimated by matching the velocities of jet impact from the TOA and the increments of mass predicted in the computations.

The kinetic and chemical energy required deform observed plate deformations are then estimated and the fraction of jet energy deposited between plates are then estimated based on aluminum-water thermochemistry and jet mass trapped between plates. Of the 4.4 grams of jet mass, 1 to 1.5 grams is becomes trapped between the last plate penetrated and the not penetrated plate in the path of the jet. It is estimated that 1-2.3 percent of the chemical potential of this aluminum segment is responsible for the observed deformation assuming that the jet segment reacts entirely between these two plated. Previous work, however, as shown that appreciable reaction can occur during transit through water. Analytical assessments of collected residues reveal much greater chemical transformation as well, but of course this debris might have reacted at times long after the penetration event. Thus the percentage of reaction responsible for the observed deformations is most likely much greater.

⁷⁵It should also be noted that the computations are not stochastic: All materials, dimensions, material response models, grid dimensions and zoning are fixed.

Along with the excellent agreement between predicted and experimentally determined jet times of arrival, there is also good agreement with respect to the disposition of the slug. It is obvious from the appearance of the plates along the early path of the jet that the slug does not reach beyond the fourth plate in the array (in one experiment the slug was trapped in the fourth plate), and therefore does not contribute to the major deformation observed along the deeper elements of the target array. Computational predictions confirm this conclusion.

It is concluded that hydro-reaction indeed contributes to the underwater performance of reactive jets and that a developed methodology can be employed to equate the exact nature of chemical contribution. The conclusion is supported by (i) accurate experimental comparisons against targets submerged in water and an inert water-simulant, and (ii) validated computational modeling⁷⁶. Supporting evidence of pre-impact hydro-reactive induced erosion from previous slower long-rod impact investigation could not be absolutely confirmed. This might have been limited by the physical size of the experimental devices. The validated methodology should be useful in assisting in the planning of future collaborative experimental investigations between NPS, UIUC and NSWC, and in predicting performance and meeting the challenge of incorporating reactive liner materials for enhanced terminal effects from warheads at realistic size.

⁷⁶NPS investigators have shown in other shaped charge studies and design efforts the accuracy of developed techniques using the ANSYS AUTODYN finite difference code.

THIS PAGE INTENTIONALLY LEFT BLANK

IX. RECOMMENDATIONS

Different issues are still uncertain in this research topic.

Although the experiments conducted so far show good compliance, more data is necessary, especially for the hole sizes and the TOA through the complete target. Additional test using oil should be considered to support the results derived from this data.

At the end of the research the deformation data of the additional experiments was available but could not be included due to the lack of time. Based on preliminary inspection the deformations are close to those examined from the prior tests. It should be evaluated and compared with the results herein, especially concerning the plastic deformation in the successful filter test.

Furthermore, tests should be conducted were the exact time when the deformation is occurring, which is still unknown, is determined. After the approach of using imaging systems was shown to be not feasible in recent experiments, maybe strain gauges could be used. Having this information and comparing it with the data from more oil tests would provide additional evidence for the combustion effect being responsible for the deformation.

While the energy dissipated in the plastic deformation of the target plates could be estimated quite exactly the amount needed for the displacement of the fluid and the general flow process stays unknown. Techniques should be developed which include the geometry of the actual setup leaving the non liquid parts rigid and concentrating on the flow process alone, thus providing the possibility to combine the results.

THIS PAGE INTENTIONALLY LEFT BLANK

A. DIMENSIONS OF THE TARGET

Figure 49 shows the described target and the dimensions.

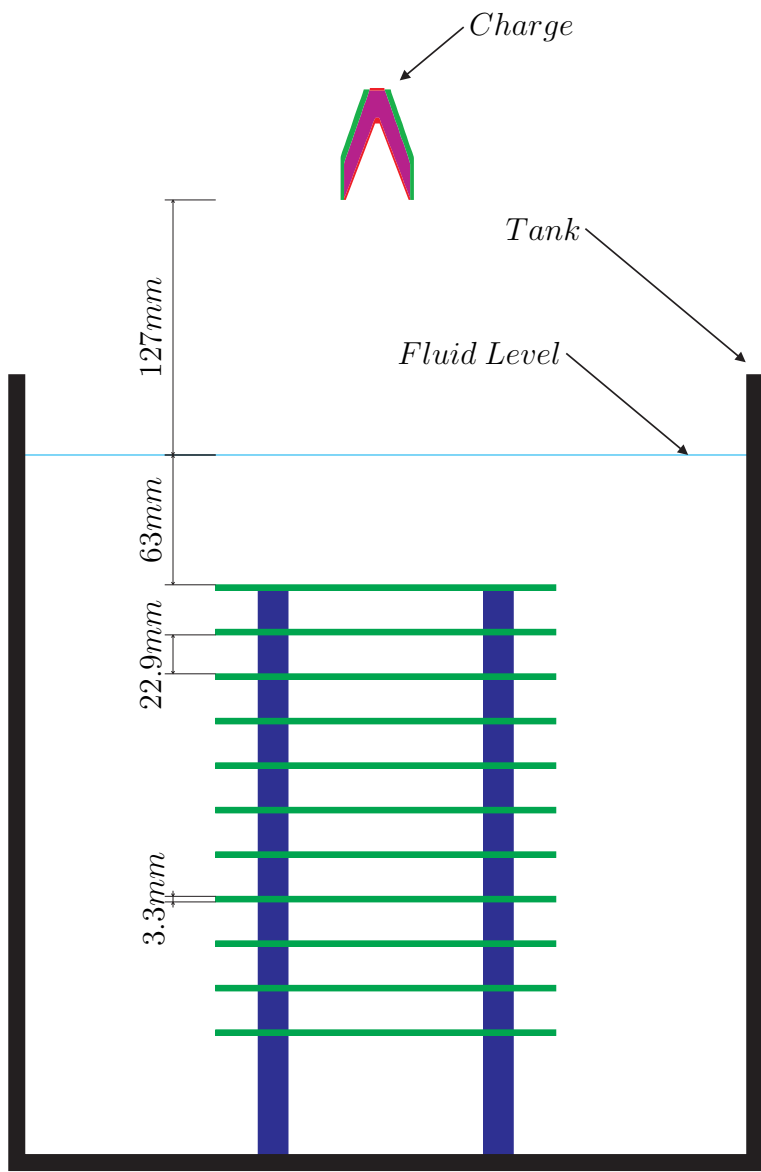


Figure 49: Sketch of the complete target setup showing the charge, the plate stack and the containing tank as well as the dimensions.

B. DRAWINGS AND DIMENSIONS OF THE CHARGE

Figure 50 shows the dimensions of the used liner. Figure 51 shows the dimensions of the used Confinement. Both figures are from [Mas10]. All dimensions in inch.

Figure 50: Engineering Drawing of the used UIUC charge liner [Mas10]

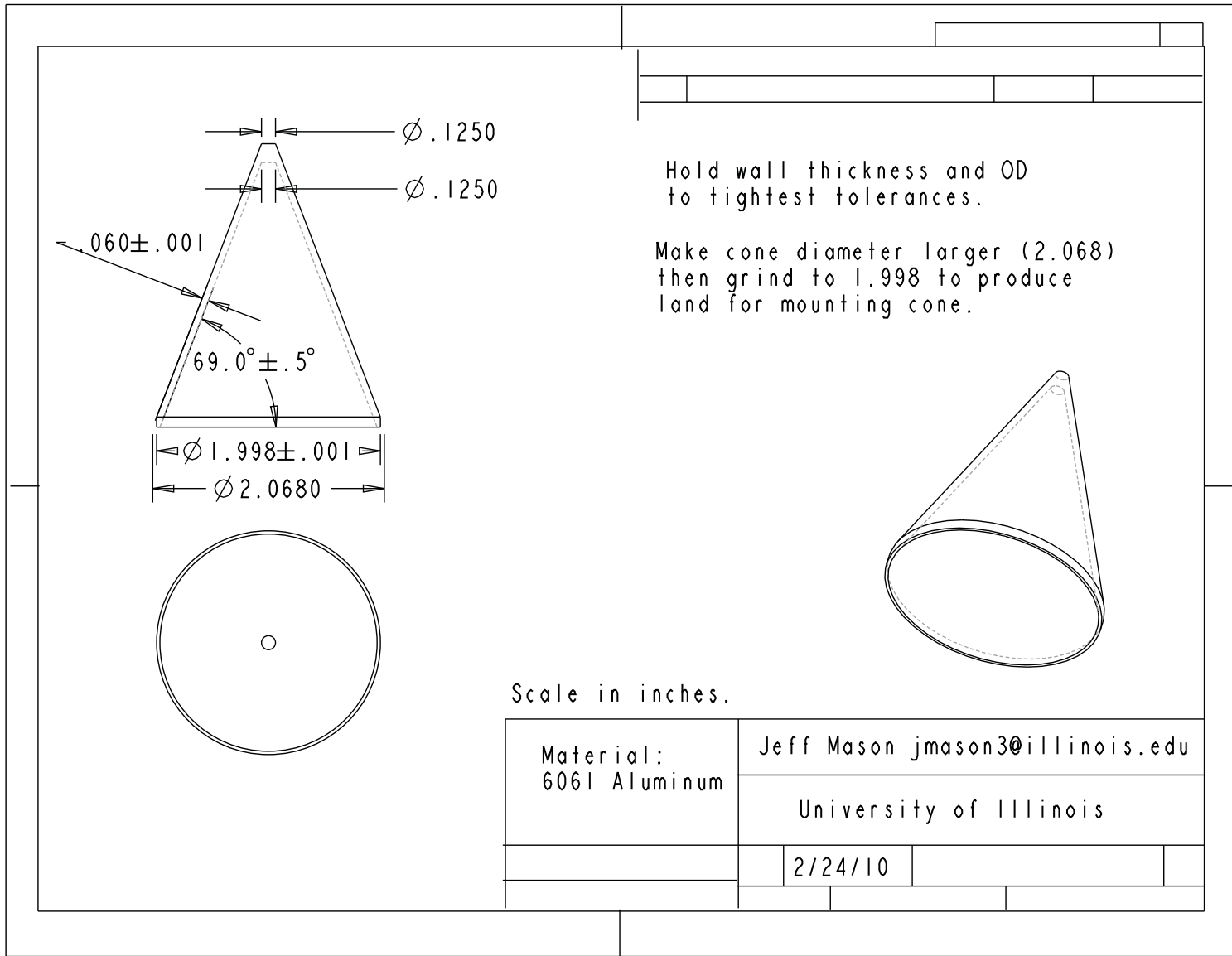
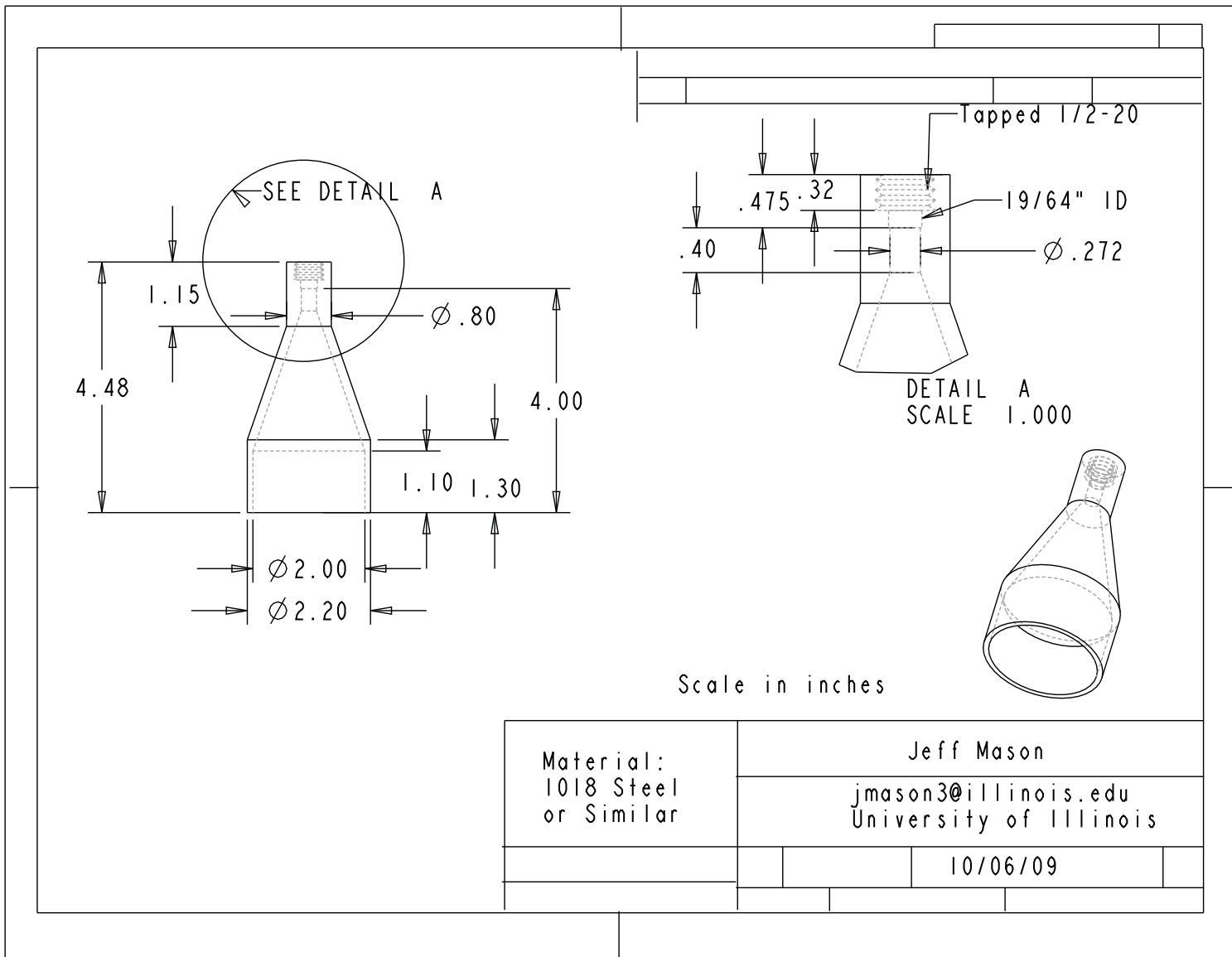


Figure 51: Engineering Drawing of the used UIUC charge confinement [Mas10]



THIS PAGE INTENTIONALLY LEFT BLANK

C. OVERVIEW OF THE EXPERIMENTS

The following table 5 displays a brief overview of the conducted preliminary and recent experiments.

The two test types, being a stack of plates or one thicker filter plate followed by a stack of plates are referred to as type "Plates" or "Filter Plate", respectively. The submerging fluid is also mentioned.

For the filter tests there were two gauges on the first plate, on the top and on the bottom. Both are counted separately.

	Test Name	Test Type	Plates Penetrated	TOA-Data	Remarks
Preliminary Tests	11	Plates Water	7	1-5	
	12	Plates Water	9	1-5	
	13	Plates Oil	9	1-10	It was unclear if the jet hit plate 10. Only oil test.
Recent Tests	1	Plates Water	8	1-9	The jet clearly hit plate 9, but did not penetrate it.
	2	Plates Water	7	1-8	The jet clearly hit plate 8, but did not penetrate it.
	3	Filter-Plate Water	0	1	The jet was not able to penetrate the filter plate. TOA is only available for the gauge on top of the filter plate
	4	Plates Water	9	4-10	Best jet performance in terms of penetration of all tests. The jet reached clearly plate ten, but was not able to penetrate it.
	5	Filter-Plate Water	1 + 4	4-6	The jet penetrated the filter plate and stopped after the following fourth plate.

Table 5: Overview of the Tests

D. COMPARISON OF THE DEFORMATION IN THE WATER AND OIL TESTS

The following figures show the comparison between the diagonal displacement in the z-direction of Test 12 (water) in red and Test 13 (oil) in blue for all plates up to number 12.

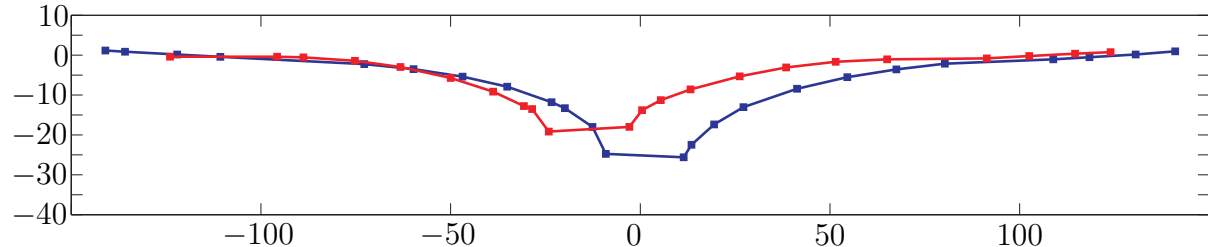


Figure 52: Plate 1 Deformation in Test 12 and Test 13

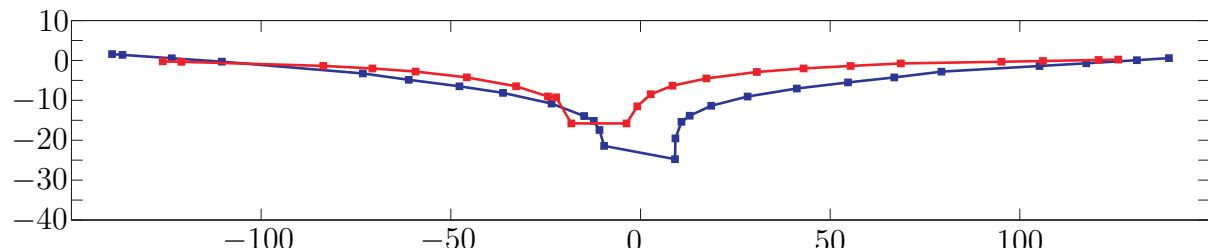


Figure 53: Plate 2 Deformation in Test 12 and Test 13

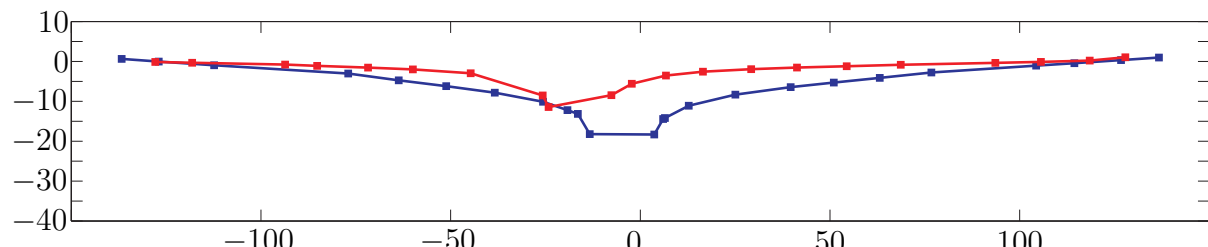


Figure 54: Plate 3 Deformation in Test 12 and Test 13

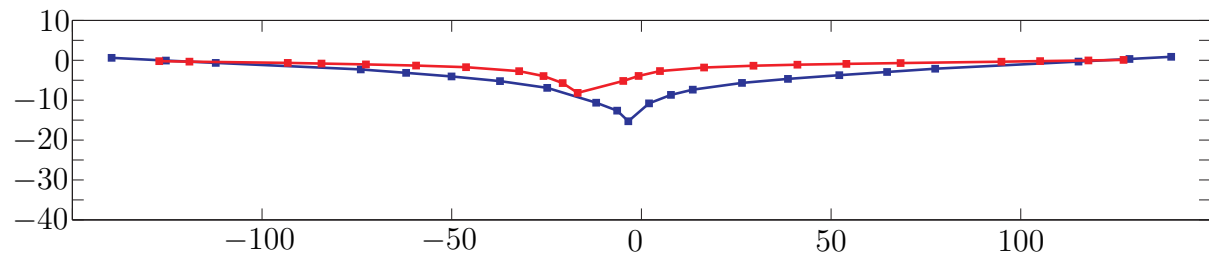


Figure 55: Plate 4 Deformation in Test 12 and Test 13

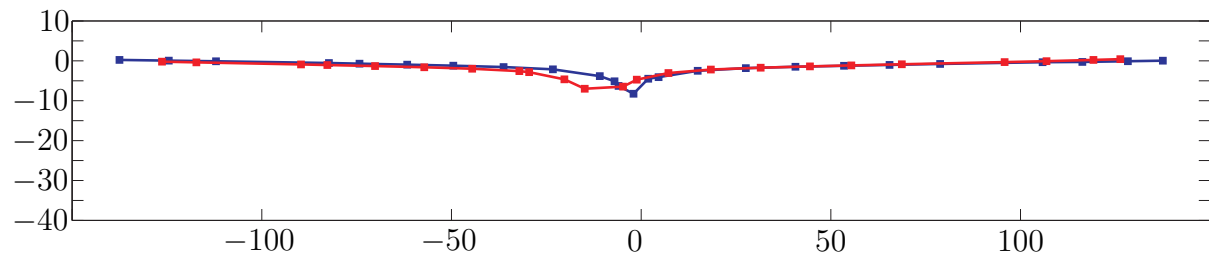


Figure 56: Plate 5 Deformation in Test 12 and Test 13

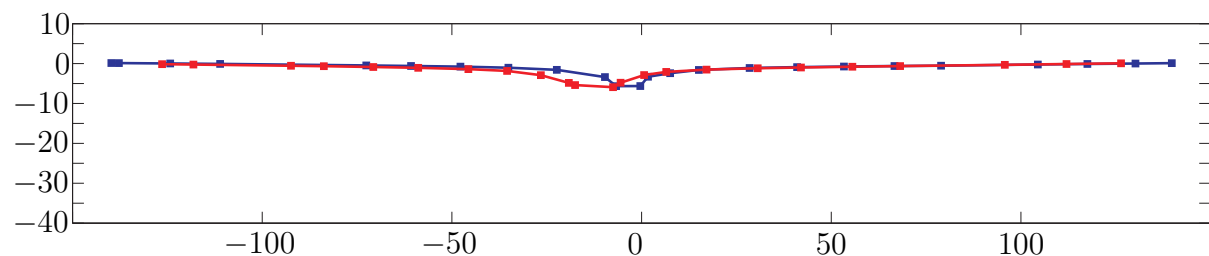


Figure 57: Plate 6 Deformation in Test 12 and Test 13

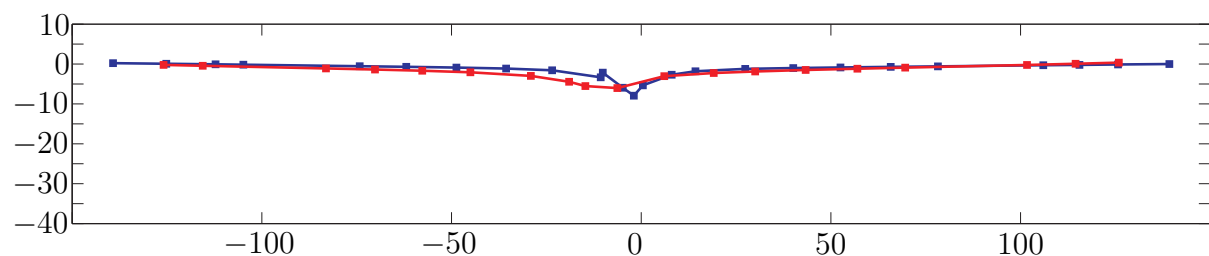


Figure 58: Plate 7 Deformation in Test 12 and Test 13

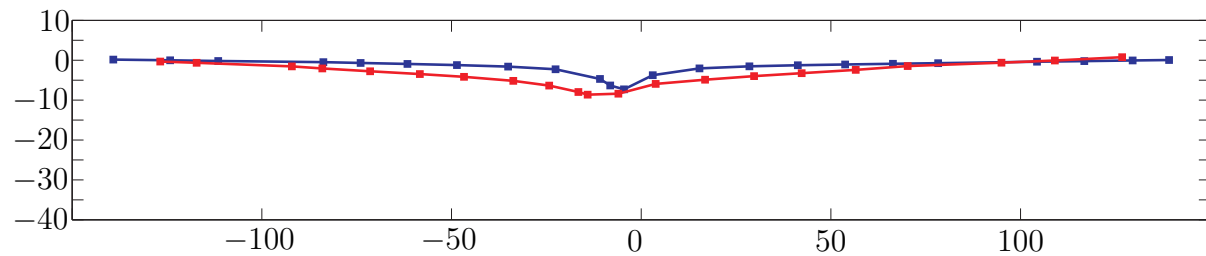


Figure 59: Plate 8 Deformation in Test 12 and Test 13

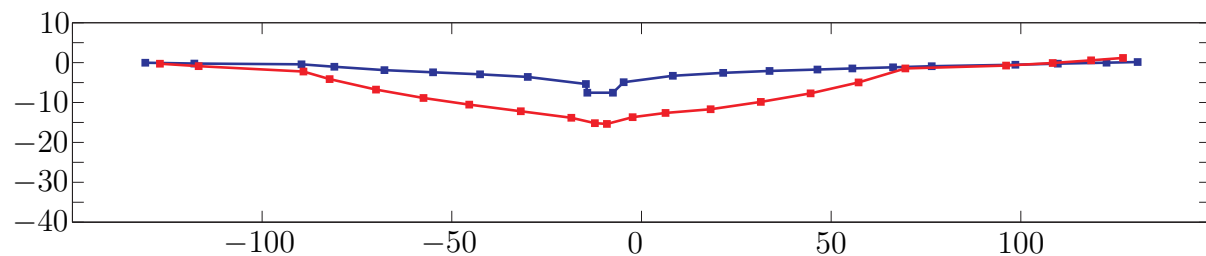


Figure 60: Plate 9 Deformation in Test 12 and Test 13

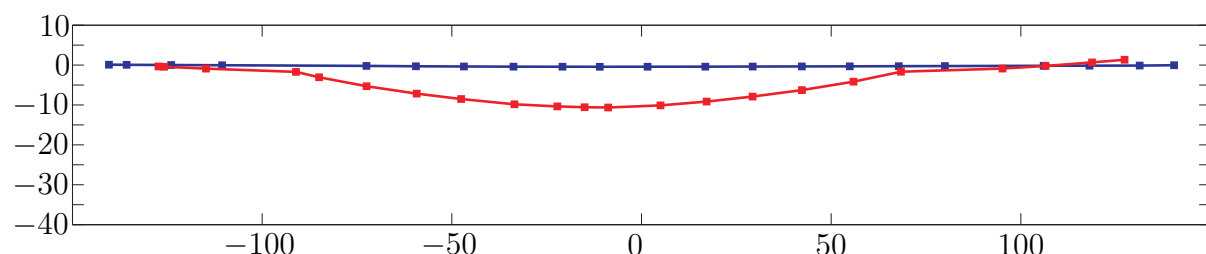


Figure 61: Plate 10 Deformation in Test 12 and Test 13

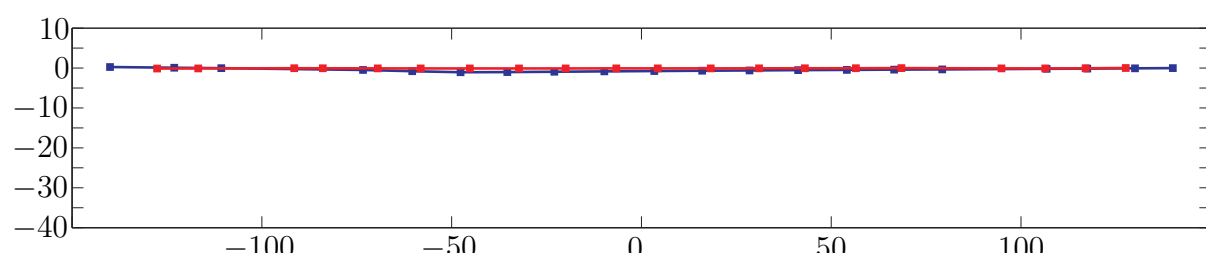


Figure 62: Plate 11 Deformation in Test 12 and Test 13

THIS PAGE INTENTIONALLY LEFT BLANK

E. RESULTS OF THE ADDITIONAL EXPERIMENTS

Tables 6 to 9 are displaying the TOA and the hole diameter data gathered for the experiments at the UIUC.

In the tables *n.D.* stands for *no Data*.

Test1,2 and 4 are repetitions of Masons Tests. Test 3 and 5 are the mentioned filter tests.

In Test 4 and 5 the first three TOA gages could not be measured.

Plate Number	TOA in <i>s</i>	Hole Diameter in <i>mm</i>
1	60.800	16.490
2	70.500	15.060
3	81.600	13.670
4	94.800	8.590
5	109.000	6.850
6	126.000	7.480
7	149.000	7.430
8	164.000	6.080

Table 6: Test results for Test 1

Plate Number	TOA in <i>s</i>	Hole Diameter in <i>mm</i>
1	61.500	20.890
2	71.300	15.140
3	82.500	10.830
4	96.400	7.440
5	111.000	7.550
6	131.000	7.470
7	152.000	7.750
8	182.000	n.D.

Table 7: Test results for Test 2

Plate Number	TOA in <i>s</i>	Hole Diameter in <i>mm</i>
1	n.D.	16.120
2	n.D.	14.350
3	n.D.	10.360
4	94.300	7.430
5	112.100	7.310
6	129.100	7.190
7	149.500	6.690
8	176.700	5.690
9	205.300	5.350
10	247.300	n.D.

Table 8: Test results for Test 4

Plate Number	TOA in <i>s</i>	Hole Diameter in <i>mm</i>
1	n.D.	12.540
1	n.D.	10.020
2	n.D.	9.810
3	129.000	8.700
4	155.000	6.740
5	192.000	n.D.

Table 9: Test results for Test 5

F. COMPLETE TOA AND HOLE DIAMETER DATA

Table 10 shows the TOA data for all tests involving the plate array. All times are in *s*. In the table *n.D.* stands for *no Data*.

Table 11 shows the hole diameter data likewise. All diameters are in *mm*.

Plate Number	Test11	Test12	Test13	Test1	Test2	Test4
1	65.300	63.500	60.900	60.800	61.500	<i>n.D.</i>
2	74.500	72.500	71.100	70.500	71.300	<i>n.D.</i>
3	87.900	84.300	84.300	81.600	82.500	<i>n.D.</i>
4	101.000	97.900	97.300	94.800	96.400	94.300
5	119.000	112.000	110.000	109.000	111.000	112.100
6	<i>n.D.</i>	<i>n.D.</i>	127.000	126.000	131.000	129.100
7	<i>n.D.</i>	<i>n.D.</i>	143.000	149.000	152.000	149.500
8	<i>n.D.</i>	<i>n.D.</i>	166.000	164.000	182.000	176.700
9	<i>n.D.</i>	<i>n.D.</i>	189.000	<i>n.D.</i>	<i>n.D.</i>	205.300
10	<i>n.D.</i>	<i>n.D.</i>	<i>n.D.</i>	<i>n.D.</i>	<i>n.D.</i>	247.300

Table 10: Complete TOA Data

Plate Number	Test11	Test12	Test13	Test1	Test2	Test4
1	16.000	18.000	23.000	16.490	20.890	16.120
2	13.000	14.000	18.000	15.060	15.140	14.350
3	15.000	13.000	14.000	13.670	10.830	10.360
4	13.000	8.000	8.000	8.590	7.440	7.430
5	8.000	7.000	6.000	6.850	7.550	7.310
6	7.000	7.000	7.000	7.480	7.470	7.190
7	6.000	6.000	7.000	7.430	7.750	6.690
8	4.000	5.000	6.000	6.080	<i>n.D.</i>	5.690
9	<i>n.D.</i>	4.000	6.000	<i>n.D.</i>	<i>n.D.</i>	5.350

Table 11: Complete Hole Diameter Data

THIS PAGE INTENTIONALLY LEFT BLANK

G. MATERIAL PROPERTIES FOR THE AUTODYN SIMULATIONS

Coefficient	NM
Equation of State	JWL
Reference density	1.12800E+00 $\frac{g}{cm^3}$
Parameter A	2.0925E+08 kPa
Parameter B	5.6890E+06 kPa
Parameter R1	4.4000E+00
Parameter R2	1.2000E+00
Parameter W	3.0000E-01
C-J Detonation velocity	6.2800E+03 $\frac{m}{s}$
C-J Energy / unit volume	5.1000E+06 $\frac{kJ}{m^3}$
C-J Pressure	1.2500E+07 kPa
Burn on compression fraction	0.0000E+00
Pre-burn bulk modulus	0.0000E+00 kPa
Adiabatic constant	0.00000E+00 kPa
Auto-convert to Ideal Gas	Yes
Additional Options (Beta)	None
Strength	None
Failure	None
Erosion	None
Material Cutoffs	
Maximum Expansion	1.00000E-01
Minimum Density Factor	1.00000E-06
Minimum Soundspeed	1.00000E-06 $\frac{m}{s}$
Maximum Temperature	1.01000E+20 K

Table 12: Material Properties for Nitromethane

Coefficient	AL2024T351	Steel 1006	Oil/Water
Reference density	2.785E+00 $\frac{g}{cm^3}$	7.896E+00 $\frac{g}{cm^3}$	9.200E-01/1.000E-1 $\frac{g}{cm^3}$
Grueneisen coefficient	2.000E+00	2.170E+00	0.000E+00
Parameter C1	5.328E+03 $\frac{m}{s}$	4.569E+03 $\frac{m}{s}$	1.647E+03 $\frac{m}{s}$
Parameter S1	1.338E+00 $\frac{m}{s}$	1.490E+00 $\frac{m}{s}$	1.921E+00 $\frac{m}{s}$
Parameter Quadratic S2	0.00000E+00 $\frac{s}{m}$	0.00000E+00 $\frac{s}{m}$	0.00000E+00 $\frac{s}{m}$
Relative volume, VE/V0	0.000E+00	0.000E+00	0.000E+00
Relative volume, VB/V0	0.000E+00	0.000E+00	0.000E+00
Parameter C2	0.000E+00 $\frac{m}{s}$	0.000E+00 $\frac{m}{s}$	0.000E+00 $\frac{m}{s}$
Parameter S2	0.000E+00	0.000E+00	0.000E+00
Reference Temperature	3.000E+02 K	3.000E+02 K	3.000E+02 K
Specific Heat	8.750E+02 $\frac{J}{kgK}$	4.520E+02 $\frac{J}{kgK}$	0.000E+02 $\frac{J}{kgK}$
Thermal Conductivity	0.000E+00 $\frac{J}{mKs}$	0.000E+00 $\frac{J}{mKs}$	0.000E+00 $\frac{J}{mKs}$
Strength	Johnson Cook	Johnson Cook	None
Shear Modulus	2.760E+07 kPa	8.180E+07 kPa	None
Yield Stress	2.650E+05 kPa	3.500E+05 kPa	None
Hardening Constant	4.260E+05 kPa	2.750E+05 kPa	None
Hardening Exponent	3.400E-01	3.600E-01	None
Strain Rate Constant	1.500E-02	2.200E-02	None
Thermal Softening Exponent	1.000E+00	1.000E+00	None
Melting Temperature	7.750E+02 K	1.822E+03 K	None
Ref. Strain Rate $\frac{1}{s}$	1.000E+00	1.000E+00	None
Strain Rate Correction	1st Order	1st Order	None
Failure	None	None	None
Erosion	None	None	None
Material Cutoffs			
Maximum Expansion	1.000E-01	1.000E-01	1.000E-01
Minimum Density Factor	1.000E-04	1.000E-04	1.000E-04
Minimum Soundspeed	1.000E-06 $\frac{s}{m}$	1.000E-06 $\frac{s}{m}$	1.000E-06 $\frac{s}{m}$
Maximum Temperature	1.010E+20 K	1.010E+20 K	1.010E+20 K

Table 13: Material Properties for the AUTODYN penetration simulations

H. RESULTS OF THE MASS DISTRIBUTION ESTIMATIONS

The following tables are providing the mass distribution data from the various approaches. The mass values represent the amount of aluminum which is eroded from the jet before each plate.

Only the plates were TOA data was available is included, which explains the differences.

The huge amount of mass which is distributed before plate one is due to the heavier tip, which is eroded int the relatively thick water portion before the first plate.

Plate Number	Distributed Mass in g	Possible Chemical Energy Release in kJ
1	3.016	46.451
2	0.068	1.044
3	0.102	1.571
4	0.133	2.047
5	0.132	2.027
6	0.143	2.200
7	0.202	3.104
8	0.238	3.673
9	0.261	4.017
10	0.374	5.762
11	0.457	7.035
12	0.468	7.202
13	0.531	8.178
14	0.398	6.135
15	0.561	8.640

Table 14: Mass distribution data from the water simulation

Plate Number	Distributed Mass in <i>g</i>	Possible Chemical Energy Release in <i>kJ</i>
1	3.074	47.338
2	0.092	1.414
3	0.102	1.573
4	0.111	1.710
5	0.102	1.578
6	0.244	3.757
7	0.114	1.760
8	0.297	4.567
9	0.362	5.582
10	0.412	6.341
11	0.512	7.880
12	0.392	6.032
13	0.535	8.238
14	0.357	5.500
15	0.834	12.837

Table 15: Mass distribution data from the oil simulation

Plate Number	Distributed Mass in <i>g</i>	Possible Chemical Energy Release in <i>kJ</i>
1	2.448	37.703
2	0.327	5.031
3	0.513	7.906
4	0.686	10.557
5	1.585	24.407

Table 16: Mass distribution in Test 11

Plate Number	Distributed Mass in <i>g</i>	Possible Chemical Energy Release in <i>kJ</i>
1	2.368	36.468
2	0.281	4.332
3	0.392	6.030
4	0.553	8.509
5	0.823	12.681

Table 17: Mass distribution in Test 12

Plate Number	Distributed Mass in g	Possible Chemical Energy Release in kJ
1	2.816	43.364
2	0.176	2.707
3	0.225	3.467
4	0.254	3.918
5	0.279	4.299
6	0.491	7.566
7	0.615	9.474
8	0.957	14.738
9	0.953	14.680

Table 18: Mass distribution in Test 13

Plate Number	Distributed Mass in g	Possible Chemical Energy Release in kJ
1	2.718	41.852
2	0.180	2.768
3	0.227	3.503
4	0.316	4.859
5	0.384	5.920
6	0.633	9.748
7	1.203	18.533
8	0.800	12.318

Table 19: Mass distribution in Test 1

Plate Number	Distributed Mass in g	Possible Chemical Energy Release in kJ
1	2.734	42.104
2	0.217	3.335
3	0.256	3.943
4	0.362	5.575
5	0.497	7.661
6	1.032	15.899
7	1.250	19.256
8	1.582	24.360

Table 20: Mass distribution in Test 2

Plate Number	Distributed Mass in g	Possible Chemical Energy Release in kJ
4	4.242	65.321
5	0.403	6.211
6	0.480	7.397
7	0.536	8.254
8	0.800	12.318
9	0.791	12.175
10	1.423	21.918

Table 21: Mass distribution in Test 4

I. RESULTS OF THE ANSYS WORKBENCH PENETRATION SIMULATIONS

Figure 63 to 44 display the diagonal deformation of the target plates due to penetration. The blue graph shows the simulation results while the red graph shows the data of Test 13. Table 22 shows the jet values used for the simulation.

Plate Number	<i>length in mm</i>	<i>r in mm</i>	<i>adapted r in mm</i>	<i>v in $\frac{m}{s}$</i>
1	4.004	2.25	1.026	4580.704
2	4.804	2.25	1.124	4346.874
3	5.005	2.50	1.275	4050.856
4	6.407	2.75	1.587	3732.450
5	6.206	3.00	1.704	3331.954
6	7.608	3.50	2.201	2933.947
7	4.004	4.50	2.053	2411.561
8	6.206	6.00	3.407	1814.550
9	6.532	4.50	2.623	1043.410

Table 22: Values for the penetration simulations

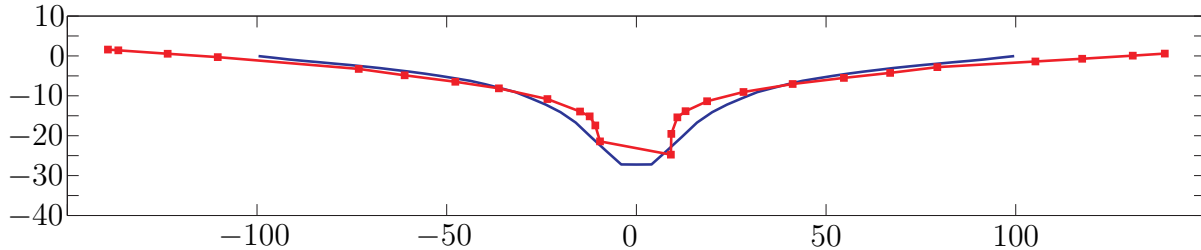
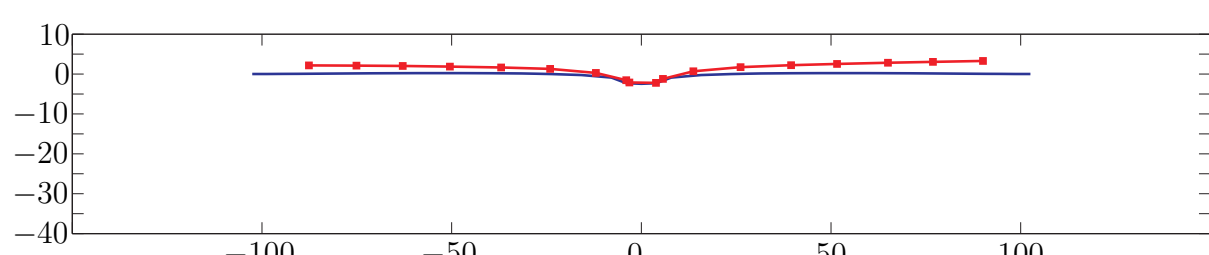
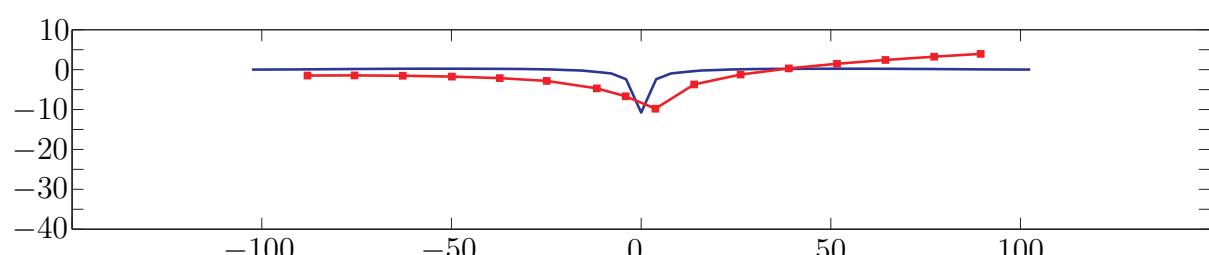
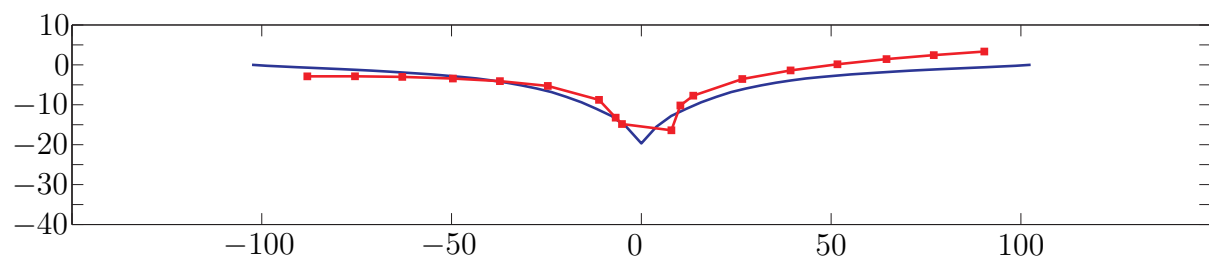
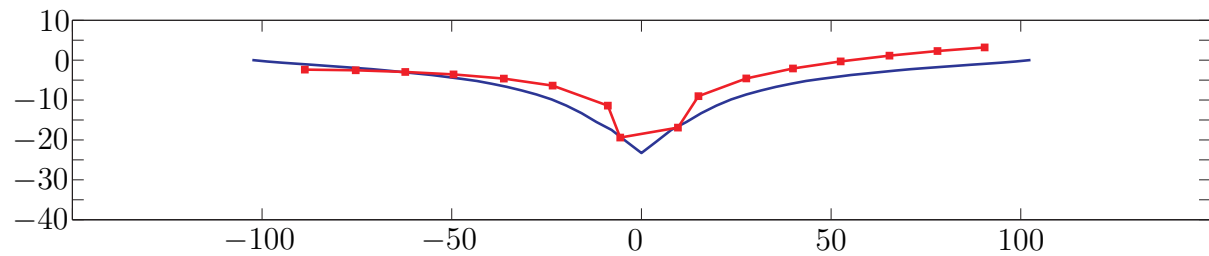


Figure 63: Plate 1 Penetration Simulation



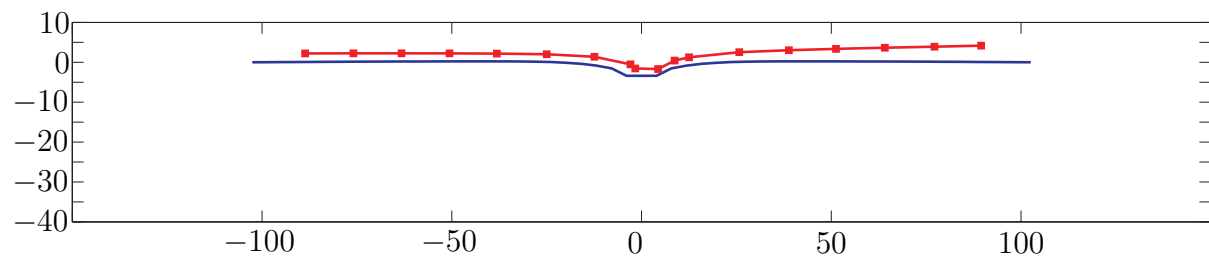


Figure 68: Plate 6 Penetration Simulation

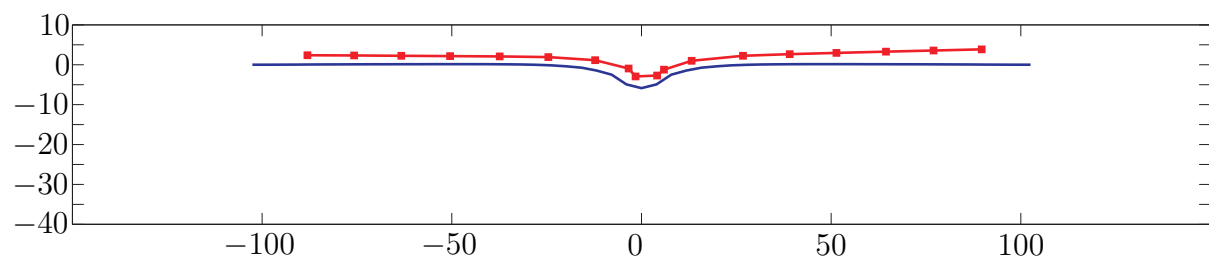


Figure 69: Plate 7 Penetration Simulation

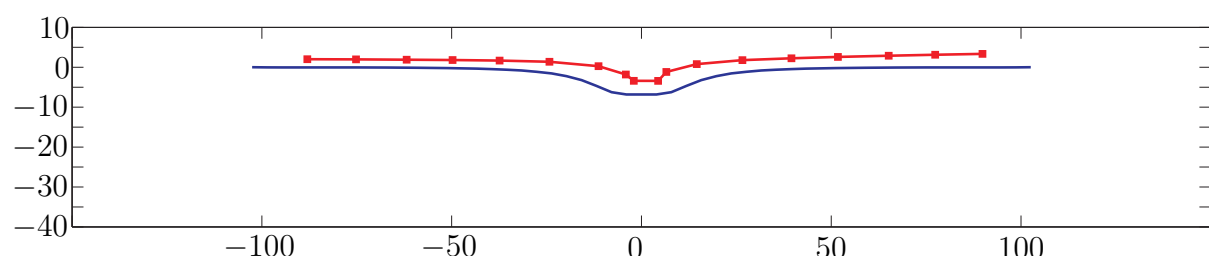


Figure 70: Plate 8 Penetration Simulation

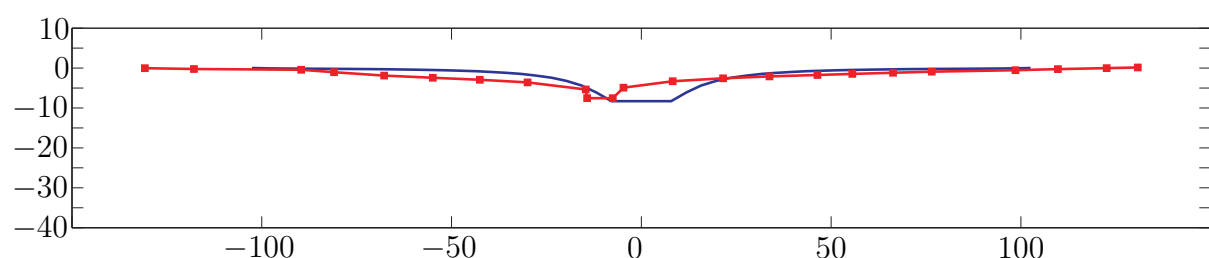


Figure 71: Plate 9 Penetration Simulation

THIS PAGE INTENTIONALLY LEFT BLANK

J. DESCRIPTION OF CREATING GEOMETRY FOR AUTODYN WITH MATLAB

As mentioned before, the possibilities of creating geometries in Autodyn are very restricted. Especially the impossibility of saving certain geometry to reuse the setting in different simulations is time-consuming.

There is a way to built the geometry using the design modeler tool which is part of the WORKBENCH package and coupling this with an AUTODYN simulation. This is a beta option and relatively complicated. It was observed that it leads to very high energy errors in shaped charge simulations in release 12.1, and a lot of system crashes in release 13.0.

Hasenberg mentioned a method in [Has10] importing geometry from files created with MATLAB. A technique like that was used for the charge creation in this research. It is very simple and showed good results.

Autodyn can import geometry from TRUEGRID⁷⁷, which produces .zon files. The relative simplicity of these files allows generating geometry with easy mathematical methods. These files have a build-up which is described in figure 72.

Header	IMPLICIT
Part name	LINER
Number of nodes (i and j)	1 2 1 2
x- and y- coordinates of the node 1,1	1.0 1.0
node 1,2	1.0 2.0
node 2,1	2.0 1.0
node 2,2	2.0 2.0
End of file	END

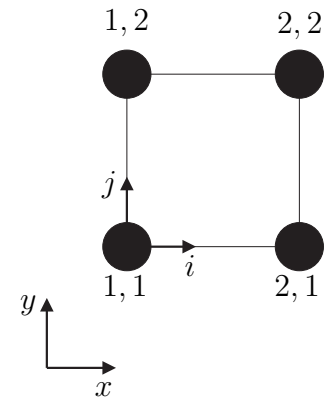


Figure 72: Build-up of a .zon file (left) and the matching simple example consisting of one cell (right)

⁷⁷TRUEGRID is a mesh generator and preprocessing software.

The main information included in the header is the part name and the number of nodes in every dimension. For shaped-charge simulations usually 2D-setups are chosen. Therefore only i and j are needed to describe the part. It is possible to describe 3D parts by adding a k index and a third row.

Creating geometries for Autodyn with that sort of file is easy, as long one (i) stays with 2D problems and (ii) chooses forms which can be described by continuous functions. It is not necessary that all defining edges are describable in one continuous function, but the edges should be able to be divided in such parts. If not, every node must be programmed by hand.

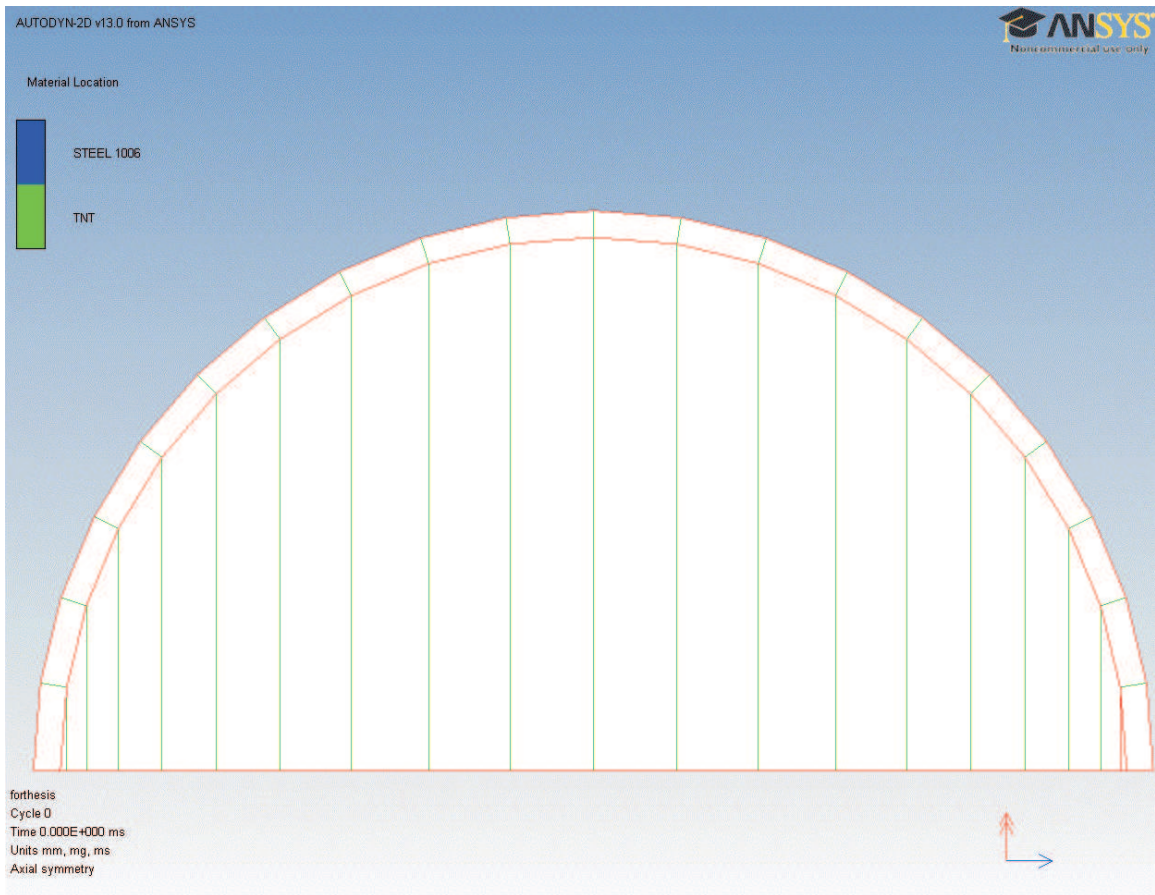


Figure 73: Grid of the sphere and the explosive after importing into AUTODYN

Normally shaped charges meet all this preconditions perfectly. The fact that the part will be later filled into the main blast area-part in AUTODYN allows to mesh the part by just two nodes in the j direction and describing the whole part with a closed curve around it, similar like the sphere shown in figure 73. The whole part is described by a simple line of cells, with only one cell in the j -dimension.

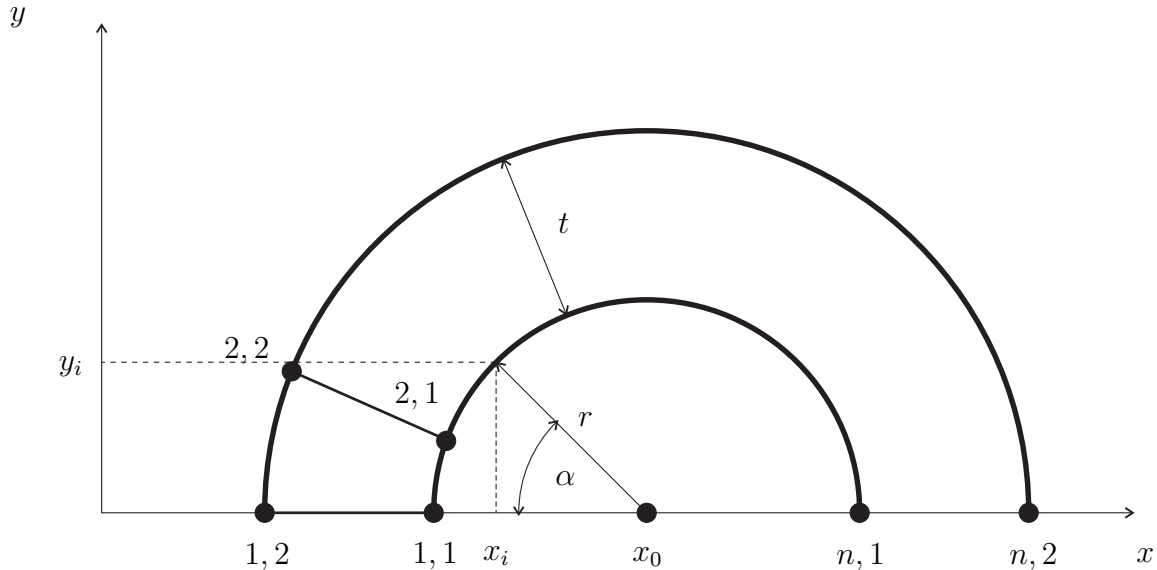


Figure 74: Set-Up and values of the MATLAB function to create the hollow sphere

The following MATLAB-Code produces two parts (a hollow sphere and a explosive core) and exports them into two .zon files, which can be easily imported into AUTODYN. After importing they need to be filled with material and can be filled into any other part. The parameters that are used can be seen in figure 74, which shows these parameters for the hollow sphere.

```

2 function GeometryCreator

4 % Main-script for programming geometries for Autodyn in an .zon format
5 % (truegrid).
6 % The function creates a 2D-Geometry, consisting of a hollow sphere filled
7 % with an explosive part.

9 close all;
10 clear all;

12 r = 100; % inner radius of the sphere
13 t = 5; % Thickness of the sphere

15 x0 = 20; %x-value of the center of the sphere.
16 n = 20; % Number of nodes in the i-direction

19 % Due to the structure of .zon files the hollow sphere will consist of two
20 % bows, on which the nodes will be placed. Due to the 2D character only
21 % half of the sphere is created.
22 % Each bow contains n+1 rows and 2 collumns, for the x and y values of every
23 % node.

25 innerbow = zeros(n+1,2);
26 outerbow = zeros(n+1,2);

28 alpha = 0:pi/n:pi;
29 for i = 1:n+1
30     innerbow(i,1) = x0-r*cos(alpha(i));
31     innerbow(i,2) = r*sin(alpha(i));

33     outerbow(i,1) = x0-(r+t)*cos(alpha(i));

```

```

34     outerbow(i,2) = (r+t)*sin(alpha(i));
35 end

37 % The explosive part shares half of its nodes with the inner bow, and the
38 % other half is situated on the x-axis. They have the same x-values as the
39 % ones in the bow.
40 % The first and last nodes of both lines have the same values.

42 OuterExplosive = innerbow;

44 InnerExplosive = innerbow;

46 InnerExplosive(:,2) = 0;

48 % Now the parts can be written into two .zon files, which can be imported
49 % into AUTODYN.

51 fid = fopen('Sphere.zon','wt');
52 fprintf(fid,'IMPLICIT\n');
53 fprintf(fid,'SPHERE\n');
54 fprintf(fid,'%d %d %d %d\n',1,n+1,1,2);

56 for i=1:n+1
57     fprintf(fid,'%1.5f %1.5f\n',innerbow(i,1),innerbow(i,2))
58     fprintf(fid,'%1.5f %1.5f\n',outerbow(i,1),outerbow(i,2))
59 end
60 fprintf(fid,'END');
61 fclose(fid);

```

THIS PAGE INTENTIONALLY LEFT BLANK

LIST OF REFERENCES

[And99] D.L. Orphal C.E. Anderson. Streamline reversal in hypervelocity penetration. *International Journal of Impact Engineering*, (23):699–710, 1999.

[Bec07] M.W. Beckstead. A summary of aluminum combustion. *NATO Research and Technology Organization (RTO), Neuilly sur Seine*, 2007.

[Car95] C. Carrington. *Basic Thermodynamics*. Oxford University Press, Oxford, 1995.

[C.C96] M. Held N.S. Huang D.Jiang C.C.Chang. Determination of the crater radius as a function of time of a shaped charge jet that penetrates water. *Propellants, Explosives, Pyrotechnics*, (21):64–69, 1996.

[Coo96] P. Cooper. *Explosives Engineering*. Willey-VCH, New York, 1996.

[Dol08] M. Dolak. Exploration of potential chemical energy/kinetic energy coupling during hypervelocity impact and penetration. Master’s thesis, Naval Postgraduate School, Monterey, 2008.

[Duo05] D.V. Duong. Overcoming the effects of supra-pressure detonation on shaped charge performance by liner material substitution (excerpts). Master’s thesis, Naval Postgraduate School, Monterey, 2005.

[Eld99] C.E. Anderson J.S. Wilbeck J.S. Elder. Long rod penetration into highly oblique, water-filled targets. *International Journal of Impact Engineering*, (23):1–12, 1999.

[Fan08] B. Fant. Experimental investigation of enhanced aluminum steam explosions for improving reactive underwater shaped charges. Master’s thesis, Graduate College of the University of Illinois, Urbana-Champaign, 2008.

[Fli86] P.C. Chou W.J. Flis. Recent developments in shaped charge technology. *Propellants, Explosives, Pyrotechnics*, (11):99–114, 1986.

[Gok96] M. Marion C. Chauveau I. Gokalb. Studies on the ignition and burning of aluminum particles. *Combustion Science and Technology*, (116):369–390, 1996.

[Has10] D. Hasenberg. Consequences of coaxial jet penetration performance and shaped charge design criteria. Master’s thesis, Naval Postgraduate School, Monterey, 2010.

[Haz06] P.J. Hazell. *Ceramic Armour: Design and Defeat Mechanisms*. Argos Press, Canberra, 1. edition, 2006.

[Hom02] R. Meyer J. Koehler A. Homburg. *Explosives*. Willey-VCH, Weinheim, 2002.

[Koh85] Y. Chozev J. Kohl. Burning time and size of aluminum, magnesium, zirconium, tantalum, and pyrofuzes particles burning in steam. Technical report, Naval Post-graduate School, Monterey, 1985.

[Lab80] Los Alamos National Laboratories. Lasl shock hugoniot data. *Los Alamos Series on Dynamic Material Properties*, 1980.

[Mas10] J. Mason. Experimental testing of bimetallic and reactive shaped charge liners. Master’s thesis, Graduate College of the University of Illinois, Urbana-Champaign, 2010.

[May07] E. Hirsch M. Mayseless. The maximum mach number of coherent copper jet. *23rd International Symposium on Ballistics, Tarragona*, 2007.

[O’C01] B. Poling J. Prausnitz J. O’Connel. *The Properties of Gases and Liquids*. McGraw-Hill Professional, New York, 2001.

[Pal02] E. Paland, editor. *Technisches Taschenbuch*. Schaeffler KG, Herzogenaurach, 7. edition, 2002.

[Pet11] M. Peters. *Characteristics and Requirements of Combustion During Hyper Velocity Impact in Water Submerged Targets*. Studienarbeit, Helmut-Schmidt-Universitt, Universitt der Bundeswehr Hamburg and Naval Postgraduate School, Monterey, 2011.

[SAS10] SAS IP, Inc., Canonsburg. *Training Manual: Introduction to ANSYS Explicit Dynamics*, 1st edition, February 2010.

[Sch10] U. Schleicher. *Scriptum: Munitionstechnik*. Helmut-Schmidt-Universitt, Universitt der Bundeswehr Hamburg, 2010.

[Sha86] Z. Shavit. A transient one-dimensional model for metal combustion in steam. Technical report, Naval Postgraduate School, Monterey, 1986.

[Ste96] D.J. Steinberg. *Equation of State and Strength Properties of Selected Materials*. Lawrence Livermore National Laboratory, Livermore, 1996.

[Tri76] W.G. Von Holle J.J. Trimble. Shaped charge temperature measurement. *Proceedings of the Sixth Symposium (International) on Detonation*, pages 691–699, 1976.

[Wil03] T. Wille. *Aufarbeitung der Grundlagen von Zndern und Anzndsystemen sowie Projektil- und Hohlladungen*. Diplomarbeit, Helmut-Schmidt-Universitt, Universitt der Bundeswehr Hamburg, 2003.

[Zuk97] W.P. Walters J.A. Zukas. *Explosive Effects and Applications*. Springer-Verlag, New York, 1997.

[Zuk98] W.P. Walters J.A. Zukas. *Fundamentals of Shaped Charges*. CMCPress, Baltimore, 1. edition, 1998.